Ultrafast mid-infrared pulse generation and characterization in chalcogenide microwires

Nurmemet Abdukerim

Department of Electrical & Computer Engineering
McGill University
Montreal, Canada

November 2018

A thesis submitted to McGill University in partial fulfillment of the requirements for the degree of Doctor of Philosophy.

2018/11/21

Abstract

Mid-infrared (IR) wavelength range (2–12 μm), encompassing numerous molecular fingerprints with strong fundamental vibrational transitions, is tremendously important for various spectroscopy applications, including military/chemical sensing, medical diagnosis and environmental monitoring. Currently, commercially available mid-IR sources are mostly based on semiconductor or gas gain media, nonlinear wavelength conversion in bulk nonlinear crystals, and rare-earth doped fluoride fibers. Generally, fiber lasers have the advantages of high efficiency, compactness, superior reliability, and excellent beam quality. Commercially available mid-IR fiber lasers are mostly based on silica or fluoride fibers. However, transmission windows of silica and fluoride glasses are limited to 2.5 μm and 5.5 μm, respectively, and emission from rare-earth dopants can only cover a small portion of the mid-IR spectral region. In comparison, chalcogenide glasses have much wider transmission windows (up to 15 μm), and high intrinsic nonlinearity enables emission virtually at any wavelength based on nonlinear gain. In this thesis, I have investigated nonlinear fiber oscillators based on chalcogenide microwires in the wavelength band of 2 μm, which is useful for the identification of atmospheric gasses such as CO_2, NH_3, C_2H_2, water vapor, and other chemical species. Unfortunately, commercially available pulse characterization techniques, such as intensity autocorrelator and frequency-resolved optical gating (FROG), are not sensitive enough to characterize the output pulses. Thereafter, I have developed highly sensitive FROG pulse characterization techniques based on extremely high nonlinearity in chalcogenide microwires.

This thesis is composed of two main parts. In the first part, two approaches to mid-IR pulse generation are demonstrated. First approach is a 2 μm Raman fiber laser using a multimaterial chalcogenide microwire. The microwire is composed of As_2Se_3 core, As_2S_3 cladding, and poly-methyl methacrylate (PMMA) coating, providing mid-infrared compatibility up to 10 μm with high nonlinearity and excellent mechanical robustness. Raman gain profile of the microwire is experimentally characterized, and Raman laser oscillation in a ring cavity is achieved at a low threshold peak power, with 8 nm of wavelength tunability range. Numerical simulations are performed by solving the generalized nonlinear Schrödinger equation using the split-step Fourier method, and good agreement is found between numerical and experimental results. The second approach is a 2 μm fiber optical parametric oscillator using a chalcogenide microwire cladded with Cyclo Olefin polymer (COP). The microwire is highly nonlinear and optimized for parametric gain in the anomalous dispersion regime. Parametric gain profile of the microwire is experimentally characterized, and parametric oscillation in a ring cavity is achieved at a low threshold peak power, with 55 nm of signal wavelength

tunability range, and total emission wavelength covering 290 nm in total with the help of cascaded parametric generation. Output wavelength of these optical sources can be further extended into the mid-IR with optimization of the cavity configuration and microwire structure.

In the second part of this thesis, two approaches to mid-IR FROG pulse characterization are demonstrated in the 2 μm wavelength band. First approach is a modified FROG pulse characterization technique based on highly efficient four-wave mixing in a COP-cladded chalcogenide microwire fabricated with anomalous chromatic dispersion. The FROG traces are identical to the ones obtained from conventional FROGs based on second-harmonic generation. The amplitude and phase of chirped and unchirped picosecond pulses are accurately characterized with a high sensitivity of 0.16 mW^2, which is several orders of magnitude better than the sensitivity of conventional FROGs. Second approach is another modified FROG pulse characterization technique, but this time based on cross-phase modulation in a COP-cladded chalcogenide microwire fabricated with zero chromatic dispersion. Without the direction-of-time ambiguity and the need for a continuous wave probe laser, the amplitude and phase of pulses as short as 390 fs with femtojoule energy are accurately characterized with a high sensitivity of 18 mW^2. These all-fiber FROG architectures enable alignment-free and highly sensitive pulse characterization for the mid-IR.

Résumé

Les longueurs d'ondes de l'infrarouge moyen (2–12 μm), englobant de nombreuses empreintes moléculaires avec des transitions vibratoires fondamentales fortes, sont d'une extrême importance pour diverses applications de spectroscopie, incluant la détection militaire/chimiques, les diagnostics médicaux et la surveillance environnementale. Présentement, les sources d'infrarouge moyen disponibles sur le marché sont pour la plupart basées sur des médiums de gain tel que l'on retrouve dans les semi-conducteurs ou les gaz, ainsi que sur la conversion non linéaire de longueur d'ondes dans de gros cristaux non linéaires, ou bien des fibres de fluorure dopées aux matériaux de terres rares. De manière générale, les lasers à fibres ont l'avantage d'être hautement efficaces, d'être compactes, de posséder une fiabilité supérieure ainsi qu'une excellente qualité de faisceau. Les lasers à fibre commercialement disponibles sont pour la plupart basés sur des fibres de silice ou de fluorure. Cependant, les régions de transparence de la fibre de silice et de fluorure sont limitées à 2.5 μm et 5.5 μm respectivement, et les émissions des dopants de terres rares ne couvrent qu'une infime partie du spectre de l'infrarouge moyen. En comparaison, les verres de chalcogénure, étant de nature hautement non linéaire, possèdent une fenêtre de transparence beaucoup plus grande (jusqu'à 15 μm), permettant une émission dans virtuellement n'importe quelle longueur d'onde basée sur un gain non linéaire. Dans cette thèse, j'ai investigué les oscillateurs à fibres non linéaires basés sur les microfils de chalcogénure dans une bande de longueur d'ondes de 2 μm, qui sont très utiles pour l'identification des gaz atmosphériques tels que le CO_2, NH_3, C_2H_2, les vapeurs d'eau et autres éléments chimiques. Malheureusement, les techniques de caractérisation d'impulsions étant disponibles sur le marché, tel qu'un auto corrélateur d'intensité et un frequency-resolved optical gating (FROG), ne sont pas suffisamment sensibles afin de caractériser les impulsions de sortie. Par la suite, j'ai développé une technique de caractérisation d'impulsion FROG hautement sensible basé sur la non linéarité extrêmement élevée des microfils de chalcogénure.

Cette thèse est divisée en deux parties principales. Dans la première partie, deux approches de génération d'impulsions dans l'infrarouge moyen sont démontrées. La première approche est un laser à fibre Raman de 2 μm utilisant une microfil de chalcogénure multimatériel. Le microfil est composé d'un cœur d'As_2Se_3, d'une gaine d'As_2S_3 et d'un enrobage de méthacrylate de polyméthyl (PMMA), fournissant ainsi une compatibilité avec l'infrarouge moyen jusqu'à 10 μm avec une haute non linéarité et une excellente robustesse mécanique. Le gain Raman du microfil est caractérisée expérimentalement, et les oscillations laser Raman dans une cavité circulaire sont accomplies à un seuil de puissance crête très bas,

avec 8 nm d'accord en longueur d'onde. Les simulations numériques sont effectuées en résolvant l'équation non linéaire généralisée de Schrödinger en utilisant la méthode de Fourier en deux étapes, menant à bon accord entre la théorie et les résultats expérimentaux. La deuxième approche est un oscillateur optique paramétrique à fibre de 2 μm utilisant un microfil de chalcogénure avec une gaine de polymère Cyclo Oléfine (COP). Le microfil est hautement non linéaire et optimisé pour un gain paramétrique dans un régime de dispersion anomale. Le profil de gain paramétrique du microfil est caractérisé expérimentalement, et une oscillation paramétrique dans une cavité circulaire est obtenue à un bas seuil de puissance crête, avec 55 nm d'accordabilité en longueur d'onde et une émission totale couvrant une plage spectrale de 290 nm avec l'aide d'une génération paramétrique en cascade. La longueur d'onde de sortie de ces sources optiques peut être étendue davantage dans l'infrarouge moyen avec une optimisation de la configuration de la cavité et de la structure du microfil.

Dans la deuxième partie de cette thèse, deux approches de caractérisation d'impulsion FROG dans l'infrarouge moyen sont démontrées dans une bande de longueur d'onde de 2 μm. La première approche est une technique modifiée de caractérisation d'impulsion FROG basée sur le très efficace mélange à quatre ondes dans un microfil de chalcogénure à gaine de COP. Les tracés de FROG sont identiques à ceux obtenus à partir de FROG conventionnels basés sur une génération de deuxième harmonique. L'amplitude et la phase des impulsions picosecondes à fréquence modulée et non modulée sont caractérisées de manière précise avec une haute sensibilité de 0.16 mW^2, étant plusieurs ordres de magnitudes supérieurs à la sensitivité des FROG conventionnels. La deuxième approche est une autre technique modifiée de caractérisation d'impulsion FROG, toutefois cette fois-ci basée sur une modulation de phase croisée dans un microfil de chalcogénure à gaine de COP avec une dispersion chromatique de zéro. Sans l'ambiguïté de la direction du temps et la nécessité d'un laser sonde en émission continue,, l'amplitude et la phase des impulsions sont aussi courtes que 390 fs avec une énergie femtojoule, précisément caractérisées avec une haute sensibilité de 18 mW^2. Ces architectures FROG tout-fibres permettent une caractérisation d'impulsion très sensible et sans alignement pour l'infrarouge moyen.

Acknowledgments

First and foremost, I would like to express my gratitude to my thesis advisor Professor *Martin Rochette* for his guidance and support throughout my entire PhD research. His course on nonlinear optics introduced me to most fundamental concepts of this fascinating field, and his enthusiasm for the field deeply shaped my academic interests. His meticulous reviews of my manuscripts and presentation slides have greatly helped me improve my academic writing and presentation skills. His rigorous thinking and sharp questions have been tremendously beneficial to me for developing research skills. I have also received his gracious recommendation letters multiple times for scholarship and job applications. I am truly blessed to have such a friendly and skilled mentor.

I would like to thank all the professors in my thesis committee, Professor *Andrew Kirk* and Professor *Zetian Mi*, for their comments and suggestions throughout my qualifying exam, research proposal, and seminar. I am grateful to Professor *Lawrence Chen* for sharing fiber optic components that were indispensable for my experiments. I am also grateful to the examiners of this thesis, for their insightful and extensive comments.

I wish to thank my colleagues from whom I had the opportunity to learn. In particular, I thank *Raja Ahmad*, for introducing me to the lab facilities and chalcogenide microwire fabrication process in the beginning of my PhD research, and teaching me how to write fiber Bragg gratings into chalcogenide microwires. I have also had the pleasure of meeting him in multiple occasions after he graduated, and we had fruitful discussions about my current research and future directions. Even deeper gratitude goes to *Lizhu Li*, with whom I had worked with for the longest period of time. He assisted me in fabricating polymer-chalcogenide hybrid fibers and microwires. He was also generous with his time to have discussions about experiments and give me detailed feedback on my manuscripts. I am especially grateful to *Imtiaz Alamgir*, who helped me with fiber and microwire fabrication. The *in situ* fabrication technique that he developed made my last project possible. I am also grateful to the other members of the photonics systems group, including *Ming Ma*, *Chenglai Jia*, *Sandrine Filion-Côté*, *Imrul Kayes*, *Alexandre Rekik*, *Kaixuan Zhang*, and *Zifei Wang*, for pleasant collaborations and discussions that we had. Special thanks go to *Alexandre Rekik* for the translation of the thesis abstract to French. I also thank all the students and postdoctoral fellows in the photonics systems group, with whom I interacted during my PhD.

I am deeply grateful to Professor *Yoshiyasu Ueno* at University of Electro-communications, Tokyo, Japan. Since 2012, when I had the privilege to visit his lab as a short-term exchange student, he has been my mentor with his well-rounded knowledge in the field of optics. We

had many Skype/phone discussions on academic matters, often inspiring and enlightening to me. He also introduced me to his colleagues, such as Dr. *Matthias Jäger* in the Leibniz Institute of Photonic Technology (IPHT), when I needed expert advice on mode-locked fiber laser experiments. I greatly appreciated his stopping by Montréal in January, 2017, after his visit to the United States.

My thanks also go to the Natural Sciences and Engineering Research Council of Canada (NSERC) for financial support through research grants, and to *CorActive High-Tech Inc.*, for providing chalcogenide glass fibers and various silica glass fibers used in my experiments, some of which are described in this thesis. I also thank the administrative staff in the department of Electrical Engineering at McGill University, for their assistance throughout my PhD.

Finally, my biggest thanks go to my beloved mother, brothers, and sisters-in-law, for their continued understanding, support, and encouragement that made it possible for me to complete the PhD. I also thank all of my friends, both here in Montréal and back home, for their moral support during these years.

Contents

List of Figures

List of Tables

List of Acronyms

COP Cyclo Olefin polymer.

CW continuous-wave.

FBG fiber Bragg grating.

FOPO fiber optical parametric oscillator.

FROG frequency-resolved optical gating.

FWHM full-width at half-maximum.

FWM four-wave mixing.

GVD group velocity dispersion.

IR infrared.

MZI Mach-Zehnder interferometer.

NLSE nonlinear Schrödinger equation.

OPO optical parametric oscillator.

PMD plarization-mode dispersion.

PMMA poly-methyl methacrylate.

SHG second-harmonic generation.

SMF single mode fiber.

SPM self-phase modulation.

SRS stimulated Raman scattering.

THG third-harmonic generation.

TOD third-order dispersion.

TPA two-photon absorption.

UV ultra-violet.

WDM wavelength division multiplexing.

XPM cross-phase modulation.

Chapter 1

Introduction

Since the development of low loss silica optical fibers in 1970s, optical fibers have not only revolutionized the fields of telecommunications, sensing and power delivery [1], but also led to the emergence of the new field of nonlinear fiber optics [2]. Although rare-earth doped fibers have gained extensive success in fiber amplifiers and lasers [3], nonlinear effects in fibers have been employed to develop fiber amplifiers and lasers that can operate at any spectral range, without the restriction of dopant emission bands [4]. Because fiber based sources posses excellent beam quality, high stability without the need for careful alignment, some of them have replaced conventional solid-state lasers [5].

Thanks to the low loss and high power handling capability, silica fibers have been the most popular medium for nonlinear fiber optics applications. Enormous efforts have been devoured into the design of new fiber geometries that enhance nonlinear effects and tailor dispersion profiles, such as microstructured optical fibers (MOF) [6], photonic crystal fibers (PCF) [7] and tapered optical fibers [8]. However, due to high propagation loss in silica glass beyond the wavelength of 2 μm, the application of silica fibers as nonlinear media has been limited to the spectral range $\sim$2 μm and below. Meanwhile, chalcogenide glass fibers with high nonlinearity and wide transmission windows have emerged as one of the best candidates for nonlinear fiber optics in the mid-infrared (IR) wavelength range [9].

1.1 Motivation

Mid-infrared (IR) wavelength range (2–12 μm) is particularly important for spectroscopy applications to identify and quantify molecular species [10]. Mid-IR spectroscopy can also be used for non-instrusive biomedical diagnostics [11]. Mid-IR atmospheric windows (3–5 μm and 8–13 μm) have important applications in highly sensitive environmental monitoring [12].

Currently, commercially available mid-IR sources include quantum cascade lasers [13], optical parametric oscillators and amplifiers [14], rare-earth doped fluoride fiber lasers [15], with their respective advantages and disadvantages. Generally, fiber lasers have the advantages of high efficiency, compact size, superior reliability, and excellent beam quality. However, rare-earth doped fiber lasers can only cover a small portion of the mid-IR spectral region. In comparison, chalcogenide glasses have extremely wide transmission windows (up to 15 μm) and high intrinsic nonlinearity (up to 1000 larger n_2 than silica) [16], therefore chalcogenide fibers are capable of providing nonlinear gain at any wavelength within the transmission window. Large Raman gain in chalcogenide fibers have been used to demonstrate compact and low-threshold mid-IR Raman fiber lasers [17]. With proper design, chalcogenide microwires yield large parametric gain over wide range of wavelengths in the mid-IR [18]. In this thesis, I have developed nonlinear fiber oscillators based on Raman and parametric gain in chalcogenide microwires in the wavelength band of 2 μm, which is useful for the identification of atmospheric gasses such as CO_2, NH_3, C_2H_2, water vapor, and other chemical species. Since the reviewers of journal papers on the Raman fiber laser and optical parametric oscillator have raised questions regarding experimental characterization of output pulses, I have ventured into ultrafast pulse characterization using chalcogenide microwires, and developed all-fiber FROG pulse characterization techniques.

Robust chalcogenide microwires cladded with poly-methyl methacrylate (PMMA) polymer were developed in our lab to achieve extremely high nonlinearity and flexibly engineered dispersion [19]. Prior to the work presented in the thesis, efforts on developing nonlinear fiber sources using chalcogenide microwires focused on 1.55 μm wavelength band, where pump sources are abundant and the cladding material of PMMA has good transmission. R. Ahmad demonstrated a synchronously pumped ring-cavity Raman fiber laser [20] and a fiber optical parametric oscillator [21] based on PMMA-cladded chalcogenide microwires. Raman and parametric oscillation were also demonstrated in a Fabry-Perot cavity formed by a pair of fiber Bragg gratings (FBGs) in a PMMA-cladded chalcogenide microwire [22]. A. Al-Kadry demonstrated supercontinuum generation spanning over an octave using a PMMA-cladded chalcogenide microwire [23]. However, strong absorption in PMMA beyond the wavelength of 1.65 μm due to the second order vibrational overtone of carbon-hydrogen bonds severely limits the transmission window of PMMA-cladded chalcognide microwires, not allowing access to the mid-IR transmission windows of chalcogenide glasses. Therefore, leveraging the high nonlinearity in chalcogenide microwires in mid-IR for the development of fiber optical sources requires microwire cladding materials that are transparent in the mid-IR. In response to this challenge, L. Li developed chalcogenide microwires cladded with Cyclo Olefin polymer

(COP) in 2015, targeting nonlinear applications in the 2 μm wavelength band [24]. Excellent transmission, high nonlinearity and flexible dispersion engineering obtained in COP-cladded chalcogenide microwires paved the way for the research topics explored in this thesis.

1.2 Main contributions

The main contributions of the thesis are summarized as follows. These contributions have been published in the form of journal papers and have been presented at international conferences. First, power efficient Raman amplification and oscillation at the wavelength of 2 μm in mid-IR compatible multimaterial chalcogenide microwires are demonstrated. Second, broadband parametric amplification and widely tunable parametric oscillation in the 2 μm wavelength band are demonstrated using COP-cladded chalcogenide microwires, becoming the first ever chalcogenide-based optical parametric oscillator relying on pure parametric gain. Two different highly-sensitive techniques for FROG pulse characterization in chalcogenide microwires are developed in the 2 μm wavelength band, one is based on four-wave mixing (FWM) effect, and the other one is based on cross-phase modulation (XPM) effect in highly nonlinear and dispersion-engineered polymer-cladded chalcogenide microwires. Amplitude and phase of ultrafast pulses as short as 390 fs with femtojoule pulse energy are accurately characterized, with sensitivity levels that are orders of magnitude better than conventional FROG architectures.

1.3 Outline of the thesis

The organization of the thesis is as follows:

- Chapter 2 presents an overview of linear and nonlinear properties of chalcogenide glasses and microwires. Design considerations and fabrication process of polymer-cladded chalcogenide microwires are briefly described. Finally, modeling pulse propagation in chalcogenide microwires is presented.

- Chapter 3 presents Raman amplification and oscillation based on a multimaterial chalcogenide microwire in the 2 μm wavelength band, with a core of $As_{38}Se_{62}$, a cladding of $As_{38}S_{62}$, and coated with PMMA. Following the general theory of Raman amplification in optical waveguides, design considerations and fabrication process of the multimaterial microwire are studied. Then, experimental results of single-pass Raman amplification and ring-cavity Raman fiber laser using a pulsed pump source are detailed. Lastly, numerical simulation results of the Raman fiber laser are presented, in

excellent agreement with experimental observations. Nearly linearly chirped output Raman pulses are numerically compressed to ∼500 fs, providing important insight to the output characteristics of the Raman fiber laser.

- Chapter 4 presents parametric amplification and oscillation based on a COP-cladded chalcogenide microwire in the 2 μm wavelength band, with a core of As_2Se_3, a cladding of COP, and coated with PMMA. Following the general theory of phase-matching and parametric amplification in $\chi^{(3)}$ nonlinear media, design considerations and fabrication process of the COP-cladded microwire are detailed. Then, experimental results of single-pass parametric amplification and ring-cavity fiber optical parametric oscillator using a pulsed pump source are detailed. The parametric signal wavelength is tunable over 55 nm, which is considerably larger than the tunable range of the Raman fiber laser, which is only 8 nm, limited by the Raman gain bandwidth.

- Chapter 5 presents a FROG pulse characterization device in the 2 μm wavelength band based on efficient FWM in a COP-cladded chalcogenide microwire, similar to the one used for parametric amplification and oscillation in chapter 3. Following a brief introduction to FROG pulse characterization techniques based on second-harmonic generation (SHG) and FWM, design considerations and fabrication process of the COP-cladded microwire are detailed. Then, experimental results of complete electric field characterization are presented with chirped and unchirped picosecond pulses with femtojoule pulse energy. Accuracy of the FROG is verified through independent measurements of pulse spectra and autocorrelation traces.

- Chapter 6 presents a FROG pulse characterization device in the 2 μm wavelength band based on efficient XPM in a COP-cladded chalcogenide microwire with zero dispersion, fabricated with a recently developed *in situ* monitoring technique. Following a brief introduction to the theory XPM between orthogonally polarized optical fields and FROG pulse characterization technique based on XPM, design considerations and fabrication process of the COP-cladded microwire are detailed. Then, experimental results of complete electric field characterization are presented with femtosecond pulses as short as 390 fs with femotojoule pulse energy. Excellent agreement is found between FROG-retrieved pulse spectra and autocorrelation traces and independently measured pulse spectra and autocorrelation traces.

- Finally, Chapter 7 concludes the thesis and suggests some future work.

Relevant literature review is presented in the introduction section of each chapter, and ncessary theoretical basis is included in respective theoretical background sections. Characteristic equation for three-layer cylindrical waveguides and MATLAB numerical simulation source code for evaluating the effect of microwire core diameter fluctuation on parametric gain are provided in the appendix.

List of publications

Relevant journal publications

- **N. Abdukerim**, L. Li, M. El Amraoui, Y. Messaddeq and M. Rochette, 2 μm Raman fiber laser based on a multimaterial chalcogenide microwire. Applied Physics Letters 110(6), 161103 (2017).
  Contributions:

  N. Abdukerim: Performed experiments and prepared manuscript.
  L. Li: Microwire fabrication.
  M. El Amraoui: Fiber fabrication.
  Y. Messaddeq: Fiber fabrication.
  M. Rochette: Prepared manuscript and supervised the project.

- **N. Abdukerim**, L. Li and M. Rochette, Chalcogenide-based optical parametric oscillator at 2 μm. Optics Letters 41(18), 4364–4367 (2016).
  Contributions:

  N. Abdukerim: Performed experiments and prepared manuscript.
  L. Li: Microwire fabrication.
  M. Rochette: Prepared manuscript and supervised the project.

- **N. Abdukerim**, I. Alamgir, and M. Rochette, All-fiber frequency-resolved optical gating pulse characterization from chalcogenide glass. Optics Letters 43(14), 3228–3231 (2018).
  Contributions:

  N. Abdukerim: Performed experiments and prepared manuscript.
  I. Alamgir: Hybrid fiber fabrication.
  M. Rochette: Prepared manuscript and supervised the project.

- **N. Abdukerim**, I. Alamgir, and M. Rochette, Pulse characterization by cross-phase modulation in chalcogenide glass. Optics Letters 43(19), 4771–4774 (2018).
  Contributions:

  N. Abdukerim: Performed experiments and prepared manuscript.
  I. Alamgir: Hybrid fiber fabrication.
  M. Rochette: Prepared manuscript and supervised the project.

Relevant conference publications

- **N. Abdukerim**, L. Li and M. Rochette, Mid-infrared Raman fiber laser in chalcogenide microwire. In Photonics North, pp. 1–1, Ottawa, Ontario, June 2015.
  Contributions:

  N. Abdukerim: Performed experiments and prepared manuscript.
  L. Li: Microwire fabrication.
  M. Rochette: Prepared manuscript and supervised the project.

- **N. Abdukerim**, L. Li and M. Rochette, Chalcogenide-based optical parametric oscillator, In CLEO: Science and Innovations, STh1O.4, San Jose, California, June 2016.
  Contributions:

  N. Abdukerim: Performed experiments and prepared manuscript.
  L. Li: Microwire fabrication.
  M. Rochette: Prepared manuscript and supervised the project.

- **N. Abdukerim**, L. Li and M. Rochette, All-fiber chalcogenide Raman laser at 2 μm, In *IEEE* Photonics Society Conference (IPC), pp. 145–146, Orlando, Florida, October 2017.
  Contributions:

  N. Abdukerim: Performed experiments and prepared manuscript.
  L. Li: Microwire fabrication.
  M. El Amraoui: Fiber fabrication.
  Y. Messaddeq: Fiber fabrication.
  M. Rochette: Prepared manuscript and supervised the project.

- **N. Abdukerim**, I. Alamgir, and M. Rochette, Frequency-resolved optical gating pulse characterization with chalcogenide microwires, In Advanced Photonics Congress,

NpM4I.1, Zürich, Switzerland, July 2018.

Contributions:

N. Abdukerim: Performed experiments and prepared manuscript.

I. Alamgir: Hybrid fiber fabrication.

M. Rochette: Prepared manuscript and supervised the project.

Other Journal publications

- M. I. Kayes, **N. Abdukerim**, A. Rekik, and M. Rochette, Free-running mode-locked laser based dual-comb spectroscopy, Optics Letters 43(23), 5809-5812, (2018).
- **N. Abdukerim**, M. I. Kayes, A. Rekik, and M. Rochette, Bidirectional mode-locked thulium-doped fiber laser, Applied Optics 57(25), 7198–7202, (2018).
- L. Li, **N. Abdukerim** and M. Rochette, Mid-infrared wavelength conversion from As_2Se_3 microwires, Optics Letters 42(3), 639–642 (2017).
- C. Jia, B. J. Shastri, **N. Abdukerim**, M. Rochette, P. R. Prucnal, M. Saad, and L. R. Chen, Passively synchronized Q-switched and mode-locked dual-band Tm^{3+}: ZBLAN fiber lasers using a common graphene saturable absorber, Scientific Reports 6, 36071 (2016).
- L. Li, **N. Abdukerim** and M. Rochette, Chalcogenide optical microwires cladded with fluorine-based CYTOP, Optics Express 24(17), 18931–18937 (2016).
- L. Li, A. Al Kadry, **N. Abdukerim** and M. Rochette, Design, fabrication and characterization of PC, COP and PMMA-cladded As_2Se_3 microwires, Optical Material Express 6(3), 912–921 (2016).

Other conference publications

- I. Alamgir, **N. Abdukerim**, and M. Rochette, In situ fabrication of far-detuned optical fiber wavelength converters. In IEEE Photonics Conference (IPC), MH3.2, Reston, Virgina, October 2018.
- **N. Abdukerim**, M. I. Kayes, A. Rekik, and M. Rochette, Bidirectional mode-locked thulium-doped laser. In IEEE Photonics Conference (IPC), MH4.4, Reston, Virgina, October 2018.

- I. Alamgir, **N. Abdukerim**, and M. Rochette, In situ fabrication of far-detuned wavelength converters. In International Symposium on Non-Oxide and New Optical Glasses (ISNOG), pp. 111–112, Québec City, Québec, June 2018.

- M. I. Kayes, **N. Abdukerim**, A. Rekik, and M. Rochette, Dual comb spectroscopy with free-running bidirectional mode-locked laser at 1.92 μm. In CLEO: Science and Innovations, SW4L.6, San Jose, California, June 2018.

- L. Li, **N. Abdukerim**, and M. Rochette, Mid-infrared all-fiber widely tunable wavelength converters based on As_2Se_3-CYTOP microwires. In Advanced Photonics Congress, ITh1A.3, New Orleans, Louisiana, July 2017.

- L. Li, **N. Abdukerim**, and M. Rochette, Widely tunable mid-infrared wavelength converters based on chalcogenide microwires. In IEEE Photonics Conference (IPC), pp. 199–200, Orlando, Florida, October 2017.

- C. Jia, J. Qiao, **N. Abdukerim**, M. Rochette, L. R. Chen, Multi-wavelength Brillouin Tm^{3+}-doped fiber laser at 1873 nm using a linear cavity. In IEEE Photonics Conference (IPC), pp. 281–282, Orlando, Florida, October 2017.

- C. Jia, B. J. Shastri, **N. Abdukerim**, M. Rochette, P. R. Prucnal, L. R. Chen, and M. Saad, Passively synchronized Q-switched and simultaneous mode-locked dual-band Tm^{3+}: ZBLAN fiber laser at 1.48-and 1.85-μm using common graphene saturable absorber. In Specialty Optical Fibers, SoTu1G.4, Vancouver, British Columbia, July 2016.

- L. Li, **N. Abdukerim** and M. Rochette, Fabrication and characterization of an As_2Se_3 optical microwire cladded with perfluorinated CYTOP. In CLEO: Science and Innovations, SW4R.4., San Jose, California, June 2016.

Chapter 2

Optical properties of chalcogenide glasses and microwires

In this chapter, linear and nonlinear properties of chalcogenide glasses and microwires are introduced, followed by a description of the microwire design considerations and fabrication process. Finally, a brief introduction to modeling pulse propagation in chalcogenide microwires is provided.

2.1 Chalcogenide glasses

Chalcogenide glasses are composed of covalently bonded chalcogen elements S, Se and Te. The bandgap in chalcogenide glasses lies in the visible or near-IR region. Transmission windows of chalcogenide glasses extend well into the IR wavelength range, up to 15 μm [25]. Among many chalcogenide compounds, arsenic trisulphide (As_2S_3) and arsenic triselenide (As_2Se_3) have been developed into commercial fibers. Although rear-earth doped chalcogenide fibers have been developed, large nonlinear refractive index and Raman gain coefficient in chalcogenide glasses (up to 1000 times larger than silica) are more appealing for nonlinear fiber laser applications, such as optical parametric oscillators and Raman lasers, with the possibility of emission over the entire transmission window [26]. Photosensitivity of chalcogenide glasses is another significant advantage for writing fiber Bragg grating (FBG) structures into chalcogenide fibers to form resonant laser cavities [27]. Mid-IR Raman fiber lasers have been demonstrated in chalcogenide fibers, up to a wavelength of 3.77 μm [17,28,29]. The potential of chalcogenide glass Raman fiber lasers to cover the entire wavelength range of the 3–4 μm has been numerically demonstrated [30]. Supercontinuum generated in chalcogenide fibers have covered the entire transmission window of chalcogenide glasses [31, 32].

2.1.1 Linear properties

Long wavelength cut-off of chalcogenide glasses lies in the mid-IR thanks to large atomic masses and relatively weak inter-atomic bond strengths, which results in low phonon energies [33]. As can be seen from the Figure 2.1, sulphide glasses transmit light up to 12 μm, selenide glasses transmit light up to 15 μm, and telluride glasses transmit light up to 20 μm [34].

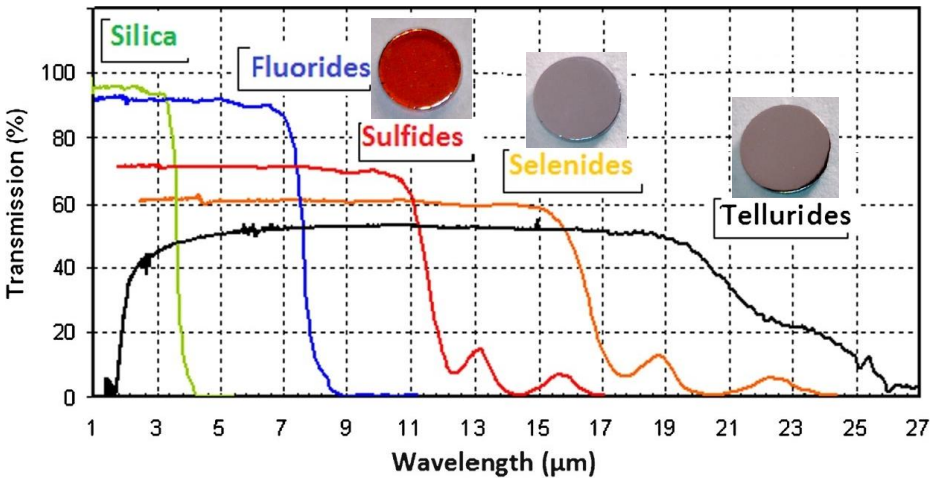

Fig. 2.1 Transmission windows of silica, fluoride and chalcogenide glasses. [Reproduced from L. Calvez, Chalcogenide glasses and glass-ceramics: Transparent materials in the infrared for dual applications. *Comptes Rendus Physique* 2017, vol. 18, pp. 314–322. Copyright ©2018 published by Elsevier Masson SAS. All rights reserved.]

Chalcogenide glasses possess large linear refractive indices. At operation wavelengths that are far away from the medium resonant frequency, the linear refractive index can be calculated by the Sellmeier equation [35]:

$$n^2(\lambda) = A_0 + \sum_{n=1}^{N} \frac{A_n \lambda^2}{\lambda^2 - \lambda_n^2}, \tag{2.1}$$

where A_0 and A_n are dimensionless coefficients, and λ_n are the material resonant wavelengths. Figure 2.2 shows the linear refractive indices of As_2Se_3 and As_2S_3 glasses as a function of wavelength, calculated using the Sellmeier coefficients provided by *Aamorphous Materials Inc.* [36].

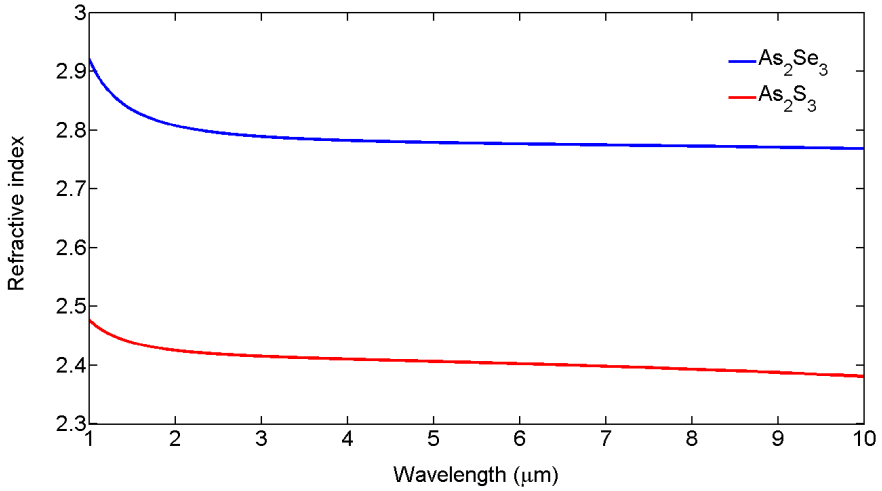

Fig. 2.2 Linear refractive indices of chalcogenide glasses

2.1.2 Nonlinear properties

The polarization **P** induced in the medium in response to the propagating optical field **E** can be expressed as a Taylor series expansion, written as

$$\mathbf{P} = \epsilon_0 \left(\chi^{(1)} \cdot \mathbf{E} + \chi^{(2)} : \mathbf{EE} + \chi^{(3)} \vdots \mathbf{EEE} + \cdots \right), \tag{2.2}$$

where ϵ_0 is the vacuum electric permittivity, and $\chi^{(j)}(j = 1, 2, 3, ...)$ is the j-th order susceptibility of the medium. In centrosymmetric media, like chalcogenide glasses, $\chi^{(3)}$ is the dominant nonlinearity, due to the absence of $\chi^{(2)}$, which is dominant in non-centrosymmetric crystals.

Nonlinear refractive index

Material nonlinear refractive index n_2 is the intensity-dependent part of refractive index, known as Kerr nonlinearity, which is related to the real part of $\chi^{(3)}$

$$n_2 = \frac{3}{8n} \operatorname{Re}\left(\chi^{(3)}\right). \tag{2.3}$$

Kerr nonlinearity is almost instantaneous. As an amorphous semiconductor material, chalcogenide materials possess very high nonlinear refractive index, which is closely related to its bandgap energy. Nonlinear refractive index n_2 of chalcogenide glasses are one of the highest in optical glasses [16]. Kerr nonlinearity gives rise to a large number of nonlinear effects, among

which widely known are self-phase modulation (SPM), cross-phase modulation (XPM), four-wave mixing (FWM) and third-harmonic generation (THG) [2]. Imaginary part of $\chi^{(3)}$ gives the intensity-dependent nonlinear absorption coefficient, known as two-photon absorption (TPA):

$$\alpha_2 = -\frac{3k_0}{4n} \operatorname{Im}\left(\chi^{(3)}\right). \tag{2.4}$$

TPA in chalcogenide glasses dwindles as the wavelength increases, and becomes negligible beyond 1.75 μm in the case of As_2Se_3 [37].

Figure 2.3 shows nonlinear refractive index and TPA coefficient of As_2Se_3 and As_2S_3 as a function of wavelength, calculated by a combination of two-level orbital approximation method [38] and the dispersion of the Kerr coefficient for crystalline solids based on Kramers-Kronig relations [39, 40].

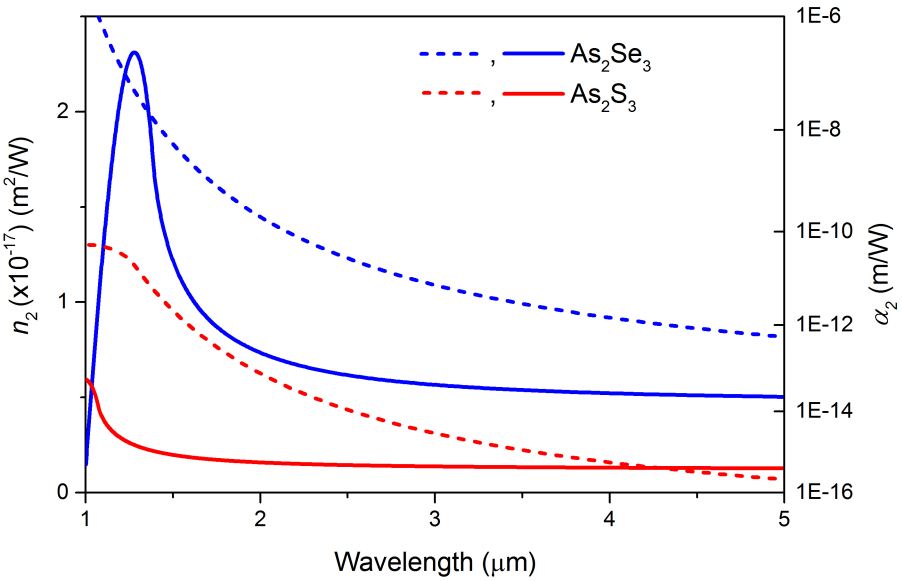

Fig. 2.3 Nonlinear refractive indices (solid lines) and two-photon absorption coefficients (dashed lines) of two common chalcogenide glasses.

Inelastic nonlinear scattering

Raman scattering of light in a material yields structural and dynamic information on a molecular level. A photon scatters to a lower frequency photon and an optical phonon. The energy of the phonon is equal to the difference in energies of pump and scattered photons, determined by the material composition. Since it is the molecular response to

the optical field, Raman scattering has a finite response time. The dominant feature in binary sulfide and selenide compounds are bands centered at 345 cm^{-1}(As_2S_3) and 230 cm^{-1} (As_2Se_3), respectively [41]. Raman gain coefficient g_R of bulk material is related to Raman susceptibility χ^R through the expression [42]

$$g_R(\omega_S) = \frac{3\omega_S}{c_0 n_S} \operatorname{Im}\left(\chi^R(\omega_S)\right), \tag{2.5}$$

where n_S is the linear refractive index at the Stokes frequency ω_S. The nonlinear response function $R(t) = (1 - f_R)\delta(t) + f_R h_R(t)$ describes both the instantaneous Kerr ($\delta(t)$) effect and the delayed Raman ($h_R(t)$) effect, where f_R is the fractional Raman contribution and $\int_0^\infty h_R(t)dt = 1$ [43]. $h_R(t)$ can be determined by the experimentally measured Raman gain spectrum $g_R(\Omega)$ and nonlinear refractive index n_2 through

$$g_R(\Omega) = \frac{2\omega_P}{c_0} n_2 f_R \operatorname{Im}\left(H_R(\Omega)\right), \tag{2.6}$$

where ω_P is the pump frequency, and $H_R(\Omega)$ is the Fourier transform of $h_R(t)$. The real part of $H_R(t)$ can be determined by the Kramers-Kronig relations using Hilbert transformation [43]. The Raman response function $h_R(t)$ usually takes the form of damped oscillation [2], which is represented by a Lorentzian profile

$$h_R(t) = \frac{\tau_1^2 + \tau_2^2}{\tau_1 \tau_2^2} \exp(-t/\tau_2) \sin(t/\tau_1), \tag{2.7}$$

where τ_1 comes from the measured Raman frequency shift, and τ_2 comes from the measured Raman gain bandwidth. Figure 2.4 shows experimentally measured normalized Raman gain spectra of chalcogenide glasses compared with that of silica [44]. Although silica glass has a wider Raman gain bandwidth, peak values of Raman gain coefficient in chalcogenide glasses are up to 800 times larger than that of silica glass. Table 2.1 summarizes the Raman response function and Raman gain coefficients of silica and chalcogenide glasses.

Table 2.1 Raman response function and Raman gain coefficients of silica and chalcogenide glasses at $\lambda = 1.55$ μm

Material	τ_1 (fs)	τ_2 (fs)	f_R	g_R (m/W$\times 10^{-13}$)
Silica [45]	12.2	32	0.18	0.65
As_2S_3 [46]	15.5	230.5	0.148	43
As_2Se_3 [47]	23	164.5	0.1	510

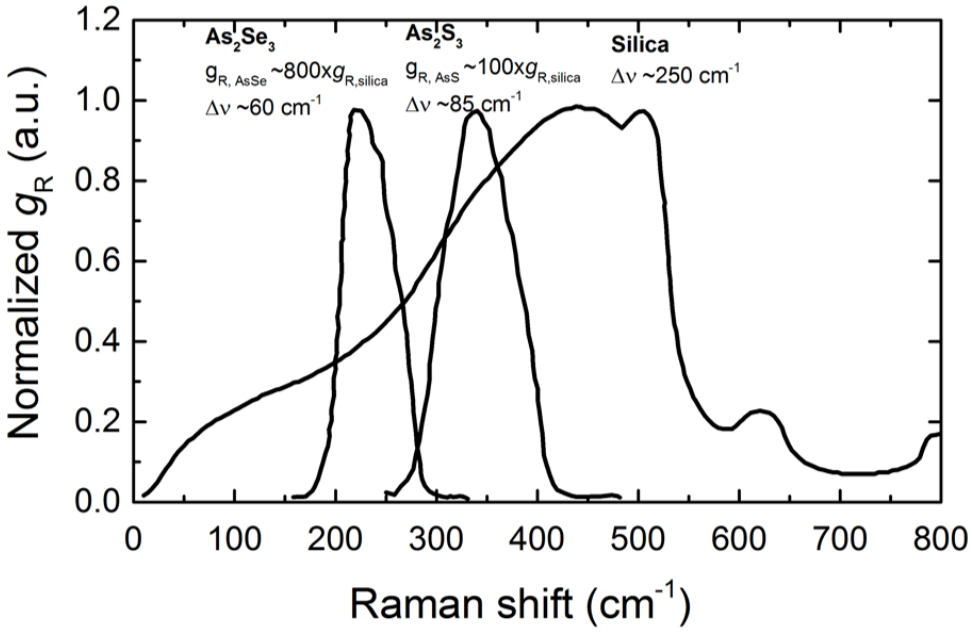

Fig. 2.4 Raman gain spectra of silica and chalcogenide glasses. [Reproduced from J. S. Sanghera, I. D. Aggarwal, L. B. Shaw, C. M. Florea, Nonlinear properties of chalcogenide glass fibers. Journal of Optoelectronics and Advanced Materials 2006, 8(6), pp. 2148–2155. Copyright ©2018 published by INOE & INFM. All rights reserved.]

Brillouin scattering is another form of inelastic nonlinear scattering that often happens in optical fibers and waveguides, in which a photon scatters to a lower frequency photon and an acoustic phonon. Remarkably different from Raman scattering, acoustic phonons participate in the Brillouin scattering process, and the Brillouin frequency shift is smaller than Raman frequency shift by three orders of magnitude. Brillouin gain spectrum also has Lorentzian shape, given by [2]

$$g_B(\Omega) = \frac{2\pi n^7 p_{12}^2}{c_0 \lambda_P^2 \rho v_A \Delta\nu_B}, \tag{2.8}$$

where p_{12} is the longitudinal photoelastic constant of the material, ρ is the density of the material, λ_P is the pump wavelength, $\Delta\nu_B$ is the Brillouin gain bandwidth, and v_A is the acoustic wave velocity. Ogusu et al. have estimated g_B in chalcogenide glasses, and reported values of up to 25 times larger than g_B of silica glass, as shown in table 2.2 [48].

Table 2.2 Brillouin gain coefficients of silica and chalcogenide glasses at $\lambda = 1.06\ \mu$m

Material	ν_B (GHz)	$\Delta\nu_B$ (MHz)	g_B (m/W$\times 10^{-11}$)
Silica	16.3	69.6	2.24
As_2S_3	12.2	239.3	48.2
As_2Se_3	11.3	328.5	53.2

2.2 Chalcogenide microwires

When a piece of fiber is heated and stretched to subwavelength outer diameters, the fiber core vanishes and surrounding air becomes the cladding, while the original fiber cladding becomes the microwire core. Figure 2.5 shows the typical structure of a tapered fiber. The central section, as called microwire, exhibits significantly enhanced waveguide nonlinearity and engineerable dispersion, due to strong modal confinement by the large core-to-cladding refractive index contrast. Enhanced nonlinearity was experimentally observed in tapered silica fibers in 1993 [49]. Since then, many numerical and experimental results have been reported with tapered fibers. In 2007, Mägi et al. reported first demonstration of a chalcogenide microwire, with a diameter of 1.2 μm and resulting in a nonlinear coefficient of 68 $W^{-1}m^{-1}$ [50]. However, this microwire was air-cladded and therefore vulnerable to mechanical damage and contamination.

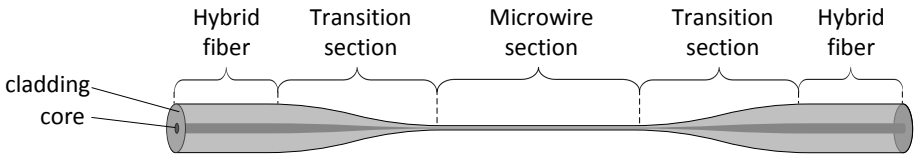

Fig. 2.5 Schematic of a typical tapered fiber.

Robust polymer-cladded chalcogenide microwires were developed in our lab. In 2010, Baker et al. demonstrated As_2Se_3 microwires with poly-methyl methacrylate (PMMA) cladding [19, 51]. The PMMA cladding helps engineering overall dispersion and provides optical and mechanical protection, thus enabling normal handling without damage. As the nonlinearity is increased, Raman gain is also enhanced in microwires. Furthermore, with appropriate design, efficient phase-matching can be achieved for parametric processes at any wavelength below the zero-dispersion wavelength of bulk chalcogenide. Since the transmis-

sion window of chalcogenide fiber extends well into mid-IR region and two-photon absorption (TPA) becomes negligible at wavelengths >1.75 μm [37], it is promising to develop mid-IR fiber sources based on large nonlinear gain in chalcogenide microwires.

2.2.1 Linear optical parameters

Effective refractive index

Light propagation in a waveguide is restricted by transverse modal extension, therefore the propagation constant of the guided mode is given by the following equation:

$$\beta = \frac{2\pi n_{eff}}{\lambda}, \tag{2.9}$$

where λ is the optical wavelength of the guided mode, and n_{eff} is called effective refractive index, which is determined by refractive indices of core and cladding materials, and the waveguide geometry. The effective refractive index is the ratio of the velocity of light in vacuum to the phase velocity of a mode in the direction of propagation in the waveguide. For a step index fiber or microwire with core diameter a, which is a cylindrical optical waveguide, made of core material with refractive index n_1 and cladding material with refractive index n_2, the effective refractive index can be found from the characteristic equation [52]:

$$\left[\frac{J_v'(u)}{uJ_v(u)} + \frac{K_v'(w)}{wK_v(w)}\right]\left[\frac{n_2^2}{n_1^2}\frac{J_v'(u)}{uJ_v(u)} + \frac{K_v'(w)}{wK_v(w)}\right] = v^2\left(\frac{1}{u^2}+\frac{1}{w^2}\right)\left(\frac{n_2^2}{n_1^2}\frac{1}{u^2}+\frac{1}{w^2}\right). \tag{2.10}$$

where $u^2 = (2\pi n_1 a/\lambda)^2 - (\beta a)^2$, and $w^2 = (\beta a)^2 - (2\pi n_2 a/\lambda)^2$. The Bessel function J_v describes the electric field in the fiber core, while the modified Bessel function of second kind K_v describes the electric field in the cladding. The fundamental mode of a step index fiber has the largest β among all the guided modes. However, for a three layer microwire, especially when the electric field expands into outer cladding with refractive index of n_3, more rigorous form of the characteristics equation has to be derived. If $n_1 > n_2 > n_3$ ($a_2 > a_1$), a modified Bessel function of third kind I_v can be used to describe the electric field in the outer cladding. Using boundary conditions of the electromagnetic field, we can obtain the characteristic equations shown in appendix A.2.

Part of the guided mode electric field propagates in the cladding as evanescent field, therefore confinement factor Γ is used to quantify the amount of optical power confined

within the boundaries of the fiber core P_{core} as compared to the total optical power P_{total}:

$$\Gamma = \frac{P_{\text{core}}}{P_{\text{total}}} = \frac{\int_0^a \int_0^{2\pi} \text{Re}(\mathbf{E} \times \mathbf{H}^*) \cdot \hat{z} r dr d\phi}{\int_0^\infty \int_0^{2\pi} \text{Re}(\mathbf{E} \times \mathbf{H}^*) \cdot \hat{z} r dr d\phi}, \tag{2.11}$$

where a is the microwire core radius, $\mathbf{E}$ is the electric field and $\mathbf{H}$ is the magnetic field in a cylindrical coordinate. The microwire propagation loss α_{total} can then be derived from the core material loss α_{core} and cladding material loss α_{cladding}:

$$\alpha_{\text{total}} = \Gamma \alpha_{\text{core}} + (1 - \Gamma)\alpha_{\text{cladding}}. \tag{2.12}$$

Dispersion

Chromatic dispersion in the microwire is a combination of material dispersion and waveguide dispersion. The microwire dispersion can be expressed by a Taylor expansion of the propagation constant β about the central angular frequency ω_0:

$$\beta(\omega) = n_{eff}(\omega)\frac{\omega}{c_0} = \beta_0 + \beta_1(\omega - \omega_0) + \frac{1}{2}\beta_2(\omega - \omega_0)^2 + \frac{1}{6}\beta_3(\omega - \omega_0)^3 + ..., \tag{2.13}$$

where

$$\beta_m = \left(\frac{d^m \beta}{d\omega^m}\right)_{\omega=\omega_0} \qquad (m = 0, 1, 2, ...), \tag{2.14}$$

where β_0 is the propagation constant at the frequency ω_0, and $\beta_1 = 1/v_g$ (v_g is the group velocity). β_2 represents the group velocity dispersion (GVD) and is responsible for pulse broadening, β_3 is the slope of GVD, while β_4 and the rest are higher-order dispersion terms. The sign of β_2 determines whether "blue" or "red" wavelengths travel faster in the medium. In "normal dispersion" ($\beta_2 > 0$), longer wavelengths travel faster than shorter ones, whereas the opposite is true in "anomalous-dispersion" ($\beta_2 < 0$).

It is worth mentioning that the difference in group velocities for pulses with different wavelengths lead to limited nonlinear interaction length between pulses due to the walk-off effect. The walk-off parameter d between two pulses with central wavelengths λ_1 and λ_2 is defined as

$$d = \beta_1(\lambda_1) - \beta_1(\lambda_2) = v_g^{-1}(\lambda_1) - v_g^{-1}(\lambda_2), \tag{2.15}$$

for pulses of width T_0, the walk-off length $L_{WO} = T_0/|d|$.

2.2.2 Nonlinear optical parameters

Waveguide nonlinearity parameter γ is an important parameter in the design of chalcogenide microwires for nonlinear applications, defined as

$$\gamma = \frac{k_0 \overline{n}_2}{A_{eff}}, \tag{2.16}$$

where k_0 is the wavenumber, and $\overline{n}_2$ is nonlinear refractive index averaged over the inhomogeneous cross section weighted to the electric field distribution [53], given by

$$\overline{n}_2 = \frac{\epsilon_0}{\mu_0} \frac{\iint_\infty n_0^2(x,y) n_2(x,y) \left[2|\mathbf{E}|^4 + |\mathbf{E}^2|^2\right] dA}{3 \iint_\infty |\mathbf{E} \times \mathbf{H}^* \cdot \hat{z}|^2 dA}, \tag{2.17}$$

where A is the cross section area, and A_{eff} is the effective area of the propagating mode, which is determined purely by the material linear refractive index $n(x,y)$, given by

$$A_{eff} = \frac{\left|\iint_\infty (\mathbf{E} \times \mathbf{H}^*) \cdot \hat{z} dA\right|^2}{\iint_\infty |(\mathbf{E} \times \mathbf{H}^*) \cdot \hat{z}|^2 dA}. \tag{2.18}$$

Likewise, for microwires with small core diameter and high confinement factor, the effective Raman gain coefficient would be different from the Raman gain coefficient g_R of the bulk material, and it takes the form [54]

$$\overline{g}_R = \frac{\epsilon_0^2 c_0^2 \int g_R n(x,y)^2 |\mathbf{E}_P \cdot \mathbf{E}_S^*|^2 dA}{\int (\mathbf{E}_P^* \times \mathbf{H}_P \cdot \hat{z}) (\mathbf{E}_S^* \times \mathbf{H}_S \cdot \hat{z}) dA}, \tag{2.19}$$

where $\mathbf{E}_P$ and $\mathbf{H}_P$ are pump electromagnatic field, and $\mathbf{E}_S$ and $\mathbf{H}_S$ are Stokes electromagnetic field.

2.2.3 Fabrication

Polymer-cladded chalcogenide microwire fabrication process involves multiple steps. It starts with drying PMMA and Cyclo Olefin polymer (COP) tubes in the vacuum oven at ∼105 °C for several days to prepare for the fabrication of preforms and hybrid fibers. A bulk chalcogenide rod is then inserted into a COP capillary tube, and the assembly is inserted into a PMMA tube. Then, the polymer tubes are collapsed on the chalcogenide rod through a heated funnel to form the preform. The preform is then heated and stretched to obtain a hybrid fiber with a chalcogenide core diameter optimized for maximum coupling efficiency

to single-mode silica fibers. Both ends of a segment of hybrid fiber are polished, and the initial core diameter is measured under the microscope prior to the microwire fabrication. The microwire core diameter is designed to achieve desired dispersion profile and nonlinear parameter for the target application. The fabrication of the microwire is completed by a multi-step horizontal heat-brush technique [55], based on a predetermined tapering profile that ensures adiabaticity. Figure 2.6 shows a schematic of polymer-cladded chalcogenide microwire fabrication setup. Two translation stages pull the hybrid fiber in opposite directions at a constant velocity, while the heater element mounted on another translation stage moves back and forth with increasing distance as the microwire gets longer. The heater temperature is programmed to gradually decrease throughout the microwire fabrication process. The hybrid fiber can be butt-coupled at both ends to silica fiber pigtails using UV-cured epoxy prior to the microwire fabrication for *in situ* monitoring of microwire transmission and dispersion evolution [56].

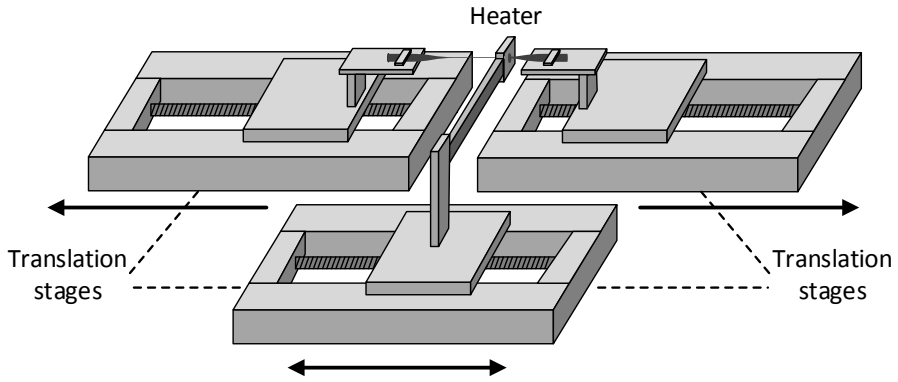

Fig. 2.6 Schematic of the polymer-cladded chalcogenide microwire fabrication setup.

2.3 Pulse propagation in microwires

Being an electromagnetic wave, light propagation in optical waveguides is governed by the Maxwell's equations, from which the following wave equation for the electric field can be obtained [2]:

$$\nabla^2\mathbf{E} - \frac{1}{c^2}\frac{\partial^2\mathbf{E}}{\partial t^2} = \mu_0\frac{\partial^2\mathbf{P}_L}{\partial t^2} + \mu_0\frac{\partial^2\mathbf{P}_{NL}}{\partial t^2}, \tag{2.20}$$

where $\mathbf{P}_L$ and $\mathbf{P}_{NL}$ are the linear and nonlinear parts of the induced polarization, respectively. By using the method of separation of variables, the electric field can be written as

$$\mathbf{E}(\mathbf{r},t) = \frac{1}{2}\hat{x}\left\{F(x,y)A(z,t)exp\left[i(\beta_0 z - \omega_0 t)\right] + c.c.\right\}, \tag{2.21}$$

where $\hat{x}$ is the polarization unit vector, $A(z,t)$ is the slowly varying pulse envelope, $F(x,y)$ is the modal distribution of the electric field in the waveguide, ω_0 is the central angular frequency, β_0 is the wave number, and $c.c.$ denotes the complex conjugate. After some mathematical derivation, the generalized nonlinear Schrödinger equation (NLSE) can be obtained for the pulse envelope $A(z,t)$ [2]:

$$\begin{aligned}\frac{\partial A}{\partial z} + \frac{1}{2}\left(\alpha + i\frac{d\alpha}{d\omega}\frac{\partial}{\partial t}\right)A \; + \; \sum_{m=1}^{M} i^{m-1}\frac{\beta_m}{m!}\frac{\partial^m A}{\partial t^m} \\ = i\left(\gamma + i\frac{\alpha_2}{2A_{eff}} + i\frac{d\gamma}{d\omega}\frac{\partial}{\partial t}\right)\left(A(z,t)\int_0^\infty R(\tau)|A(z,t-\tau)|^2 d\tau\right),\end{aligned} \tag{2.22}$$

where β_m is the m-th order dispersion coefficient, and M denotes the order up to which dispersive effects are included. The integral represents for the energy transfer as a result of intrapulse Raman scattering. Assuming a reference time frame moves with the pulse at the group velocity v_g, obtained by the transformation $T = t - z/v_g = t - \beta_1 z$, the NLSE can then be written in the form

$$\frac{\partial A}{\partial z} = \left(\hat{D} + \hat{N}\right)A, \tag{2.23}$$

where $\hat{D}$ is the linear operator that accounts for dispersion and losses, while $\hat{N}$ is the nonlinear operator that accounts for nonlinear effects and nonlinear absorption, given by

$$\begin{aligned}\hat{D} &= -\sum_{m=2}^{M} i^{m-1}\frac{\beta_m}{m!}\frac{\partial^m}{\partial T^m} - \frac{1}{2}\left(\alpha + i\frac{d\alpha}{d\omega}\right), \\ \hat{N} &= i\left(\gamma + i\frac{\alpha_2}{2A_{eff}} + i\frac{d\gamma}{d\omega}\frac{\partial}{\partial T}\right)\left(\int_0^\infty R(\tau)|A(z,t-\tau)|^2 d\tau\right).\end{aligned} \tag{2.24}$$

The NLSE can be numerically solved by the split-step Fourier method, by independently applying the linear and nonlinear operators over a small distance h. The obtained solution is approximate, and accurate to second order in the step size h [2].

Chapter 3

Raman fiber laser based on multimaterial chalcogenide microwires

[1]In this chapter, we report a Raman fiber laser based on a multimaterial chalcogenide microwire. The microwire structure comprises a core of $As_{38}Se_{62}$, a cladding of $As_{38}S_{62}$, and a coating of poly-methyl methacrylate. The microwire is a robust, high confinement waveguide compatible with the mid-infrared. With the microwire inserted in a ring cavity, Raman laser oscillation at a wavelength of 2.025 μm occurs from synchronous pumping at a wavelength of 1.938 μm. The input peak power required to reach threshold is 6.6 W and the power slope efficiency is 4.5%. Numerical simulations are in good agreement with experimental results and predict chirp-free femtosecond pulses.

3.1 Introduction

The Raman gain is of widespread use in laser cavities, especially convenient to generate light at any wavelength for which resonant gain media are not available [4]. In silica fibers, the Raman gain provided by silica has led to Raman fiber lasers [57]. Various forms of continuous-wave (CW) and pulsed Raman fiber lasers have been extensively studied [58–62]. Previous studies using the Raman gain in silica fibers mostly focused on the wavelength range of 1.0–1.6 μm for imaging and telecommunications related applications. Targeting emission wavelengths beyond 2 μm for biomedical and chemical sensing applications, Raman fiber lasers have been demonstrated using GeO_2-doped silica fibers but the low Raman gain

[1]Part of the content in this chapter has been subject to publication in (1) N. Abdukerim, L. Li, M. El Amraoui, Y. Messaddeq and M. Rochette, 2 μm Raman fiber laser based on a multimaterial chalcogenide microwire, Applied Physics Letters 110, 161103 (2017).

coefficient combined with high transmission losses of silica led to high power threshold and low efficiency [63].

As described in chapter 2, chalcogenide glasses have a Raman gain coefficient as high as 800 times that of silica, and wide transmission windows extending up to 11 μm (As_2S_3) and 16 μm (As_2Se_3) in the mid-infrared [26, 64, 65]. These properties bring chalcogenide fibers as excellent candidates for the development of Raman fiber lasers at wavelengths in the mid-infrared. To date, only a few Raman lasers based on chalcogenide fibers have been reported [17, 20, 28, 66]. One of them provides the longest wavelength for Raman fiber lasers with 3.77 μm [28]. At the exception of one report showing an all-fiber design [20], every demonstration relied on free-space optics for pump coupling, making the laser prone to misalignment. The main limitation of the all-fiber concept presented in [20] is the polymethyl methacrylate (PMMA) cladding directly applied over the chalcogenide core of the Raman gain medium, impairing transmission in the mid-infrared.

With an aim towards compact and low-power consumption Raman fiber lasers, the access to a large waveguide nonlinearity coefficient of the gain medium is of prime concern. Tapered microwires benefit from a large increase in the waveguide nonlinearity coefficient by hundreds of times with respect to their untapered counterpart [49, 50]. Although high numerical aperture optical fibers with dual-material core-cladding composition (e.g. polymers, As_2Se_3, As_2S_3) have served to build robust microwires [19, 24, 55, 67], mid-IR transmission is severely limited by the absorption in polymer cladding. In response to this, we have developed a multimaterial chalcogenide microwire, both core and cladding comprising chalcogenide glasses, with excellent mid-IR transparency as well as mechanical robustness.

In this chapter, we demonstrate an all-fiber Raman laser based on a multimaterial microwire. The microwire consists of a 10 cm long waveguide with a core of $As_{38}Se_{62}$ and a cladding of $As_{38}S_{62}$ coated with PMMA. This microwire provides a strong Raman gain and enables the laser threshold to occur at a peak power as low as 6.6 W. In the microwire, light is confined by mid-infrared compatible materials of an $As_{38}Se_{62}$ core and an $As_{38}S_{62}$ cladding. The microwire is thus a promising candidate for the fabrication of mid-infrared sources that are compact and operate with low-power consumption. Numerical simulations are carried out and predict that the experimentally obtained Raman pulses are linearly chirped and could be compressed to ~500 fs, which is 14 times shorter than pump pulses, showing that the Raman fiber laser is capable of converting picosecond pulses to femtosecond pulses.

3.2 Theoretical background

In the absence of pump depletion, Raman gain in the microwire can be estimated by:

$$G = \exp(\overline{g}_R P_0 L_{eff}/A_{eff}), \tag{3.1}$$

where $\overline{g}_R$ is obtained from equation 2.19, and effective length $L_{eff} = [1 - \exp(-\alpha L)]/\alpha$, for a microwire with length L and attenuation coefficient α.

In the case of pulsed pumping, more rigorous evaluation of Raman amplification can be obtained by solving the coupled amplitude equations [2]:

$$\begin{aligned}
\frac{\partial A_p}{\partial z} + \frac{i\beta_{2p}}{2}\frac{\partial^2 A_p}{\partial T^2} &= i\gamma_p\left[|A_p|^2 + (2+\delta_R - f_R)|A_s|^2\right]A_p - \left(\frac{\overline{g}_p}{2}|A_s|^2 + \frac{\alpha_p}{2}\right)A_p, \\
\frac{\partial A_s}{\partial z} - d\frac{\partial A_s}{\partial T} + \frac{i\beta_{2s}}{2}\frac{\partial^2 A_s}{\partial T^2} &= i\gamma_s\left[|A_s|^2 + (2+\delta_R - f_R)|A_p|^2\right]A_s + \left(\frac{\overline{g}_s}{2}|A_p|^2 - \frac{\alpha_s}{2}\right)A_s,
\end{aligned} \tag{3.2}$$

where subscripts p and s denote pump and Stokes parameters, f_R is the fractional Raman contribution, δ_R is the Raman-induced index change, and d is obtained from equation 2.15. Spontaneous Raman scattering can also be included by adding a noise term.

Cascaded Raman scattering can be utilized to scale the output wavelength of Raman fiber lasers even further [17, 68–70]. In fact, cascaded Raman scattering has been experimentally observed in chalcogenide fibers up to eighth order [64, 69, 71].

3.3 Microwire design and fabrication

The microwire fabrication includes arsenic (As), sulfur (S) and selenium (Se) batched from commercially available elements with purity higher than 99.9999%. The raw materials are placed under vacuum into a sealed silica ampoule and then heated up to 700–800 °C for several dozen hours, quenched in water, and annealed at approximately 170 °C to remove mechanical stress. The core and cladding glass compositions are $As_{38}Se_{62}$ and $As_{38}S_{62}$, respectively. The dual-material $As_{38}Se_{62}/As_{38}S_{62}$ fiber is then drawn by a double crucible method [72]. The dual-chalcogenide fiber is coated with PMMA to result into a multimaterial fiber that enables the fabrication of robust microtapers following the technique detailed in [19, 55].

Figure 3.1 presents the geometry of a typical microtaper. It is subdivided into multimaterial fibers on both ends, two intermediate transition sections, and a microwire at the center.

Figure 3.1 shows the reflection optical micrograph of a typical multimaterial fiber facet. Both multimaterial fiber ends are butt-coupled to SMF-28 fibers via UV epoxy, resulting into a total insertion loss of 6 dB at a wavelenth of 2 μm, including 0.1 dB/cm of propagation loss, 0.5 dB per interface due to Fresnel reflection loss at chalcogenide-silica interfaces, and the rest is attributed to mode-mismatch and misalignment losses.

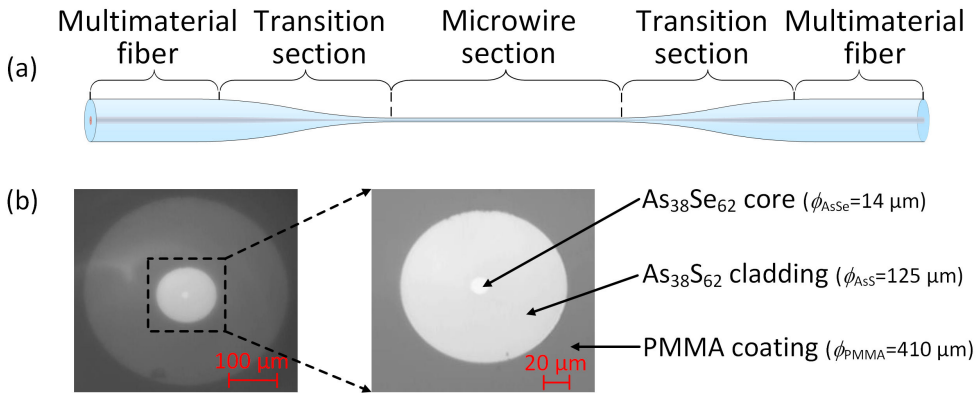

Fig. 3.1 Schematic of a typical chalcogenide microwire.

From equation 2.19, effective Raman gain coefficient $\overline{g}_R$ is a function of microwire core diameter, and A_{eff} in equation 3.1 also exhibits a maximum value. Therefore overall Raman gain in the microwire could be optimized by maximizing $\overline{g}_R/A_{eff}$, as shown in Figure 3.2.

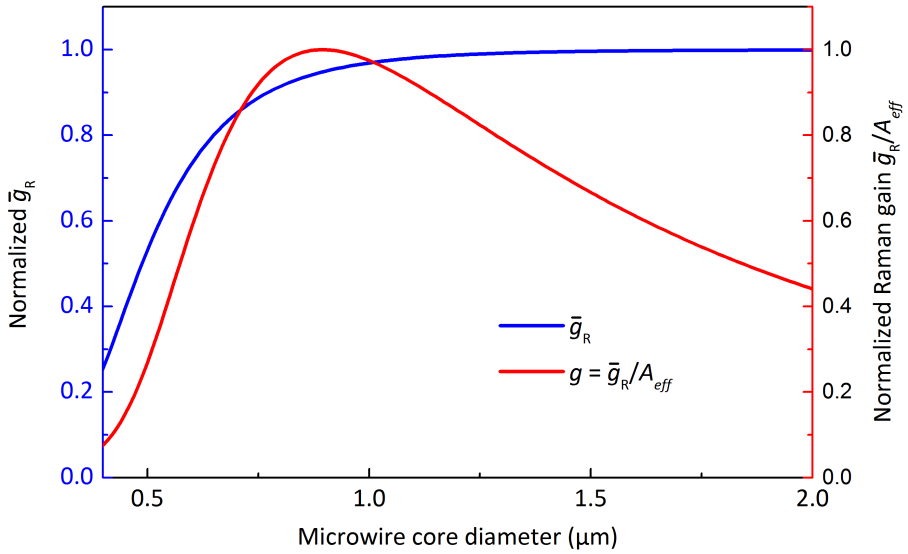

Fig. 3.2 Normalized effective Raman gain coefficient and Raman gain in the multimaterial microwire as a function of core diameter.

The microwire is designed with a core diameter of 0.85 μm to achieve a minimum effective mode area $A_{eff} = 0.92\,\mu\text{m}^2$ at the wavelength of 1.94 μm and thus maximize the Raman gain. In the microwire, the fundamental optical mode is tightly confined in the $As_{38}Se_{62}$ core ($n_{\text{AsSe}} = 2.81$) due to large refractive index contrast with respect to the $As_{38}S_{62}$ cladding ($n_{\text{AsS}} = 2.41$). The chosen diameter also leads to chromatic dispersion that is normal with $\beta_2 = 1.67\,\text{ps}^2/\text{m}$, ensuring pure Raman operation without modulation instability. The transmission window of the microwire is only limited by the common transmission windows of $As_{38}Se_{62}$ and $As_{38}S_{62}$, which spans from 1.5 μm up to 11.0 μm , thus making this microwire compatible with mid-infrared applications.

3.4 Raman amplification in chalcogenide microwire

In this experiment, the Raman gain of the microwire is characterized. Figure 3.3(a) shows a schematic of the pump-probe experimental setup. The pump is a thulium-doped mode-locked fiber laser that emits pulses at a wavelength of 1.938 μm, with a full-width at half-maximum (FWHM) duration of 800 fs, and at a repetition rate of 30 MHz. A 100 m long spool of SMF-28 fiber is used to broaden pump pulses before amplification by a thulium-doped fiber amplifier, to avoid nonlinear effects and pulse distortion in the fiber amplifier. Amplified pulses are subsequently filtered by a 2 nm tunable bandpass filter to eliminate amplified spontaneous emission from the fiber amplifier. Resulting pulses have a FWHM duration of $\sim$7 ps. The probe is a CW thulium-doped fiber laser constructed as shown in Figure 3.3(b) [73]. The ring cavity fiber laser is pumped in forward direction through a 1550/2000 wavelength division multiplexing (WDM) coupler, and a tunable bandpass filter is used to select the oscillating wavelength. A polarization controller followed by a polarization-dependent isolator is used to ensure linear polarization and unidirectional operation. 20% of the laser power in the cavity is coupled out via an 80/20 output coupler. Output wavelength is tunable in between 1.900 μm and 2.036 μm, with a linewidth <0.05 nm, limited by optical spectrum analyzer resolution bandwidth. Pump and probe are coupled into the microwire by an 80/20 fiber coupler. The peak pump power coupled into the microwire is 2.85 W, and the CW probe power coupled into the microwire is 0.021 mW independently of the wavelength. A polarization controller (PC) is inserted in both the pump and probe arms to align their polarization states in the microwire. Raman gain is measured as a function of probe wavelength from 2.009 μm to 2.036 μm, where the longest wavelength is limited by the tunable range of the probe laser. Output spectra are recorded with an optical spectrum analyzer, with resolution bandwidth set to 1 nm.

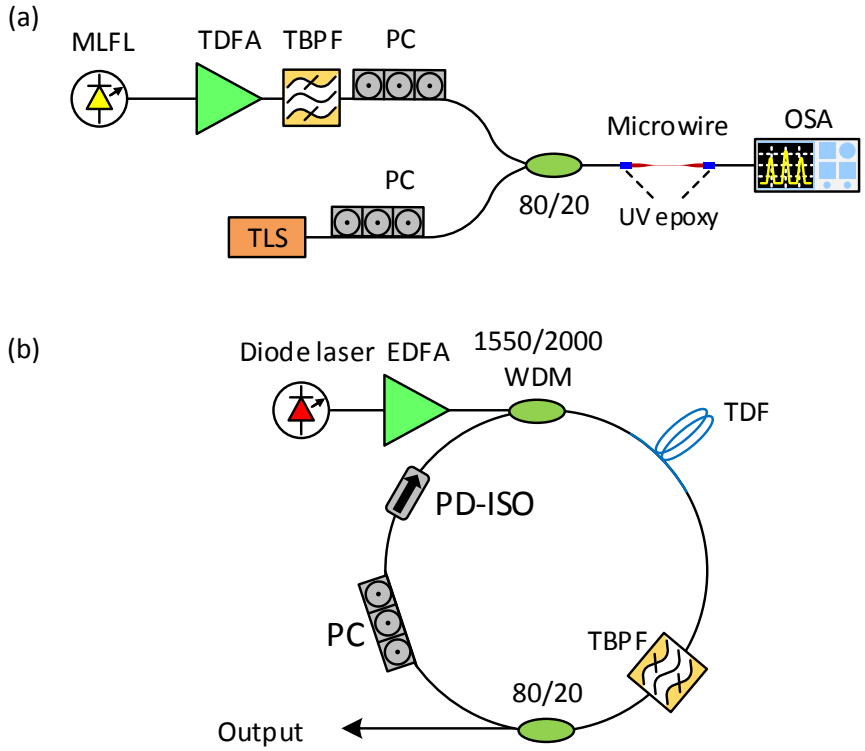

Fig. 3.3 (a) Schematic of the characterization setup for Raman amplification. MLFL, mode-locked fiber laser; TDFA, thulium-doped fiber amplifier; TBPF, tunable bandpass filter; PC, polarization controller; TLS, tunable laser source; OSA, optical spectrum analyzer. (b) Schematic of the wavelength tunable thulium-doped fiber laser. WDM, wavelength division multiplexer; PD-ISO, polarization-dependent isolator.

When a pump pulse propagates in the microwire along with a CW probe, a portion of the probe gets amplified by Raman gain in time domain, and it is manifested in optical spectrum as amplified side lobes. Figure 3.4(a) shows the amplified spectra and extracted Raman gain at different probe wavelengths λ_P. Spectral broadening of the probe signal occurs from cross-phase modulation, and it is amplified by Raman gain. The Raman gain at each wavelength is extracted by integrating the amplified spectra without the CW probe, and illustrated by red triangles. The contour line shows the Raman gain profile, and dashed part of the contour line is extrapolated to show the expected gain profile at longer wavelengths. Maximum Raman gain of 18.4 dB occurs at 2.030 μm or a wavelength shift of 92 nm, corresponding to a Raman frequency shift of 7.07 THz or 236 cm^{-1}, in agreement with pre-

viously reported values [26]. Figure 3.4(b) shows the Raman response function of $As_{38}Se_{62}$ extracted from Lorentzian curve fitting to the measured Raman gain [43]. Based on equation 2.7, extracted time constants are $\tau_1 = 22.5\,\text{fs}$ and $\tau_2 = 342\,\text{fs}$. Using fractional contribution of delayed Raman response $f_R = 0.1$ and nonlinear refractive index $n_2 = 7.6\times10^{-18}\,\text{m}^2/\text{W}$ at $1.94\,\mu\text{m}$ [39], the peak Raman gain coefficient of $As_{38}Se_{62}$ is estimated from equation 2.6 at $g_R = 2.2\times10^{-11}\,\text{m/W}$ at the pump wavelength.

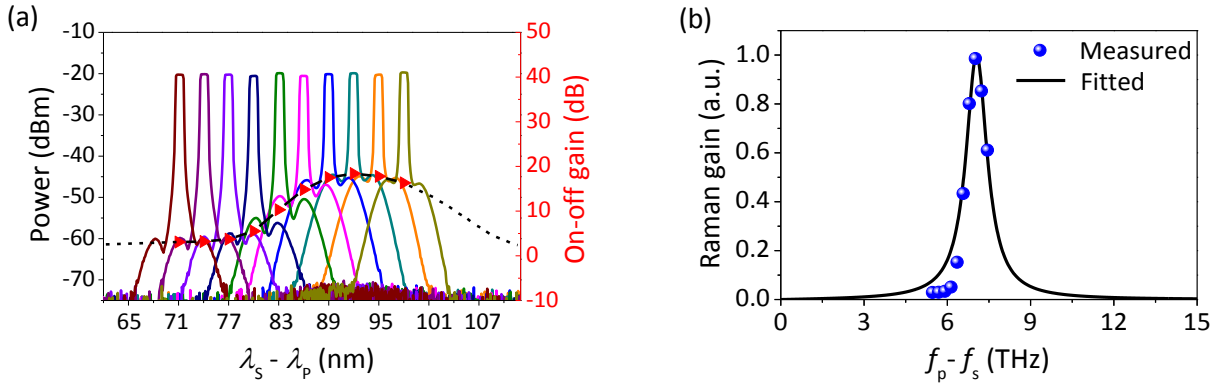

Fig. 3.4 (a) Measured Raman amplification spectra and extracted Raman gain as a function of probe wavelength λ_S shift with respect to pump wavelength $\lambda_P = 1.938\,\mu\text{m}$. The inferred Raman gain is presented by red triangles with right hand side vertical axis. (b) Normalized Raman gain as a function of frequency shift and fitted curve with a Lorentzian profile.

The linearity of the Raman gain is also investigated. Figure 3.6(a) shows the measured single-pass Raman gain as a function of probe power, whilst input peak power is kept at 3.0 W. The probe wavelength is set to $2.030\,\mu\text{m}$. As the coupled probe power is gradually increased up to 0.11 mW, no sign of gain saturation effect is observed. Figure 3.6(b) shows Raman gain as a function of coupled peak pump power, whilst probe power is kept at 0.021 mW at the wavelength of $2.030\,\mu\text{m}$. The Raman gain linearly increases as the peak pump power is increased without a sign of gain saturation.

Stimulated Raman scattering (SRS) can also be observed in the microwire without the probe signal. Figure 3.5 shows the SRS spectrum from the same microwire, pumped at a peak power of 3.1 W. SRS peak is located at $2.030\,\mu\text{m}$. If the pump power is further increased, second- and higher-order Raman scattering would arise from noise at multiple of Raman frequency shift. Cascaded Raman scattering was observed up to third-order in an $As_{38}Se_{62}$ suspended core fiber using a 1995 nm pump laser [74]. Up to eighth-order cascaded

Raman scattering was demonstrated in low loss AsS fiber pumped by a nanosecond source at 1545 nm [75]. Cascaded Raman scattering can be utilized in supercontinuum generation [76] and cascaded Raman fiber lasers [28].

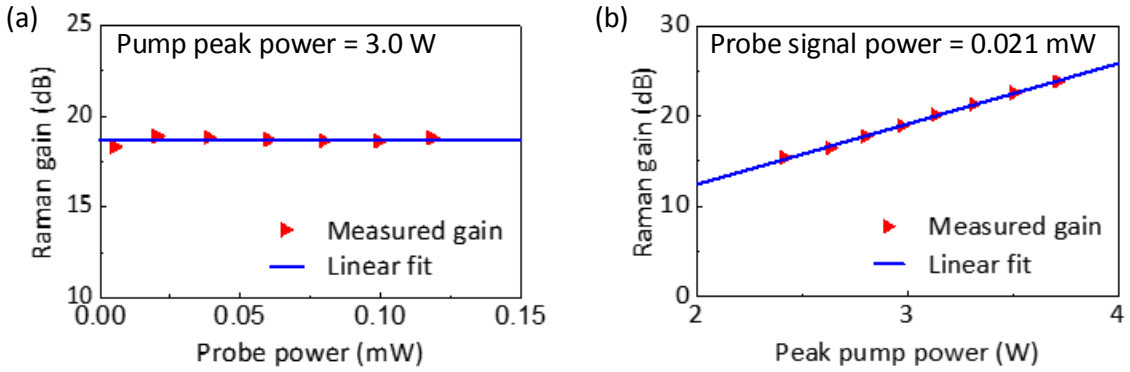

Fig. 3.5 (a) Measured Raman gain as a function of input probe power. (b) Measured Raman gain as a function of input peak pump power.

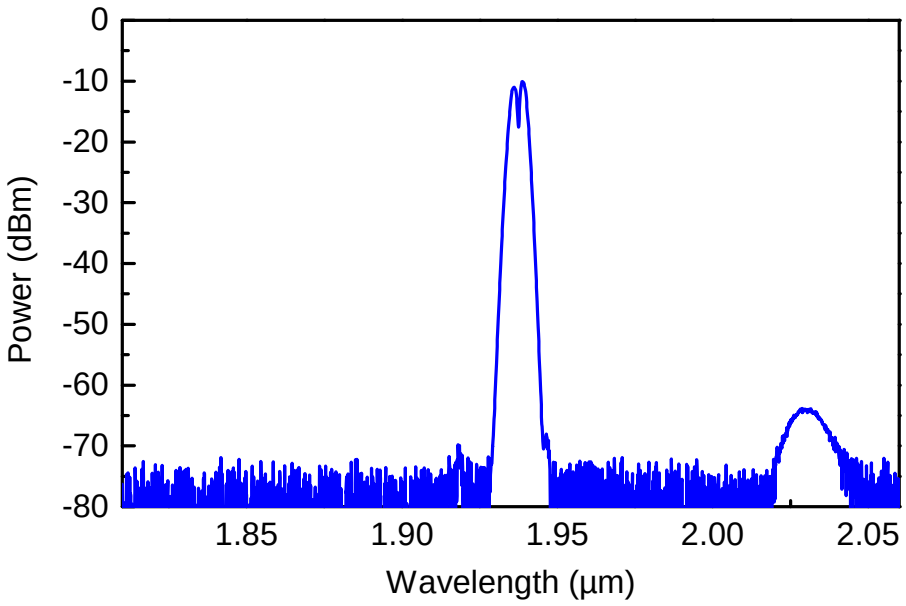

Fig. 3.6 Stimulated Raman scattering in the multimaterial microwire

3.5 Ring-cavity Raman fiber laser

Figure 3.7 shows a schematic of the Raman fiber laser. Amplified and filtered pump pulses are coupled into the Raman laser cavity through a WDM coupler. An 80/20 fiber coupler is used to extract 20% of the power at the output of the cavity. An optical delay line (ODL) serves to adjust the ring cavity length to the pump laser repetition rate. Another PC made of normal dispersion fiber is placed in the cavity to stabilize the polarization state of the laser as well as to compensate the total cavity dispersion. The total cavity dispersion is $\sim -0.05\,\mathrm{ps/nm}$ at the wavelength of $2.025\,\mu\mathrm{m}$, which is slightly normal dispersion. The total round-trip cavity loss is 12.0 dB, including 1.5 dB for the WDM coupler, 6.0 dB for the microwire, 2.0 dB for the 80/20 coupler plus insertion losses, 2.5 dB for the ODL. The round-trip cavity loss could be reduced to <5 dB by employing $2\,\mu\mathrm{m}$ fiber components and optimizing the microwire coupling losses.

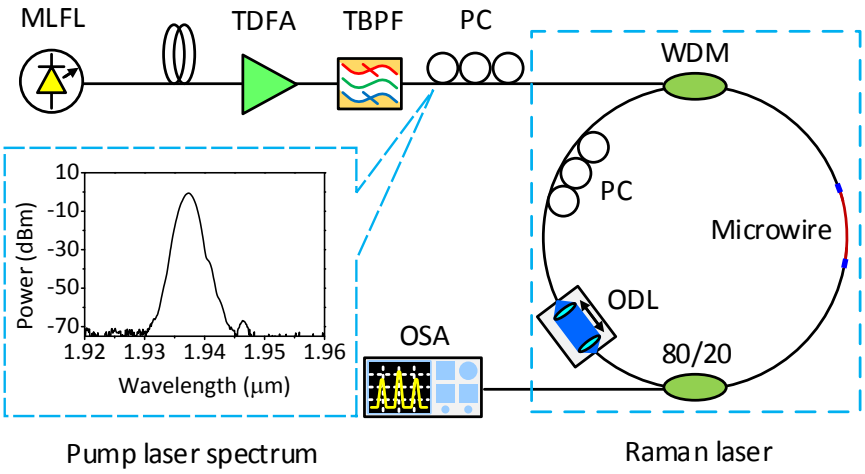

Fig. 3.7 Raman fiber laser experimental setup. MLFL, mode-locked fiber laser; TDFA, thulium-doped fiber amplifier; TBPF, tunable bandpass filter; WDM, wavelength division multiplexing coupler; PC, polarization controller; ODL, optical delay line; OSA, optical spectrum analyzer.

Laser oscillation is observed when the total Raman gain exceeds the total round-trip cavity loss and Raman pulses in the cavity are synchronized to the incoming pump pulses. Figure 3.8(a) shows the evolution of the laser output spectrum as the pump power is increased. The inset shows the average output power as a function of average pump power.

The laser threshold is reached at an average pump power of 1.69 mW, corresponding to a peak power of 6.6 W, with a slope efficiency of 4.5%. The slope efficiency could be further improved by a lower round-trip cavity loss and a higher output coupling ratio.

As the pump power is increased, the Raman laser bandwidth exceeds the Raman gain bandwidth of $As_{38}Se_{62}$, and shows flat-top spectral characteristics often seen in normal dispersion Raman fiber lasers [61]. The wide spectrum of the Raman laser possibly comes from two sources: one is that the spectrally broadened pump gives rise to broadened Raman gain bandwidth; the other source is the pump interacts with Raman signal via cross-phase modulation (XPM). Such a spectrally wide Raman laser output can potentially be externally compressed to femtosecond pulses.

The output wavelength of the Raman laser is tuned by adjusting the intra-cavity delay line, and as a result of time-dispersion tuning. The principle of the time-dispersion tuning technique is that different wavelength components of the Raman gain pulse, which is temproally stretched by the total cavity group velocity dispersion, can be tuned to synchronize with the incoming pump pulses after a round-trip in the cavity by slightly adjusting the cavity length. In fact, wavelength tuning can also be achieved by adjusting the pump pulse repetition rate. Thus, the time-dispersion tuning technique makes it easy to continuously tune the output wavelength of the Raman fiber laser. Neglecting any frequency-pulling effect due to the slope of Raman gain, the output wavelength tuning rate can be estimated by [77]

$$\frac{\Delta\lambda}{\Delta t} = \frac{c_0\lambda_s}{L_c D(\lambda)} \tag{3.3}$$

where c_0 is speed of light in vacuum, L_c is the total cavity length, $D(\lambda)$ is the net cavity dispersion at Stokes wavelength.

Figure 3.8(b) shows the output spectrum of the Raman laser at different cavity detuning values. The range of wavelength tunability is 8 nm, falling within the limits of Raman gain bandwidth.

3.6 Numerical simulations

To better understand the properties of the Raman fiber laser, numerical simulations are performed by solving the nonlinear Schrödinger equation (NLSE) given in equation 2.22 using the split-step Fourier method [2]. The Raman response function derived above is incorporated in the NLSE for the multimaterial fiber and the microwire, while Raman scattering in silica fibers is ignored due to low peak power levels involved. Dispersion terms of α and γ are

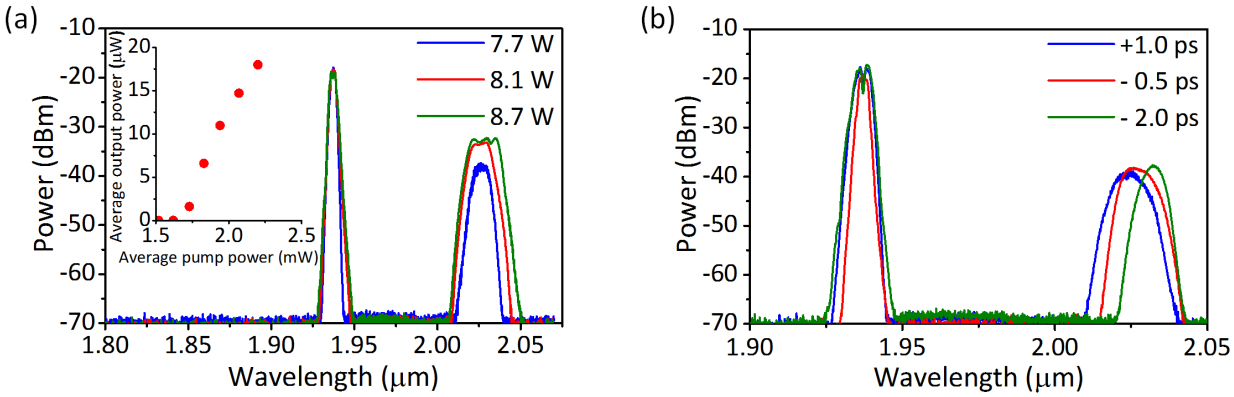

Fig. 3.8 (a) Output spectrum of the Raman laser with increasing pump power. Inset: Average output power versus average pump power. (b) Raman laser output spectrum at different relative cavity detuning.

also neglected, given the relatively narrow range of wavelengths in the simulation. Figure 3.9 shows the schematic of the simulation architecture. The circulating optical field containing both Raman signal and residual pump is filtered by the WDM coupler at the end of each round-trip. The spectral response of the WDM coupler is modeled from experimental data. The Raman signal is delayed by 6.2 ps for synchronization before it is combined with a new pump pulse and fed back into the next round-trip. Raman pulse energy and pulse width are monitored as a function of the number of round-trips to ensure the numerical solution converges to a consistent solution.

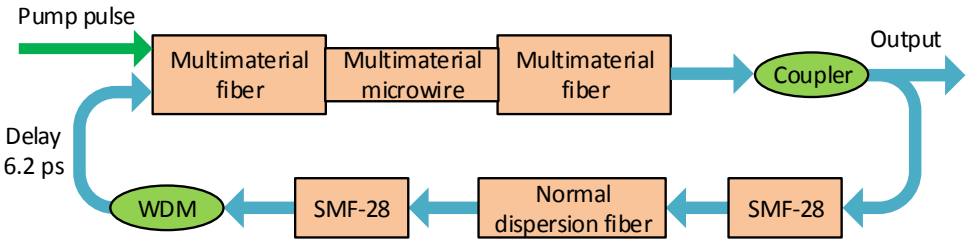

Fig. 3.9 Simulation diagram of the Raman fiber laser.

Table 3.1 shows the simulation parameters selected for the Raman laser. Figure 3.10 shows the spectral and temporal evolution of the Raman fiber laser output as increased number of round-trips for a peak pump power of 8.1 W. Raman oscillation self-starts and reaches steady-state after ∼20 round-trips into which only the pump pulses are injected into

the resonant cavity. Pump spectral broadening due to XPM with the Raman pulse can also be observed from the spectral evolution. Figure 3.11(a) shows output spectra of the Raman fiber laser as a function of pump power, in good agreement with experimental results. As the peak pump power is increased, the Raman signal spectrum gradually develops a flat-top structure. Wavelength tunability is also confirmed by changing the temporal delay. Figure 3.11(b) shows output Raman pulses obtained by filtering and inverse Fourier transformation. Inspection of the phase content of the pulses reveals a strong linear chirp that can be compressed by applying a linear dispersion. Figure 3.11(c) shows the Raman pulses after recompression. As the peak pump power is increased, the compressed Raman pulse width decreases. However, due to the increased nonlinear chirp in the Raman pulses, compressed pulses exhibit increasingly prominent pedestals. Figure 3.11(d) shows the amount of dispersion required for optimal compression and compressed pulse width as a function of peak pump power. In light of the simulations, output Raman pulses could be compressed to femtosecond pulses by propagating through e.g. a few meters of fiber with anomalous dispersion.

Table 3.1 Raman fiber laser simulation parameters

Parameters [unit]	Multimaterial Fiber	Multimaterial Microwire	SMF-28	Normal Dispersion Fiber
Length [m]	0.03	0.1	3.15	3.31
α [dB/m]	10	20	0.02	0.03
α_2 [cm/GW]	0.011	0.011	0	0
β_2 [ps^2/m]	0.774	1.67	–0.068	0.038
β_3 [ps^3/m]	1.0×10^{-3}	-3.3×10^{-3}	-3.4×10^{-4}	2.6×10^{-4}
β_4 [ps^4/m]	7.44×10^{-7}	1.79×10^{-5}	-1.76×10^{-6}	-3.06×10^{-6}
γ [W^{-1}m^{-1}]	0.5	18	0.001	0.0025
τ_1 [fs]	22.5	22.5	–	–
τ_2 [fs]	342	342	–	–
f_R [a.u.]	0.1	0.1	–	–

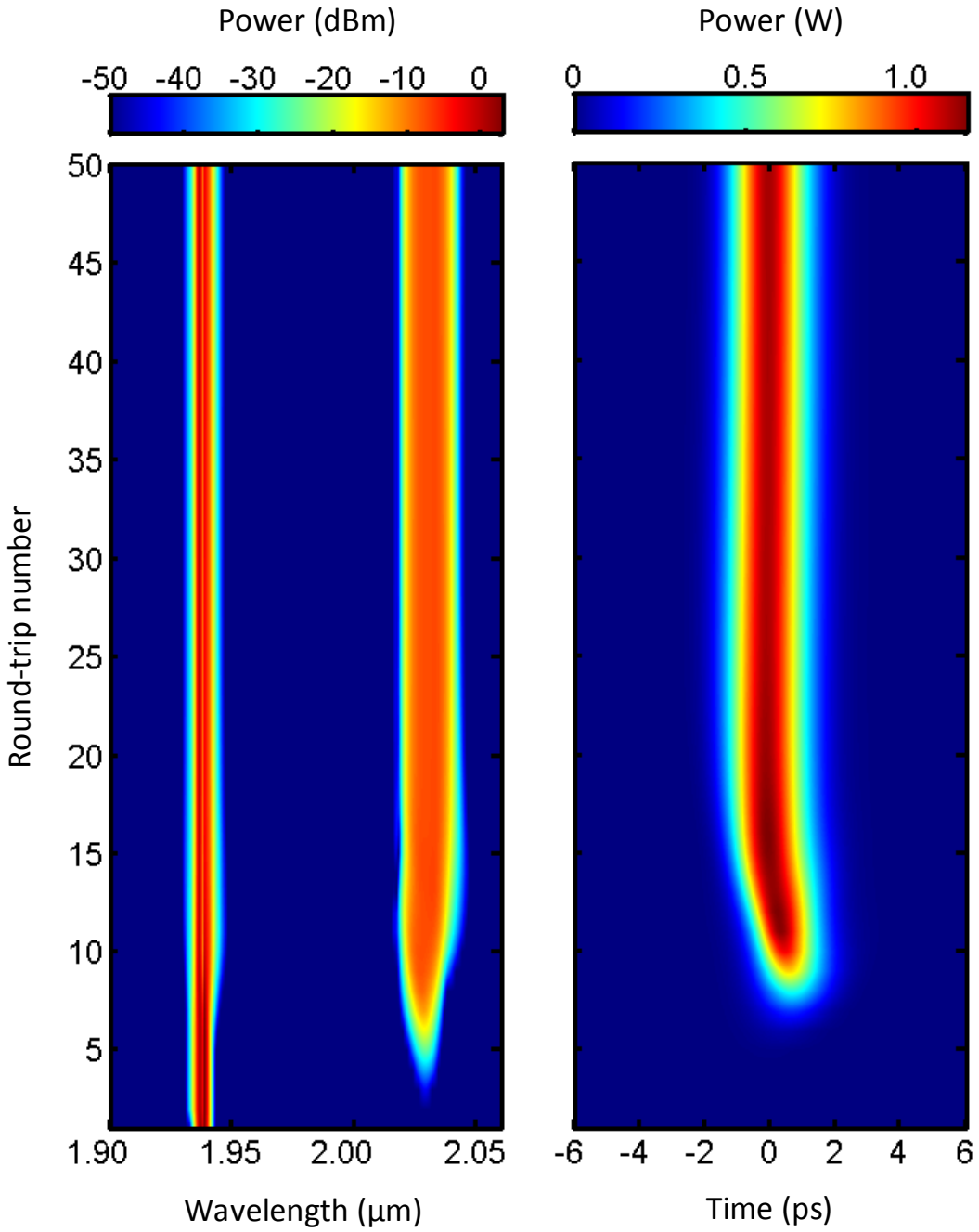

Fig. 3.10 Spectral and temporal evolution of the Raman fiber laser output.

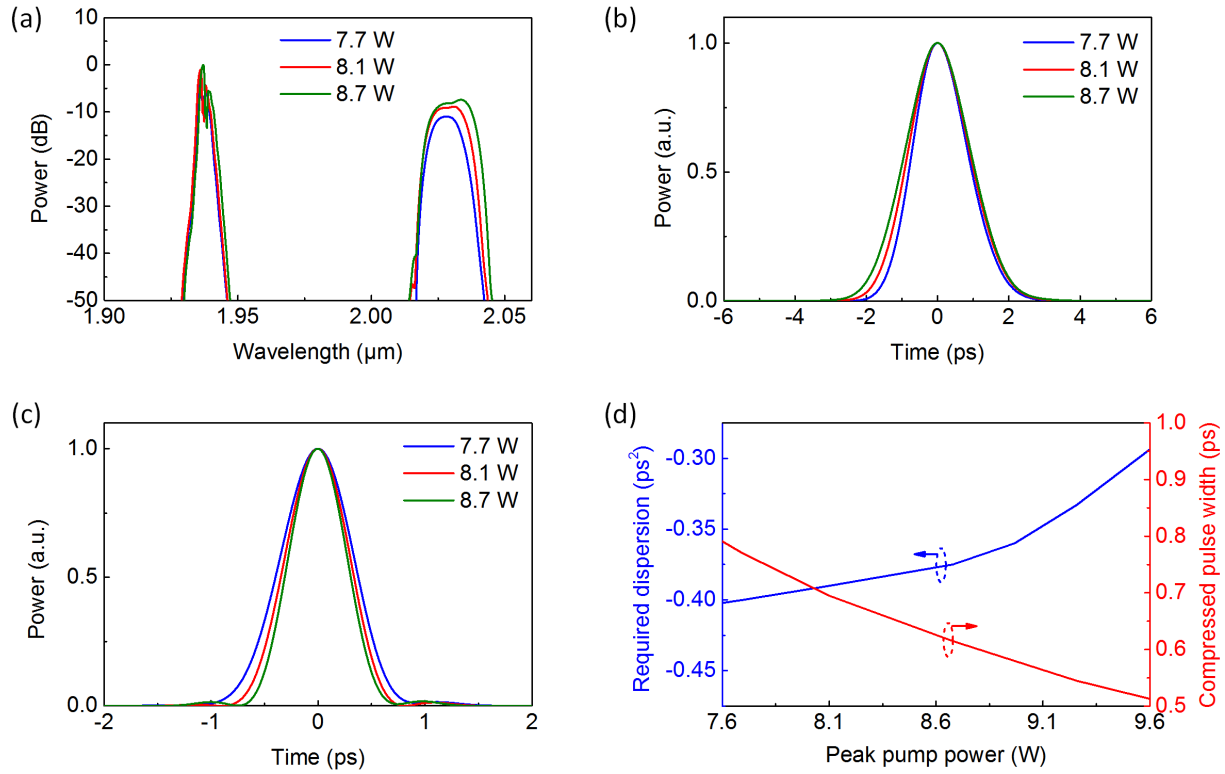

Fig. 3.11 (a) Simulated output spectra of the Raman fiber laser. (b) Simulated temporal shape of output Raman pulses and (c) after compression. (d) Required dispersion for optimal pulse compression and compressed pulse width as a function of peak pump power.

3.7 Summary

In summary, we have demonstrated the operation of a Raman fiber laser based on a multimaterial chalcogenide microwire. The Raman laser emits at 2.025 μm from pump pulses centered at a wavelength of 1.938 μm. The threshold peak pump power of the Raman laser is 6.6 W, with a slope efficiency of 4.5%, which could be further improved by reducing the round-trip cavity loss and optimizing the output coupling ratio. The reach of laser output wavelength could be significantly extended towards longer wavelengths by enabling the operation of second or higher order Raman shift [78]. Numerical simulation results are in good agreement with experimental observations, providing important insight into output Raman pulse evolution. Output Raman pulses can be compressed to femtosecond pulses by applying linear dispersion. The transmission window of the microwire is only limited by the trans-

mission windows of $As_{38}Se_{62}$ and $As_{38}S_{62}$, which spans over 1.5–11.0 μm wavelength range. This microwire is thus a promising gain medium for the fabrication of mid-infrared sources that are compact and operate with low-power consumption.

Chapter 4

Parametric amplification and oscillation in chalcogenide microwires

[1]In this chapter, we report the first chalcogenide-based optical parametric oscillator (OPO) relying on pure parametric gain. The all-fiber OPO operates in the wavelength range of 2 μm and is tunable over 290 nm from the combined Stokes and anti-Stokes contributions. The gain medium is a 10 cm long chalcogenide microwire made out of a high modal confinement As_2Se_3 core with Cyclo Olefin polymer (COP) cladding, leading to optimized chromatic dispersion, high nonlinearity, and broadband transparency. With a power threshold of only a fraction of a milliwatt, this design is promising for the fabrication of tunable, compact, and low-power consumption mid-infrared sources.

4.1 Introduction

Optical parametric oscillators are the most efficient and flexible sources to access broadband or unconventional wavelength bands [79]. Confined within an optical fiber path, fiber optical parametric oscillators (FOPOs) provide the additional advantages of compactness, mechanical stability, reliability of operation, beam quality, and easy integration with fiber systems [80]. A number of FOPOs designs have been proposed that together cover the transparency range of silica glass. While wavelengths at 2 μm and above are important for chemical sensing applications, FOPOs designed for these wavelengths are limited by the relatively large attenuation and low nonlinearity of silica. In 2010, Gershikov et al. have demonstrated the operation of a FOPO at a wavelength of 2 μm. The FOPO was enabled

[1]Part of the content in this chapter has been subject to publication in (1) N. Abdukerim, L. Li and M. Rochette, Chalcogenide-based optical parametric oscillator at 2 μm, Optics Letters 41(18), 4364-4367 (2016).

by a 200 m long highly nonlinear silica fiber, leading to propagation losses of 15 dB, and required 30 W of pump power to reach the oscillation threshold [81].

As an alternative to silica fibers, chalcogenide microwires provide excellent mid-IR transmission and enhanced nonlinearity [19,50]. By an appropriate design of the chromatic dispersion properties, chalcogenide microwires can yield significant parametric gain spanning over a broad spectral range [82]. Ahmad et al. reported the first Raman-assisted FOPO based on chalcogenide glass, using an As_2Se_3 microwire to generate parametric oscillation at output wavelengths of 1.605 μm (Stokes) and 1.502 μm (anti-Stokes) [21]. However, wavelength tunability was limited to the Raman gain bandwidth of only a few nanometers.

In this chapter, we demonstrate the first chalcogenide-based FOPO that oscillates from pure parametric gain. The broad oscillation spectrum of the FOPO is divided into two sections: a first set of wavelengths for which the gain originates from pure parametric process, and a second set of wavelengths for which the gain is a combination of parametric and Raman processes. The FOPO is tunable from 1.980 μm to 2.142 μm (Stokes) and from 1.770 μm to 1.898 μm (anti-Stokes). The average power threshold of the FOPO is 487 μW with a slope efficiency of 2%.

4.2 Theoretical background

As chalcogenide glasses are third order nonlinear media, parametric process happens as four-wave mixing (FWM) and third-harmonic generation (THG). FWM can be classified as degenerate FWM and non-degenerate FWM, depending on the number of waves involved in the parametric process. When pump and signal wavelengths satisfy the phase-matching condition of degenerate FWM, parametric gain becomes available in fibers. The effective phase mismatch is given by [2]

$$\kappa = 2\gamma P_p + \Delta\beta, \tag{4.1}$$

where γ is waveguide nonlinear parameter, P_p is the peak pump power, and $\Delta\beta$ is the linear phase-mismatch parameter between pump and signal wavelengths, which is governed by the dispersion profile of the waveguide

$$\Delta\beta = \sum_{m=2}^{M} \frac{2\beta_m}{m!}\Omega^m \qquad (m = 2, 4, 6, ..., M), \tag{4.2}$$

where β_m is m-th order dispersion coefficient, given by equation 2.14, and Ω is the angular frequency difference between pump and Stokes or anti-Stokes signal. M is the order which

dispersion effects are included. The parametric gain coefficient is given by

$$g = \sqrt{(\gamma P_p)^2 - (\kappa/2)^2}, \tag{4.3}$$

and the parametric gain is

$$G = 1 + (\gamma P_p)^2 \sinh^2(g L_{eff}), \tag{4.4}$$

where L_{eff} is the effective length of the nonlinear medium. Effect of pump depletion is neglected. In order to achieve parametric gain, the linear phase-mismatch parameter $\Delta\beta$ must be within the range $0 < \Delta\beta < 4\gamma P_p$. Peak parametric gain occurs at an angular frequency shift at which $\kappa = 0$.

Assuming all pump, signal, and idler waves experience same attenuation coefficient α and nonlinearity coefficient γ, propagation of pump A_p, signal A_s, and idler A_i is governed by the coupled amplitude equation

$$\begin{aligned}
\frac{\mathrm{d}A_p}{\mathrm{d}z} &= i\gamma(|A_p|^2 + 2|A_s|^2 + 2|A_i|^2)A_p + 2i\gamma A_p^* A_s A_i \exp(i\Delta\beta z) - \frac{\alpha}{2}A_p, \\
\frac{\mathrm{d}A_s}{\mathrm{d}z} &= i\gamma(2|A_p|^2 + |A_s|^2 + 2|A_i|^2)A_s + i\gamma A_p^2 A_i^* \exp(-i\Delta\beta z) - \frac{\alpha}{2}A_s, \\
\frac{\mathrm{d}A_i}{\mathrm{d}z} &= i\gamma(2|A_p|^2 + 2|A_s|^2 + |A_i|^2)A_i + i\gamma A_p^2 A_s^* \exp(-i\Delta\beta z) - \frac{\alpha}{2}A_i.
\end{aligned} \tag{4.5}$$

By ignoring pump depletion and cross-phase modulation (XPM), the equation for the pump A_p can be readily integrated to $A_p = \sqrt{P_p}\exp((i\gamma P_p - \alpha/2)z)$, which then can be plugged into the equations for signal and idler waves to get

$$\mathbf{A}z = \begin{bmatrix} i\kappa/2 & i\gamma P_p \\ -i\gamma P_p & -i\kappa/2 \end{bmatrix} \mathbf{A}, \tag{4.6}$$

where $\mathbf{A}$ is a column vector with elements A_s and A_i. Then we can obtain a propagation matrix $\mathbf{M}$ to describe the parametric gain evolution along the length of the fiber [83]

$$\mathbf{A}(z) = \mathbf{M}\mathbf{A}(0) = \begin{bmatrix} \cosh(gz) + \frac{i\kappa}{2g}\sinh(gz) & \frac{i\gamma P_0}{\alpha}\sinh(gz) \\ -\frac{i\gamma P_0}{g}\sinh(gz) & \cosh(gz) - \frac{i\kappa}{2g}\sinh(gz) \end{bmatrix}. \tag{4.7}$$

4.3 Microwire design and fabrication

The microwire used in this investition is fabricated from a three-layer composite that consists of an inner core of As_2Se_3, and intermediate layer of Cyclo Olefin polymer (COP), and an outer layer of poly-methyl methacrylate (PMMA). Figure 4.1 shows the microwire geometry and composition of the hybrid fiber. The large refractive index contrast between the core of As_2Se_3 ($n_{\mathrm{AsSe}} = 2.81$) and cladding of COP ($n_{\mathrm{cop}} = 1.48$) tightly confines the optical mode in the microwire core and enables precise chromatic dispersion engineering. The COP cladding preserves transparency in the $2\,\mu$m wavelength band, and ensures optical insulation of the evanescent wave from the ambient environment, while the outer PMMA layer provides the mechanical robustness required for practical handling of the waveguide. Figure 4.2(a) and (b) show the second order (β_2) and fourth order (β_4) dispersion coefficients as a function of microwire core diameter and operation wavelength. The group-velocity dispersion β_2 of the fundamental mode propagating in the microwire can be engineered to zero, normal or anomalous, depending on the target application [84]. The combination of β_2 and β_4 (ignoring higher order dispersion coefficients) determines the linear phase-mismatch for FWM process.

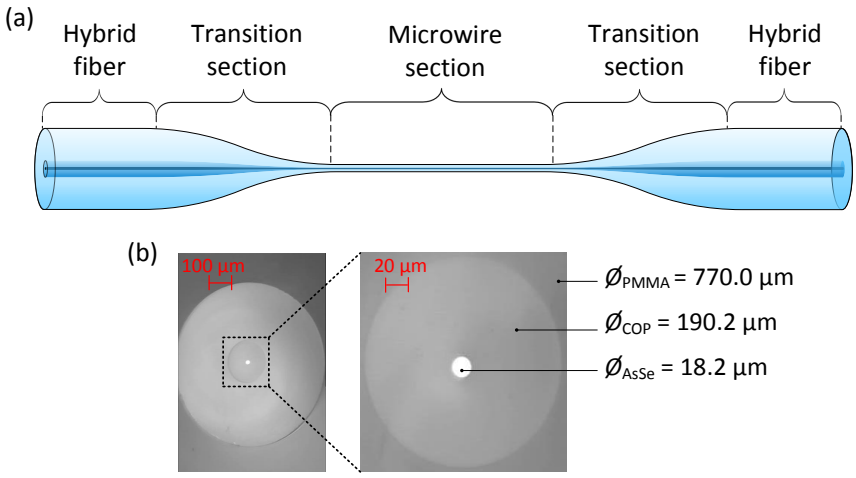

Fig. 4.1 (a) Hybrid microwire composition and geometry (not to scale). (b) Reflection optical micrograph of the hybrid fiber facet.

Parametric gain is present when the pump and signal wavelengths satisfy the phase-matching condition of degenerate FWM [2]. Figure 4.3 shows the parametric gain expected in a 10 cm long microwire with a peak pump power of 2.4 W, using the propagation matrix method [83]. The wavelength at which the Raman gain maximum occurs ($2.025\,\mu$m) is indicated by a horizontal dashed line [26]. A microwire with a core diameter of $\sim 1.55\,\mu$m has a Raman gain maximum that superimposes at the same wavelength as the parametric

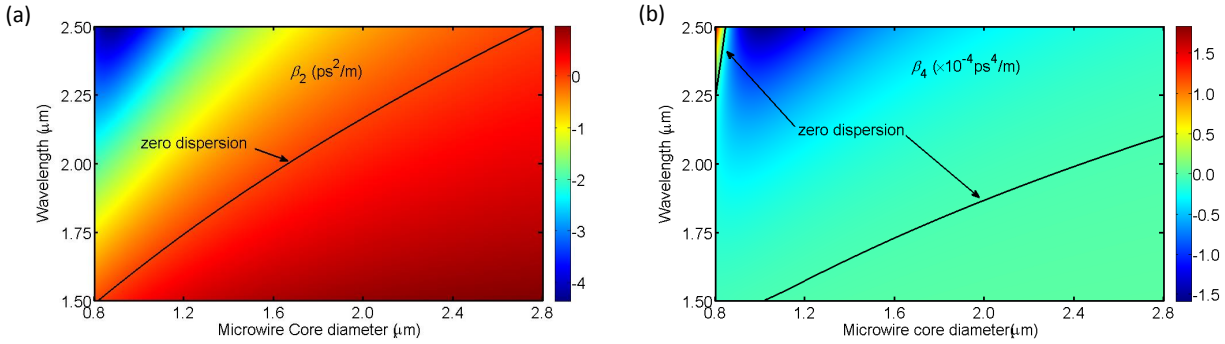

Fig. 4.2 (a) Group velocity dispersion β_2 for the fundamental mode of the microwire as a function of core diameter. Zero dispersion wavelength with corresponding microwire core diameter is illustrated by the solid line. (b) Fourth order dispersion β_4 for the fundamental mode of the microwire as a function of core diameter.

gain maximum. Raman gain and parametric gain can be combined to significantly enhance the amplification gain bandwidth [85]. A narrow band parametric gain is achieved at a core diameter in excess of 1.6 μm, where β_2 is positive and β_4 is negative [86].

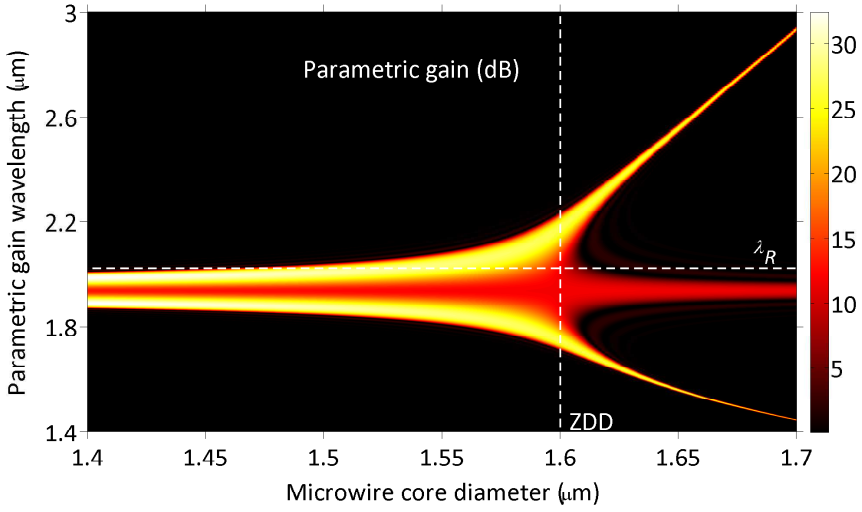

Fig. 4.3 Parametric gain spectrum of a 10 cm long microwire as a function of core diameter. The peak pump power is 2.4 W at a wavelength of 1.938 μm. Dashed lines indicate the positions of zero dispersion diameter (ZDD) and maximum Raman gain wavelength (λ_R).

The actual core diameter of any fiber is known to have random variations related to fabrication, which results in randomly varying parametric gain profile along the length of the fiber due to variation in phase-matching condition [87, 88]. In the process of microwire fabrication using the heat-brush method, nanoscale fluctuation occurs inevitably in core

diameter along the length of the microwire. Chow et al. used a phase-correlation Brillouin distributed measurement method to map the core diameter of a 13 cm long PMMA-cladded As_2Se_3 microwire with a designed diameter of 1.65 μm, and found the diameter fluctuation to be less than 50 nm [89]. However small the fluctuation is, it affects the parametric gain profile of the chalcogenide microwire. Every fabricated microwire has different diameter non-uniformity, resulting in different parametric gain profile from one microwire to another, though designed with the exact same diameter. Figure 4.4 shows the calculated parametric gain spectra for 100 realizations from microwires designed with core diameters of 1.47 μm, 1.55 μm, 1.6 μm, 1.625 μm and 1.65 μm, respectively. For microwires designed with strong anomalous dispersion, such as 1.47 μm and 1.55 μm core diameters, dispersion fluctuation has little impact on the parametric gain spectra. However, when the microwire is designed with zero dispersion (core diameter of 1.6 μm) or normal dispersion (core diameters of 1.625 μm and 1.65 μm), dispersion fluctuation severely distorts the actual parametric gain spectra. The MATLAB code used to simulate the effect of dispersion fluctuation on the parametric gain profile is provided in appendix A.1.

The microwire used in this investigation was designed with a core diameter of 1.47 μm, combined with high optical confinement factor and high nonlinear refractive index of As_2Se_3 ($n_2 = 7.6\times10^{-18}$ m^2/W at 1.94 μm [39]) leading to a high waveguide nonlinearity of γ=24 W^{-1}m^{-1}, and a zero dispersion wavelength of λ_{ZD}=1.875 μm. The lengths of the microwire and transition sections are 10 cm and 2 cm, respectively. Both ends of the hybrid fiber are polished and butt-coupled to SMF-28 via UV-cured epoxy and result in a SMF to SMF insertion loss of 8 dB, including 0.25 dB/cm of propagation loss at 2 μm in the microwire due to COP absorption and diameter non-uniformities, and the rest is attributed to Fresnel reflection chalcogenide-silica interfaces, mode-mismatch and misalignment losses.

4.4 Parametric amplification in chalcogenide microwire

In this experiment, the single-pass parametric gain is measured with a pump-probe configuration. Figure 4.5 shows the experimental setup used to measure parametric gain in the microwire. Pump pulses with a full-width at half-maximum (FWHM) duration of 800 fs are provided by a 30 MHz thulium-doped mode-locked fiber laser with a central wavelength of 1.938 μm. The pulses are amplified by a thulium-doped fiber amplifier and subsequently filtered by a 2 nm FWHM tunable bandpass filter to lengthen the pulses duration to ~3 ps FWHM, as well as to eliminate amplified spontaneous emission noise from the fiber amplifier. A wavelength-tunable thulium fiber laser was constructed following [73], as shown in Figure

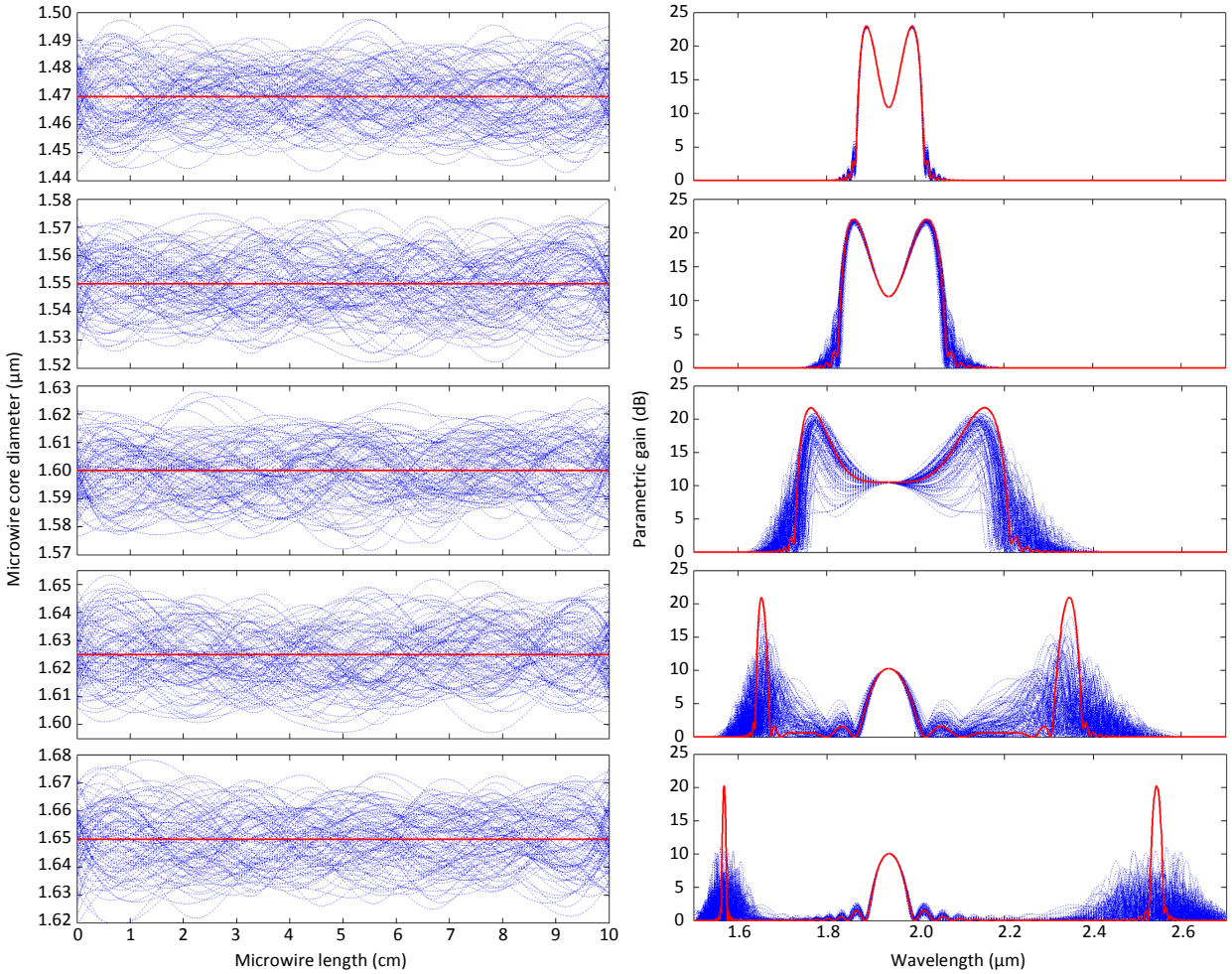

Fig. 4.4 Microwire-to-microwire variations in the parametric gain profile caused by random diameter fluctuation along the length of the microwire. (Red curves denote ideal diameter and ideal parametric gain spectrum.)

3.3, and serves as a continuous wave probe signal. Pump and probe are coupled into the microwire via an 80/20 silica fiber coupler. The polarization states of pump and probe are co-aligned using polarization controllers. The parametric gain of the probe is measured as a function of the probe wavelength from 1.955 μm to 2.040 μm. The average pump power coupled into the microwire is 0.23 mW, corresponding to a peak power of 2.4 W, while the input probe power is kept at 0.025 mW. Figure 4.6(a) shows the output spectra recorded on an optical spectrum analyzer. The amplified signals and generated idlers are pulsed as a consequence of the pulsed pump. Parametric signal gain and idler conversion gain values for each probe signal wavelength were extracted by integrating amplified signal sidebands and idler spectra, and calculating the ratio between amplified signal/idler peak power and probe

signal average power [90]. Figure 4.6(b) shows the signal and idler gain as a function of wavelength. The microwire provides an optical gain resulting from the superimposition of a broad parametric gain and Raman gain. A maximum gain of 15.5 dB occurs at a wavelength of 2.025 μm, corresponding to the Raman frequency shift in As_2Se_3, that is $\Delta f \sim$6.7 THz or $\Delta\lambda \sim$87 nm with respect to the pump wavelength. The measured parametric gain is lower than the theoretical value by up to 9 dB as a result of random diameter fluctuations and thus longitudinal dispersion fluctuation along the length of the microwire [89, 91].

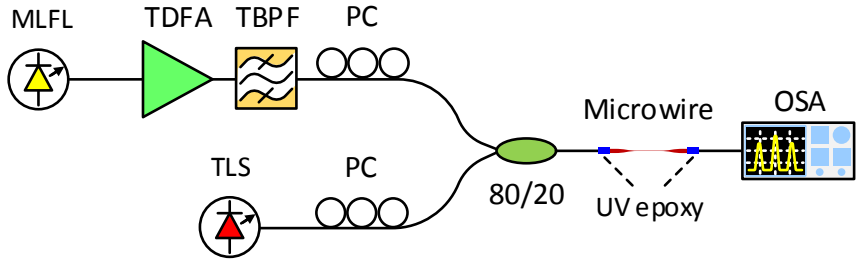

Fig. 4.5 Experimental setup for measurement of parametric gain in the chalcogenide mcirowire.

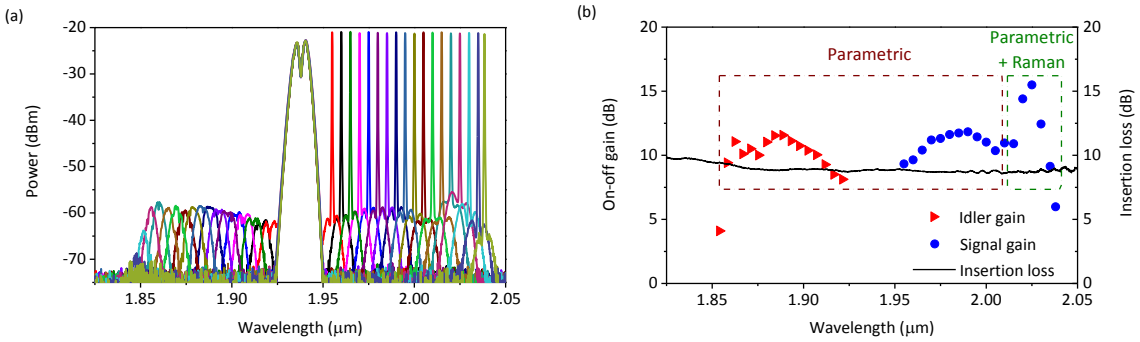

Fig. 4.6 (a) Superimposition of single-pass parametric amplification spectra resulting from several probe wavelengths. (b) On-off parametric signal gain (blue circles), idler conversion gain (red triangles), and insertion loss of the pigtailed microwire (black solid line).

Spontaneous FWM can be observed in the microwire without the probe signal. Figure 4.7(a) shows the spontaneous FWM spectrum from the same microwire, pumped at a peak

power of 4.6 W. FWM peak is located at 1.983 μm, corresponding to a frequency shift of 3.5 THz, about half of the Raman frequency shift, which is located at 2.016 μm. With a probe signal centered at the FWM peak wavelength, cascaded FWM is observed. Figure 4.7(b) shows the cascaded FWM spectrum, at two different pump power levels, with up to fifth-order anti-Stokes signal generated on the shorter wavelength side, and up to third-order Stokes signal generated on the longer wavelength side. Higher order cascaded Stokes signal is limited by the COP cladding absorption at longer wavelengths.

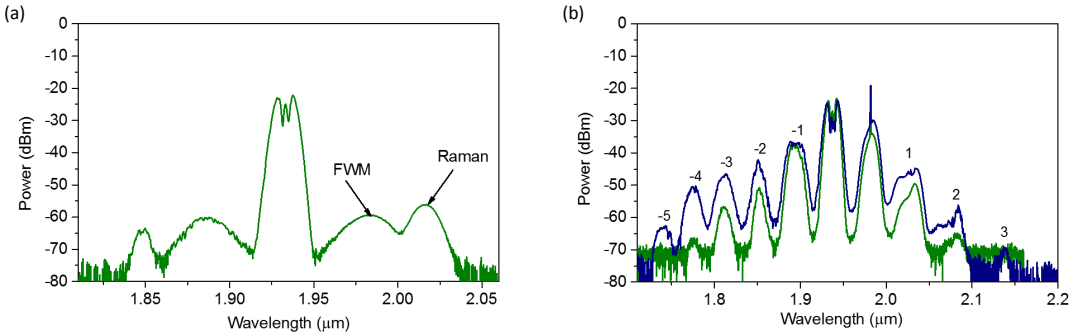

Fig. 4.7 (a) Spontaneous FWM from the microwire. (b) Cascaded FWM at two different peak pump power levels of 4.6 W (green) and 6.4 W (blue).

4.5 Ring-cavity fiber optical parametric oscillator

Figure 4.8 presents the FOPO as a result of inserting the gain medium in a resonant cavity. The FOPO comprises a wavelength division multiplexing (WDM) coupler to combine the pump pulses in the cavity and extract them after one round-trip, a tunable optical delay line (ODL) to precisely adjust the cavity length according to the repetition rate of the pump laser, a polarization controller (PC), and a 80/20 broadband fiber coupler to sample the in-cavity power. The PC comprises a 3.4 m long high numerical aperture and normal dispersion fiber to compensate the total cavity dispersion. All the components at the exception of the microwire and PC are made with SMF-28 fiber, which has anomalous dispersion at 2 μm. At the output coupler, 80% of the signal is fed back to the cavity, and 20% serves to monitor the signal.

The FOPO reaches the oscillation threshold when the total nonlinear gain exceeds the total round-trip loss of 14 dB, and when the cavity length enables the synchronization of pump and oscillating pulses. Figure 4.9(a) shows the average output power as a function of average pump power for the FOPO output at a wavelength of 2.023 μm. The threshold

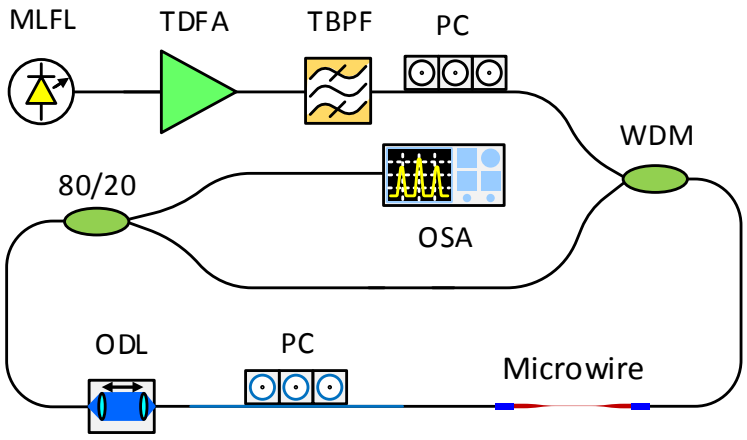

Fig. 4.8 Experimental setup of the FOPO. MLFL, mode-locked fiber laser; TDFA, thulium-doped fiber amplifier; TBPF, tunable bandpass filter; WDM, wavelength division multiplexing coupler; PC, polarization controller; ODL, optical delay line; OSA, optical spectrum analyzer.

pump power is 0.485 mW, corresponding to 5 W of peak power, with a slope efficiency of 2%. The inset shows the evolution of FOPO output signal optical spectrum as the average pump power increases.

The FOPO is wavelength-tuned by adjusting the cavity length via the optical delay line, with a rate of ∼10 nm/ps, based on the time-dispersion tuning technique described in section 3.5. The wavelength tuning rate is determined by the totoal cavity group velocity dispersion and the output signal wavelength. Figure 4.9(b) shows spectra of the FOPO at several wavelengths. On the long wavelength side (Stokes), the FOPO wavelength is continuously tuned from 1.980 μm to 2.035 μm, corresponding a total tuning range of 55 nm. This wavelength span exceeds the Raman gain bandwidth and thus the FOPO oscillation is maintained solely by parametric gain in the wavelength range of 1.980 μm to ∼2.005 μm. The peak pump power requires up to 8 W to access the complete tuning range. On the short wavelength side (ant-Stokes), the FOPO wavelength is continuously tuned from 1.850 μm to 1.898 μm, corresponding to a total tuning range of 48 nm. The shortest walk-off length in between pump pulses and oscillating signal pulses in the microwire is ∼18 cm. This is almost twice as long as the microwire and thus temporal walk-off is not expected to limit the wavelength tunable range of the FOPO. The wavelength tunable range is mainly limited by the parametric gain bandwidth of the microwire and transmission bandwidth of the WDM

coupler used in the experiment, as shown by the black curve in figure 4.9(b).

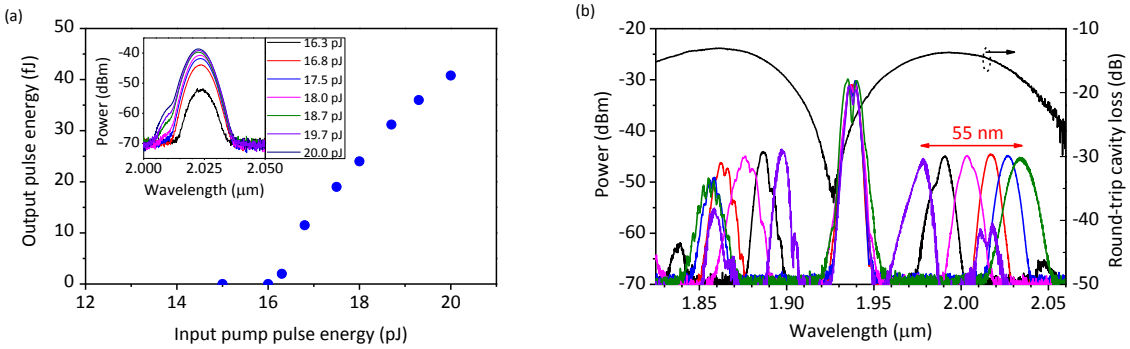

Fig. 4.9 (a) Average output signal pulse energy versus average input pump pulse energy. Inset: output signal spectrum evolution with increasing average input pump pulse energy. (b) Output spectra of the FOPO for various delay settings. Black curve shows the FOPO round-trip cavity loss.

The FOPO also shows evidence of cascaded parametric oscillation, as noticed from Figure 4.9(b). Figure 4.10 shows two FOPO outputs for two positions of the optical delay line. The first orders of the FOPO can be tuned from 1.980 μm to 2.035 μm (Stokes) and 1.850 μm to 1.898 μm (anti-Stokes) whereas the second orders can be tuned from 2.024 μm to 2.142 μm (Stokes) and 1.770 μm to 1.859 μm (ant-Stokes). In total, the FOPO is thus tunable over a spectral range of 290 nm.

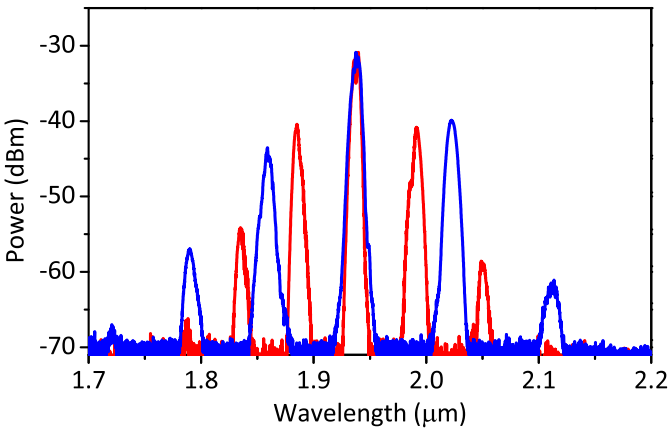

Fig. 4.10 Output spectra of the FOPO showing first and second order parametric oscillation. Delay line adjusted for first order Stokes set at 2.023 μm (blue) and 1.991 μm (red).

4.6 Summary

In conclusion, we have demonstrated the first 2 μm band FOPO using a highly nonlinear chalcogenide microwire. The parametric gain of the FOPO is sufficiently strong to support oscillation without the support of Raman gain. The fiber optical parametric oscillator (FOPO) has a low peak pump power threshold of 5 W, and a slope efficiency of 2%. The first-order oscillating signal can be tuned from 1.980 μm to 2.035 μm on the Stokes side and from 1.850 μm to 1.898 μm on the anti-Stokes side. With the help of cascaded FWM, the FOPO can cover a total tunable wavelength range of 290 nm. The FOPO has lower threshold and higher slope efficiency comparing to previously reported FOPOs in the same wavelength band [81, 92], thanks to high nonlinearity and low loss in the chalcogenide microwire. However, the round-trip cavity loss is relatively high, because the fiber components are not specially designed for 2 μm wavelength band. Therefore, threshold pump power and slope efficiency are expected to improve further, by using low-loss fiber components and reducing the microwire insertion loss.

Chapter 5

Pulse characterization based on four-wave mixing in chalcogenide microwires

[1]In this chapter, we report the first all-fiber frequency-resolved optical gating (FROG) device from nonlinear processing in chalcogenide glass. The strong four-wave mixing efficiency of an 11 cm long chalcogenide microwire enables a high sensitivity characterization of pulses in the 2 μm wavelength band. The amplitude and phase of chirped and unchirped picosecond pulses are accurately characterized with a high sensitivity of 0.16 mW^2. This represents more than six orders of magnitude improvement in measurement sensitivity comparing to conventional FROG techniques based on second-harmonic generation.

5.1 Introduction

Frequency-resolved optical gating (FROG) has been widely employed for complete pulse characterization in amplitude and phase. The conventional FROG technique relies on free-space based second-harmonic generation in a bulk $\chi^{(2)}$ crystal [93]. The measurement sensitivity of this approach is limited to pulse energies of the order of the pico to nanjoule due to a short interaction length in the crystal, with a sensitivity in the order of $10^6\,\mathrm{mW}^2$, as defined by the product of peak and average powers [93, 94], which represents the minimum input power level required for accurate pulse characterization. While impressive levels of measure-

[1]Part of the content in this chapter has been subject to publication in (1) N. Abdukerim, Imtiaz Alamgir and M. Rochette, All-fiber frequency-resolved optical gating pulse characterization from chalcogenide glass, Optics Letters 43(14), 3228–3231 (2018).

ment sensitivity as low as $2.0\times10^{-6}\,\mathrm{mW}^2$ have been demonstrated from FROGs based on $\chi^{(2)}$ nonlinearity in aperiodically poled lithium niobate waveguides [95, 96], $\chi^{(3)}$ nonlinearities in fibers and waveguides have been successfully used for FROG pulse characterization in the $1.55\,\mu$m wavelength band with significant improvement in sensitivity [97–103], among which an approach based on four-wave mixing (FWM) in highly nonlinear silica fiber [97] demonstrated a measurement sensitivity as low as $0.2\,\mathrm{mW}^2$. Unfortunately, sensitivity and resolution of conventional FROGs decrease as the input wavelength increases. This has posed challenges for complete pulse characterization at wavelengths of $2\,\mu$m and beyond. So far, no fiber or waveguide-based FROG has been demonstrated at longer wavelengths than $1.55\,\mu$m towards the mid-IR.

Chalcogenide glasses (e.g. As_2Se_3, As_2S_3) possess good transparency in the mid-IR up to $15\,\mu$m with intrinsically high nonlinearity [44]. With appropriate design, chalcogenide microwires yield highly efficient parametric conversion that spans over hundreds of nm [82]. Parametric wavelength conversion and oscillation have been demonstrated in chalcogenide microwires in various dispersion regimes [18, 21, 22, 82, 86, 104]. The parametric gain from chalcogenide microwires can be used to enable highly sensitive pulse characterization techniques with great flexibility in operating wavelength.

In this chapter, we demonstrate the first all-fiber FROG device enabled by chalcogenide glass. The all-fiber device is operated in the $2\,\mu$m wavelength band from the efficient FWM of a chalcogenide microwire. Picosecond pulses with femtojoule energy are experimentally characterized, and complex electric fields are recovered with low FROG error. To demonstrate the measurement capability of the FROG device, experiments are carried out with unchirped pulses as well as positively and negatively chirped pulses. The accuracy of the FROG is verified through independent measurements of pulse spectra and autocorrelation traces. This demonstration is a major step towards the development of compact and highly sensitive FROG devices compatible with the mid-IR.

5.2 Theoretical background

Conventional FROG measurement setup is very similar to that of an intensity autocorrelator, except that the photodetector is replaced with a spectrometer. Figure 5.1 shows a typical setup for SHG-based FROG. The input pulse is split into two, and combined at the nonlinear crystal with a variable delay. Recording some tens or hundreds of second-harmonic spectra for different arrival time differences τ of the two pulses results in a spectrogram. A sophisticated iterative phase retrieval algorithm can then be used for reconstructing the complex electric

field of the original pulse from the FROG spectrogram [93].

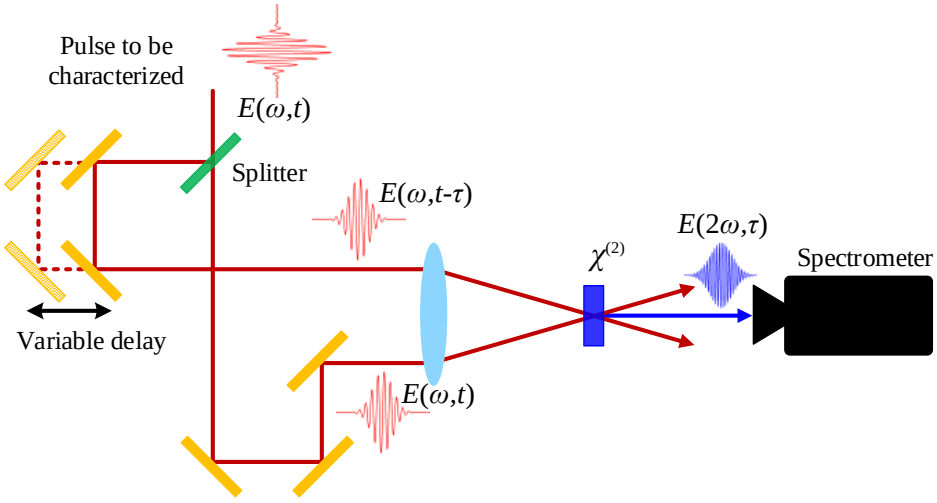

Fig. 5.1 A typical setup for SHG-FROG. The spectrum of the nonlinear mixing product of the pulse and the delayed replica is measured as a function of the relative time delay.

For an input pulse with electric field $E(t)$ and delayed replica $E(t-\tau)$, the SHG signal after the $\chi^{(2)}$ crystal is given by [42]

$$E_{SHG}(t,\tau) = \frac{1}{2}\epsilon_0\chi^{(2)}\left[E^2(t) + E^2(t-\tau) + 2E(t)E(t-\tau)\right]. \tag{5.1}$$

The spectrometer detects only the power spectral density of $E(t)E(t-\tau)$ through aperture, therefore frequency-resolved optical gating (FROG) signal is given by the Fourier transformation [94]

$$I_{FROG}(\omega,\tau) \propto \left|\int_{-\infty}^{+\infty} E(t)E(t-\tau)\exp(-i\omega t)dt\right|^2. \tag{5.2}$$

A FROG retrieval algorithm then starts with an initial guess for the field $E(t)$, generates a signal field $E_{signal}(t,\tau)$. Then Fourier transform of the signal field is compared to the measured FROG trace to generate an improved signal field, which is used to generate a new guess of $E(t)$ for the next iteration. This process is repeated a number of times, with a better guess of $E(t)$ obtained at each iteration, until the algorithm converges. The FROG retrieval error is defined as average root-mean-square difference between the measured and reconstructed FROG traces divided by the number of points in the trace. For a FROG trace

with $N \times N$ points [94]

$$G = \sqrt{\frac{1}{N^2}\sum_{i,j=1}^{N}\left|I_{FROG}^{measured}(\omega_i,\tau_j) - \sigma I_{FROG}^{retrieved}(\omega_i,\tau_j)\right|^2}, \tag{5.3}$$

where σ is a real normalization constant to minimize the error G. $I_{FROG}^{measured}(\omega_i,\tau_j)$ is the measured FROG trace, $I_{FROG}^{retrieved}(\omega_i,\tau_j)$ is the retrieved FROG trace, and ω_i and τ_j are the i-th frequency and j-th delay vectors, respectively. Typically, $G < 1\%$ for accurate FROG reconstructions limited by the experimental error. Larger N leads to lower FROG error, due to the fast Fourier transform relations between the time delay and frequency axis ranges and steps [105].

Figure 5.2 shows a block diagram of a FWM-based FROG. Similar to conventional SHG-based FROG systems, input pulses are split, delayed and then recombined and sent into the nonlinear medium along with a CW laser. For a pump electric field $E_{pulse}(t) + E_{pulse}(t-\tau)$, combined with the CW probe electric field E_{CW}, the generated idler electric field $E_{idler}(t,\tau)$ can be obtained from equation 4.5. If self-phase modulation (SPM), cross-phase modulation (XPM) and fiber losses are ignored, the output idler electric field is given by [2]

$$E_{idler}(t,\tau) = \frac{\gamma}{\Delta\beta}E_{CW}^{*}\left[E_{pulse}^{2}(t) + E_{pulse}^{2}(t-\tau) + 2E_{pulse}(t)E_{pulse}(t-\tau)\right], \tag{5.4}$$

where $\Delta\beta$ is linear phase mismatch, given by equation 4.2. The first two terms in between brackets represent a constant background in spectrum that is invariant of time delay, which can be subtracted from the measurement to produce a background-free spectrogram identical to that from conventional SHG-based FROG. The FROG trace is then identical to the one given by equation 5.2.

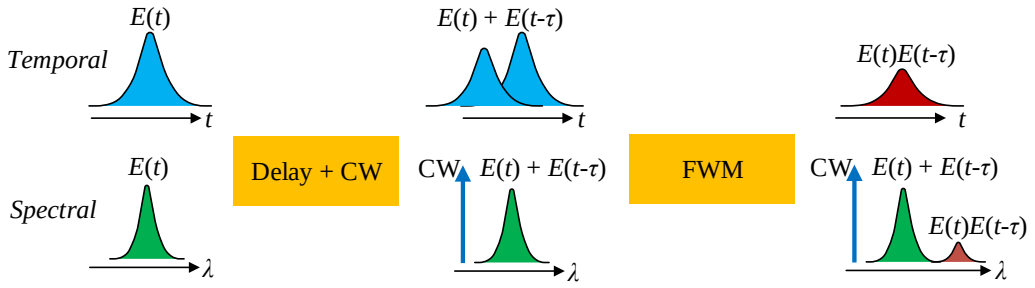

Fig. 5.2 A block diagram of a FWM-based FROG.

5.3 Microwire design and fabrication

The microwire used in this investigation is fabricated from a three layer hybrid fiber that consists of an As_2Se_3 core, a Cyclo Olefin polymer (COP) cladding and an outer layer of polymethyl methacrylate (PMMA), following the procedure detailed in Ref. [24], as described in section 4.3. Effective phase-matching for parametric conversion has been demonstrated in chalcogenide microwire at frequency shifts up to 49.3 THz [18]. With these microwires, electric field of ultrafast pulses in the mid-IR can be characterized by wavelength conversion to short-wave infrared, where highly sensitive optical spectrum analyzers and photodetectors are commercially available.

For the specific application of a FROG device enabling the characterization of pulses at a wavelength of $\sim$1.935 μm, the microwire core is designed with a diameter of 1.48 μm. The lengths of the microwire and of each transition section are 11 cm and 2 cm, respectively. The microwire possesses a waveguide nonlinearity of $\gamma = 24\,\mathrm{W^{-1}m^{-1}}$, and group velocity dispersion $\beta_2 = -0.11\,\mathrm{ps^2/m}$ at the wavelength of 1.935 μm. Both ends of the hybrid fiber are polished and butt-coupled to SMF-28 via UV-cured epoxy and result in a SMF to SMF insertion loss of 5.5 dB.

5.4 Experiment and results

Figure 5.3 shows the experimental setup of the FROG device. The structure of the FROG begins with an all-fiber delayed Mach-Zehnder interferometer (MZI) to produce two pulses separated by a variable delay. The MZI is constructed with a pair of fiber couplers, a tunable optical delay line on one arm, and a piezoelectric transducer that dithers the length on the other arm to eliminate the undesired interference between delayed pulses. The path length variation in the dithered arm is much smaller than the delay steps to ensure a good accuracy of measurement. While the pulses to be characterized serve as pump in the FWM process, a wavelength tunable thulium-doped fiber laser serves as a continuous-wave (CW) probe signal. Pump and probe are coupled into a chalcogenide microwire via an 80/20 silica fiber coupler (FC3), combining 20% of the pump and 80% of the probe signal, while the second output port of FC3 is used to monitor the power. If a wavelength division multiplexing (WDM) coupler that couples 100% of both the pump and the probe were used, the required pump power at the input of the FROG setup could be lowered by a factor of 25 for the same probe power coupled into the mirowire. Since the idler power is proportional to the probe power, sensitivity of the FROG could also be improved by increasing the coupled probe power.

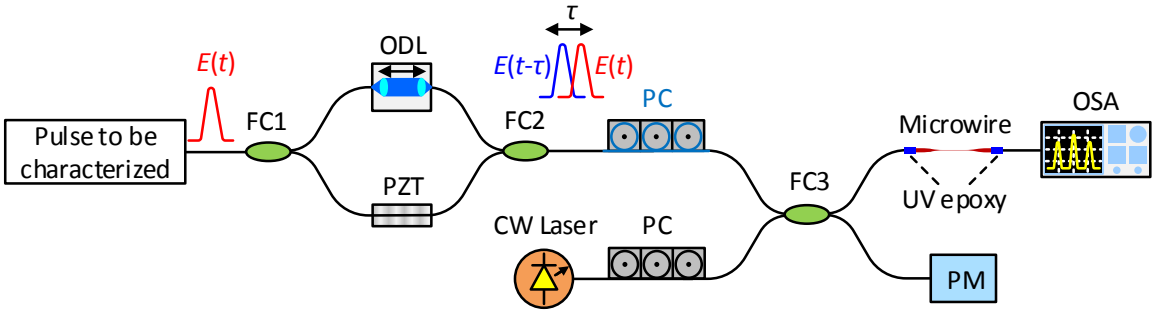

Fig. 5.3 Experimental setup of the FWM-based FROG. FC, fiber coupler; ODL, optical delay line; PZT, piezoelectric transducer; PC, polarization controller; OSA, optical spectrum analyzer; PM, power meter.

In the FROG device, the polarization states of pump and probe are co-aligned using polarization controllers. The polarization controller on the pump arm is made of normal dispersion fiber to compensate for the chromatic dispersion that the pulse experiences before reaching the microwire. The average and peak pump powers coupled into the microwire are 4 μW and 40 mW, corresponding to a pulse energy of 135 fJ, while the CW wavelength is fixed at 1.920 μm with an input probe power of 7 mW. The pump power in the microwire induces a nonlinear phase shift $\phi_{NL} = \gamma P L_{eff} = 0.07$ rad, which satisfies the maximum peak power criteria for negligible pulse distortion induced by XPM [97]. Considering the low pump power, FWM process takes place mainly in the realm of linear phase matching $\Delta\beta = \beta_2\Omega^2 + \beta_4\Omega^4/12$, where β_2 and β_4 are the second and fourth order dispersion coefficients, respectively, and Ω is the angular frequency difference between pump and probe signal. In the present device, dispersive effects at the pump wavelength of 1.935 μm limit the minimum measurable pule duration to 820 fs [97]. However, by operating at zero dispersion wavelength or using a microwire designed with zero dispersion at the measurement wavelength, pulses as short as ~200 fs could be accurately characterized by this FROG device, limited only by the third-order dispersion [98].

Figure 5.4 shows a typical FWM spectrum at the output end of the microwire, with zero delay in the MZI. While XPM is noticeable on the probe spectrum, no trace of spectral broadening due to the SPM is observable on the pump spectrum. Small dips on the pump spectrum are caused by atmospheric water absorption in the optical spectrum analyzer (OSA) with a resolution bandwidth set to 1 nm. There is no observable Raman gain contribution to the idler as the Raman gain offset by 6.7 THz (or 87 nm) to the longer wavelength

side of the pump [104], much further away than the idler which is 1.2 THz (or 15 nm) offset from the pump. During the FROG experiments, only the output idler spectra are recorded on the OSA at each delay line setting to generate the spectrogram. The background spectrum is acquired at a large delay setting, where there is no temporal overlap between pulses from two arms of the delayed MZI, and eventually subtracted from the spectrogram. The entire characterization process is fully automated using Python script.

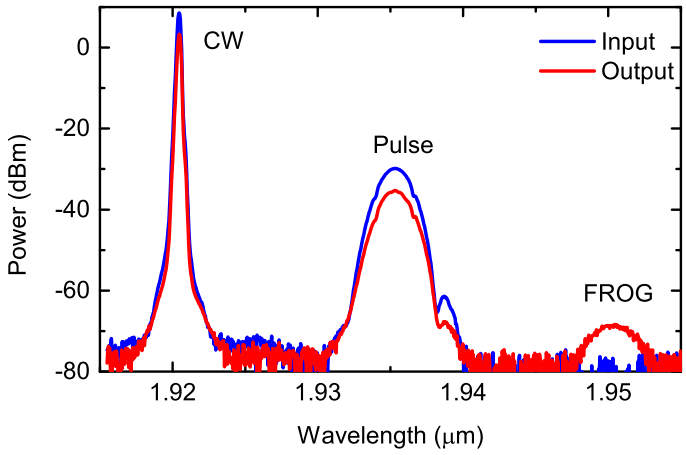

Fig. 5.4 Optical spectra measured at the input and output ends of the microwire.

Pulses to be characterized are generated from a mode-locked thulium-doped fiber laser at a central wavelength of 1.935 μm, a duration of $\sim$3 ps and at a repetition rate of 30 MHz. In a first experiment, pulses from this laser are sent directly to the FROG device. Figure 5.5(a) shows the measured spectrogram after background subtraction and noise filtering on a 64×64 grid. Then the input pulse electric field is reconstructed by a standard SHG-FROG algorithm [93], and result into a FROG retrieval error $G = 0.0074$. The sensitivity of the FROG is 0.16 mW^2 in this situation. Figure 5.5(b) shows the retrieved amplitude and phase in time and frequency domains, respectively. Retrieved pulse width FWHM is 3.08 ps, and spectral width is 1.8 nm. Corresponding to a time-bandwidth product is 0.44, confirming the near transform-limited nature of the pulse with a Gaussian temporal shape. Pulse autocorrelation and spectrum are independently measured using an autocorrelator and OSA. An excellent agreement is found with the retrieved autocorrelation and spectrum, as shown in the inset of Figure 5.5(b). Temporal and spectral phase exhibit a slight residual chirp. The same measurement is repeated with a pump power coupled to the microwire increased to 6 μW, instead than the nominal 4 μW. As a result of improved signal-to-noise ratio, the retrieved FROG error is reduced to $G = 0.005$.

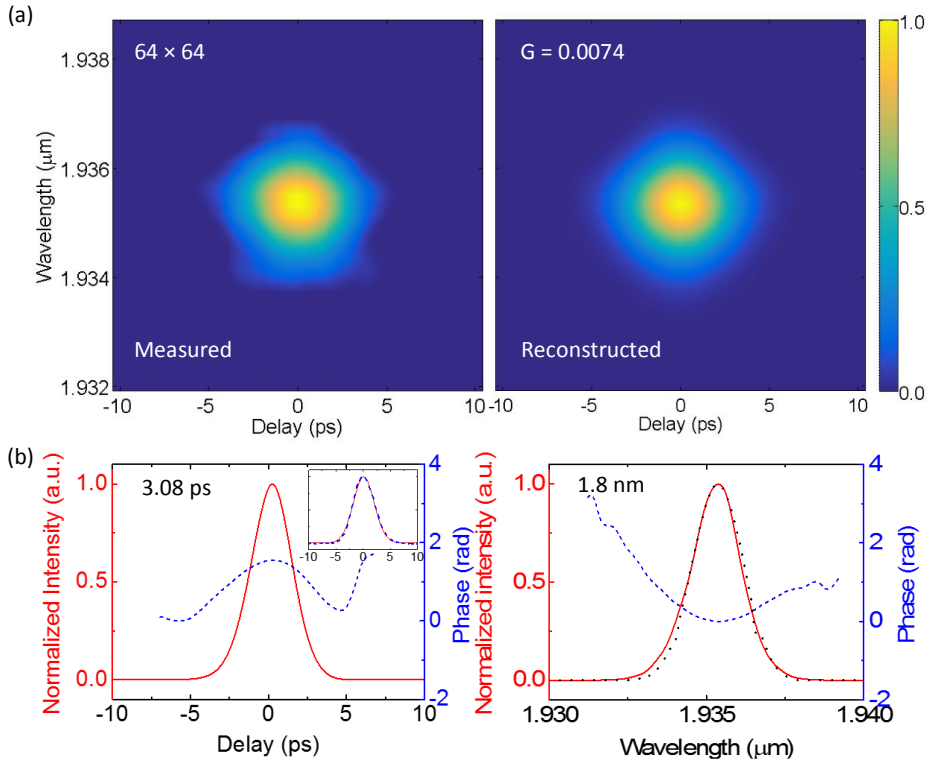

Fig. 5.5 (a) Measured and reconstructed FROG spectrograms. (b) Retrieved pulse shape (solid) and temporal phase (dashed), inset: retrieved autocorrelation (solid) and measured autocorrelation (dashed); Measured spectrum (dotted), retrieved spectrum (solid) and spectral phase (dashed).

To further investigate the measurement capability of the FROG device with variable characteristics, additional experiments are carried out with segments of optical fibers with either anomalous or normal dispersion, inserted in between the pump laser and the FROG device. The chromatic dispersion of the inserted fiber determines the signs of the retrieved temporal and spectral phases. Figure 5.6 shows the measurement and FROG reconstruction results of the 3 ps pulses anomalously chirped in 100 meters of SMF-28 fiber, with a FROG error G = 0.0088. Retrieved pulse width FWHM is 5.29 ps, and spectral width is 1.9 nm. Corresponding time-bandwidth product is 0.78. Retrieved autocorrelation and spectrum have good agreement with the measured autocorrelation and spectrum. Both temporal phase and spectral phase are predominantly parabolic. The sign of the spectral phase, hence the direction-of-time, is identified from the anomalous dispersion expected from SMF-28 fiber in the spectral range. Fitting the spectral phase profile results in a quadratic phase coefficient of –2.4 ps^2, corresponding to a dispersion coefficient $\beta_2 \cong$–0.048 ps^2/m, close to the value –0.068 ps^2/m reported in the literature [106].

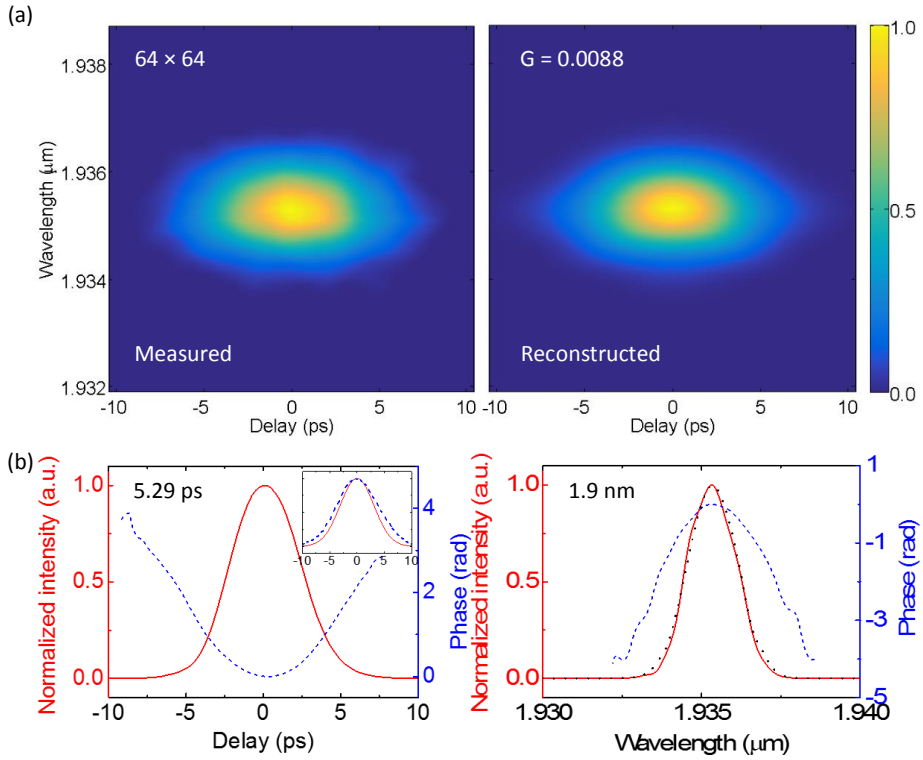

Fig. 5.6 (a) Measured and reconstructed FROG spectrograms of anomalously chirped pulses. (b) Retrieved pulse shape (solid) and temporal phase (dashed), inset: retrieved autocorrelation (solid) and measured autocorrelation (dashed); Measured spectrum (dotted), retrieved spectrum (solid) and spectral phase (dashed).

Figure 5.7 shows the measurement and FROG reconstruction results of 3 ps pulses normally chirped in 40 meters of ultra-high numerical aperture fiber (Nufern UHNA7). Retrieved pulse width FWHM is 3.55 ps, and spectral width is 2.5 nm, with a FROG error G = 0.0132. Corresponding time-bandwidth product is 0.68. Due to high nonlinearity in UHNA7 fiber, pulses experience a spectral broadening as well. Again, retrieved autocorrelation and spectrum have good agreement with the measured ones. Both temporal phase and spectral phase are predominantly parabolic. The sign of the spectral phase, hence the direction-of-time, is identified from the anomalous dispersion expected from SMF-28 fiber in the spectral range. Fitting the spectral phase profile results in a quadratic phase coefficient of 0.7 ps^2, corresponding to a dispersion coefficient of UHNA7 fiber $\beta_2 \cong 0.035\,ps^2/m$, in good agreement with the value 0.039 ps^2/m reported in the literature [107].

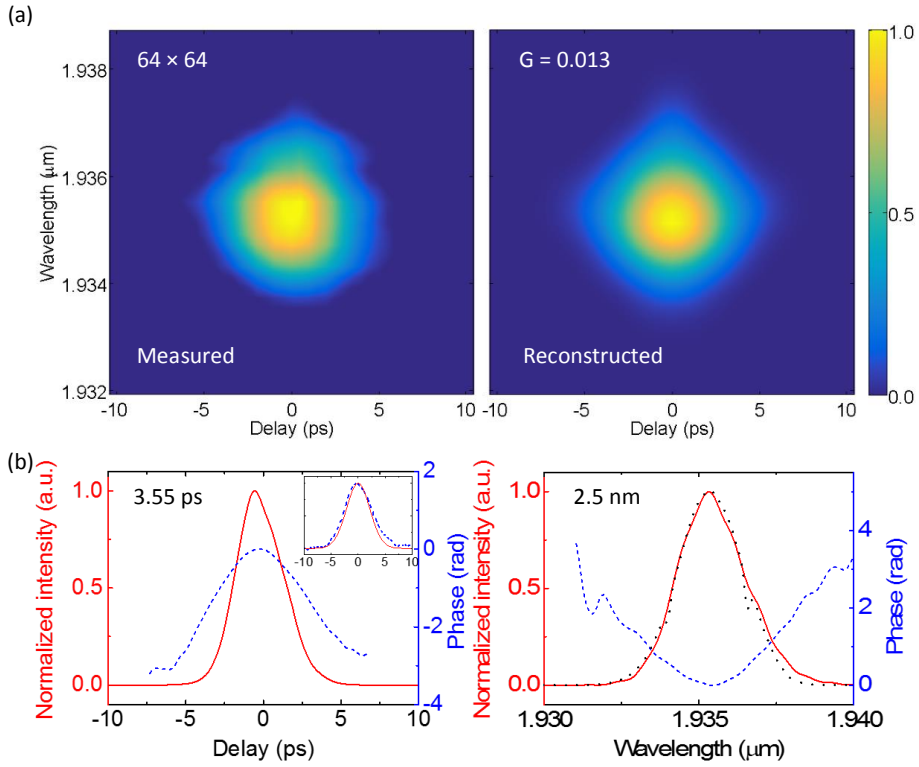

Fig. 5.7 (a) Measured and reconstructed FROG spectrograms of normally chirped pulses. (b) Retrieved pulse shape (solid) and temporal phase (dashed), inset: retrieved autocorrelation (solid) and measured autocorrelation (dashed); Measured spectrum (dotted), retrieved spectrum (solid) and spectral phase (dashed).

5.5 Summary

In conclusion, we have demonstrated the first all-fiber FROG device from chalcogenide glass. Thanks to high nonlinearity and transparency of chalcogenide glasses in the wavelength band of 2 μm, dispersion engineered chalcogenide microwires enable efficient FWM and thus high-sensitivity FROG characterization. The all-fiber architecture in this demonstration eliminates critical alignment requirements and represents an important step towards the fabrication of highly sensitive FROG devices compatible with the mid-IR. Appropriate microwire structures compatible with longer wavelengths of the mid-IR could be used for this purpose, as well as replacing silica-based fiber components with the ones that are made of mid-IR compatible fibers such as chalcogenide and ZBLAN. Measurement sensitivity could be further improved by reducing losses in the setup and increasing the probe signal power. The optical spectrum analyzer measurement sensitivity will eventually limit the achievable

FROG sensitivity, becasue a reasonable signal-to-noise ratio of the idler spectrum is required to obtain accurate field reconstruction. Microwire core diameter fluctuation, illustrated in figure 4.4, is not expected to have significant impact on the performance of the FROG presented in this chapter, since the microwire has appreciable anomalous dispersion, and therefore the parametric gain profile of the microwire is not susceptible to slight fluctuations in core diameter along the length of the microwire. However, dispersion fluctuation can considerably diminish the performance of the FROG when operated at zero dispersion wavelength or in the normal dispersion regime.

Chapter 6

Pulse characterization based on cross-phase modulation in chalcogenide microwires

[1]In this chapter, we report the first all-fiber frequency-resolved optical gating (FROG) based on cross-phase modulation in chalcogenide glass. The amplitude and phase of pulses as short as 390 fs at femtojoule energy levels are accurately characterized without direction-of-time ambiguity in the retrieved pulse. A measurement sensitivity of 18 mW^2 is achieved from the strong nonlinearity of a 10 cm long chalcogenide microwire.

6.1 Introduction

As described in chapter 5, frequency-resolved optical gating (FROG) is a well-established technique for complete characterization of pulse amplitude and phase [93]. The basic principles that support FROG functionality include polarization gating (PG), self-diffraction (SD), second-harmonic generation (SHG), third-harmonic generation (THG), and transient gating (TG). Currently, SHG-based FROG is the most widely used pulse characterization technique [94]. The main drawback of SHG-based FROG is the unresolved ambiguity on the direction of time, such that a pulse and its temporally reversed replica results in the same FROG trace, thus preventing unique determination of the spectral phase sign. There is also ambiguity in the relative phase of distinct multiple pulses, which means that relative phases

[1]Part of the content in this chapter has been subject to publication in (1) N. Abdukerim, I. Alamgir and M. Rochette, Pulse characterization by cross-phase modulation in chalcogenide glass, Optics Letters 43(19), 4771–4774 (2018).

of ϕ and $\phi + \pi$ for various pulses is interpreted as the same for a SHG-based FROG [93].

Alternatively, optical fibers and waveguides have been successfully used for FROG pulse characterization using third order nonlinear effects, such as based on cross-phase modulation (XPM) in the 1.55 μm wavelength band [98, 100, 102, 108–110]. Fiber-based FROG devices offer high sensitivity and alignment-free architecture. Despite rapid development of mid-IR sources and increasing interest in complete pulse characterization, no XPM-based FROG devices in optical fiber or waveguide have been demonstrated beyond wavelengths of the 1.55 μm band. Close to this is the all-fiber FROG in the 2 μm wavelength band based on four-wave mixing (FWM), presented in chapter 5. One constraint of FWM-based FROGs is the requirement of a continuous wave probe laser and the unresolved temporal ambiguity. In contrast, XPM-based FROGs do not require a probe laser while providing FROG traces reflecting pulse symmetry and chirp characteristics, consequently eliminating temporal ambiguity in the retrieved pulse [98].

Tight modal confinement in a microwire geometry with a large core to cladding refractive index contrast significantly enhances the waveguide nonlinearity $\gamma = k_0 n_2 / A_{eff}$, concurrently allowing chromatic dispersion to be widely engineerable [19,49–51]. Chalcogenide microwires have demosntrated their effectiveness for nonlinear processing in the mid-IR [23, 111].

In this chapter, we demonstrate an all-fiber FROG device based on XPM of a highly nonlinear chalcogenide microwire. Amplitude and phase profiles of femtosecond pulses in the 2 μm wavelength band are accurately characterized without ambiguity in the direction-of-time. The FROG measurement accuracy is verified through independent measurements of optical spectra and autocorrelation traces. The wide transmission window of chalcogenide glass combined with high nonlinearity allows highly sensitive ultrafast pulse characterization in the mid-IR.

6.2 Theoretical background

The propagation evolution of two orthogonally polarized optical fields in the microwire is governed by the following coupled nonlinear Schrödinger equation (NLSE), assuming the microwire is weakly birefringent and neglecting FWM [2]

$$\begin{aligned} \frac{\partial A_x}{\partial z} + \frac{i\beta_{2x}}{2}\frac{\partial^2 A_x}{\partial T^2} + \frac{\alpha}{2}A_x &= i\gamma_x \left[|A_x|^2 + \frac{2}{3}|A_y|^2 \right] A_x, \\ \frac{\partial A_y}{\partial z} + d\frac{\partial A_y}{\partial T} + \frac{i\beta_{2y}}{2}\frac{\partial^2 A_y}{\partial T^2} + \frac{\alpha}{2}A_y &= i\gamma_y \left[|A_y|^2 + \frac{2}{3}|A_x|^2 \right] A_y, \end{aligned} \tag{6.1}$$

where subscripts x and y denote axes of linearly polarized slowly varying amplitudes A_x and A_y, time T is a reference frame moving with the x-polarized pulse, and d is the walk-off due to birefringence in the microwire. By neglecting dispersive effects and plarization-mode dispersion (PMD), assuming $\gamma_x = \gamma_y = \gamma$, an analytical solution to the above system of coupled NLSE can be found

$$A_{x,y}(z,t) = A_{x,y}(0,t)exp\left[i\gamma|A_{x,y}(0,t)|^2 z + \frac{i2\gamma}{3}|A_{y,x}(0,t)|^2 z\right]. \tag{6.2}$$

In the microwire, each of the two orthogonally polarized pulses delayed by τ, experiences a nonlinear phase shift due to self-phase modulation (SPM) effect and XPM from the other co-propagating pulse with orthogonal polarization state, which is manifested in optical spectrum as delay-dependent spectral modulation. The mean frequency of the FROG spectrogram is directly linked to the autocorrelation of the pulse in time domain. If the pulses with x polarization state are selected by the polarizer before the optical spectrum analyzer, the FROG signal is given by [98]

$$A_{SIG}(t,\tau) = A_x(t)exp\left\{i\gamma L_{eff}\left[|A_x(t)|^2 + \frac{2}{3}|A_y(t-\tau)|^2\right]\right\}, \tag{6.3}$$

where $L_{eff} = (1-exp(-\alpha L))/\alpha$ is the effective nonlinear length of the microwire with length L and attenuation coefficient α. The first term in between brackets represent a constant SPM independent of time delay, and second term is the delay-dependent XPM induced by the pulse with orthogonal polarization state. The FROG spectrogram is the squared modulus of the Fourier transformed $A_{SIG}(t,\tau)$, can be written as

$$I_{FROG}(\omega,\tau) = \left|\int_{-\infty}^{\infty} A_x(t)exp\left\{i\gamma L_{eff}\left[|A_x(t)|^2 + \frac{2}{3}|A_y(t-\tau)|^2\right]\right\} exp(i\omega t)dt\right|^2, \tag{6.4}$$

from which the amplitude and phase of the pulses are retrieved by the principle component generalized projections algorithm [112]. The gate function is the phase modulation on the probe pulse given by the exponential term. Unlike the FROG signal from FWM in the previous chapter, this FROG signal is asymmetric in time, meaning that $A(t-\tau)$ and $A(\tau-t)$ would result in different FROG spectrograms. This property allows uniquely determining the sign of spectral phase during electric field reconstruction by the phase retrieval algorithm.

6.3 Microwire design and fabrication

The microwire used to generate XPM is fabricated from a three layer hybrid fiber that consists of an As_2Se_3 core, a Cyclo Olefin polymer (COP) cladding and an outer layer of poly-methyl methacrylate (PMMA), following the procedure detailed in [24], as described in section 4.3. Zero dispersion can be achieved at any wavelength up to 6 μm, enabling XPM-FROGs to operate efficiently in this range of wavelengths from high refractive index contrast chalcogenide microwires with minimum incidence of chromatic dispersion. At zero dispersion wavelength, minimum measurable pulse width is only limited by third-order dispersion (TOD). Sub-100 fs pulses could be characterized by using a shorter microwire at the expense of a decreased sensitivity.

For the current experiment, the FROG device is built with an intent to characterize femtosecond pulses at a wavelength of $\sim$1.937 μm. For this purpose, the microwire core is designed with a diameter of 1.6 μm to achieve near zero dispersion. Experimentally, the microwire is precisely set to zero dispersion from an *in situ* fabrication technique that involves real-time monitoring of the parametric conversion efficiency [56]. Prior to tapering, both ends of the hybrid fiber are polished and butt-coupled to SMF-28 via UV-cured epoxy. An experiemental setup similar to the one shown in Figure 4.5(a) is used to monitor the parametric conversion efficiency, with a thulium-doped fiber laser constructed similar to Figure 3.3(b) is used as the probe signal. The probe signal wavelength is fixed at 1.744 μm, where the parametric gain is maximum, and the average probe power coupled into the hybrid fiber is kept at 0.3 mW. The coupled peak pump power is 3.8 W. The FWM spectrum is monitored during the tapering process, starting from the point when the actual microwire diameter is expected to be close to the target diameter of 1.6 μm. Figure 6.1 shows the measured FWM spectrum, and the expected parametric gain spectrum for a peak pump power of 3.8 W with targeted dispersion parameters, calculated from the matrix method given in equation 4.6. When the actual microwire diameter asymptotically approaches the target diameter, the idler appears at the expected wavelength of 2.167 μm. The idler power is continuously monitored, and the tapering processes is aborted once the idler power reaches maximum value. The accuracy of the fabricated microwire diameter is estimated to be within a few nanometers.

The lengths of the microwire and of each transition section are 10 cm and 2.5 cm, respectively, with 4 cm of hybrid fiber section at each end. The nonlinear refractive index of ($n_2 = 7.6\times10^{-18}$ m^2/W) [39], combined with the strong modal confinement in the microwire leads to a waveguide nonlinearity of $\gamma = 21$ W^{-1}m^{-1}, and third order dispersion $\beta_3 = 3.51\times10^{-3}$ ps^3/m

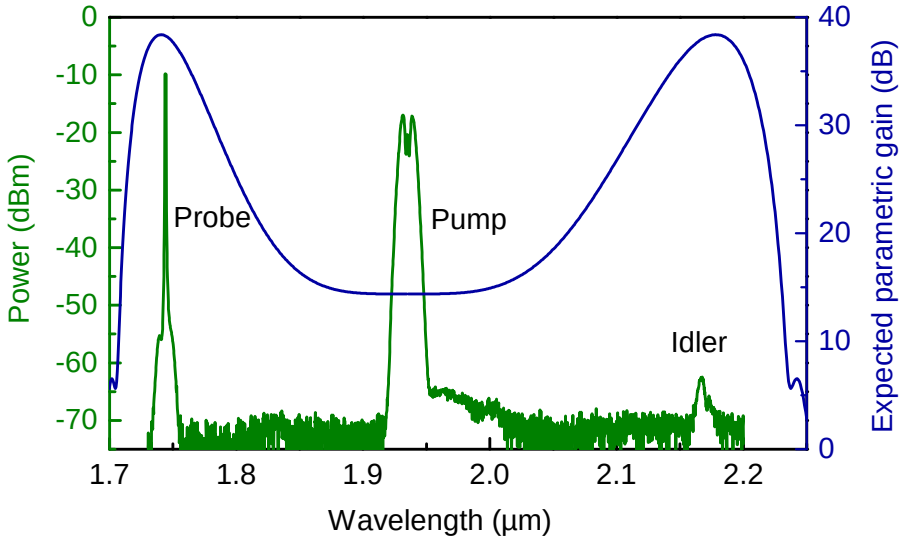

Fig. 6.1 Measured FWM spectrum and calculated parametric gain spectrum for the same peak pump power.

all at a wavelength of 1.937 μm. SMF to SMF insertion loss of the tapered fiber is 5 dB, including 0.2 dB/cm of propagation loss in the microwire due to polymer absorption and microwire core diameter roughness, and the rest is attributed to Fresnel reflection loss at chalcogenide-silica interfaces, optical fiber mode mismatch and misalignment losses.

The microwire possesses a small amount of linear birefringence due to residual stress of the COP cladding that emerges from the tapering process. The magnitude of birefringence is controllable over some extent by adjusting the tapering temperature [113]. The birefringence of the microwire is experimentally measured at $B_m = 2.4 \times 10^{-4}$ from spectral polarization method [114]. Due to this residual birefringence in the microwire, it is not favorable to work with circularly polarized pulses, because circularly polarized modes in the microwire would couple through linear birefringence [109].

6.4 Experiment and results

Figure 6.2 shows the experimental setup of the XPM-based FROG device. Pulses to be characterized are provided by a mode-locked thulium-doped fiber laser followed by a variable attenuator. Pulses sent to the FROG device in a first experiment have a FWHM duration of ~850 fs at a repetition rate of 30 MHz centered at a wavelength of 1.937 μm. The FROG device begins with an in-line polarization controller to adjust the polarization

splitting ratio in the delayed Mach-Zehnder interferometer (MZI). The MZI itself is composed of a polarization beam splitter that produces two orthogonally polarized pulses before recombining them with a second polarization beam splitter. In one arm of the MZI, a motorized variable optical delay line (ODL) is added to induce time delay between a pair of pulses. In the other arm of the MZI, a piezoelectric transducer dithers the optical path at a frequency of 0.6 kHz, in order to eliminate interferometric fringes that otherwise would modulate the XPM spectrum in a noise-like fashion. The path delay variation in the dithered arm is less than a femtosecond, which has negligible impact on the measurement accuracy. In the MZI, polarization controllers made of normal dispersion fibers partially compensate the anomalous dispersion caused by standard SMF pigtails of the optical components used in the FROG setup. Additional dispersion compensation is provided by a 6 m long normal dispersion fiber (NDF) following the MZI. A COP-cladded chalcogenide microwire is then used for XPM processing. The output of the microwire is filtered through the combination of a polarization controller and an in-line polarizer to isolate one of the linear polarization states. An optical spectrum analyzer (OSA) records spectra at each delay setting to generate the FROG spectrogram. The entire characterization process is fully automated using Python script to ensure reproducibility.

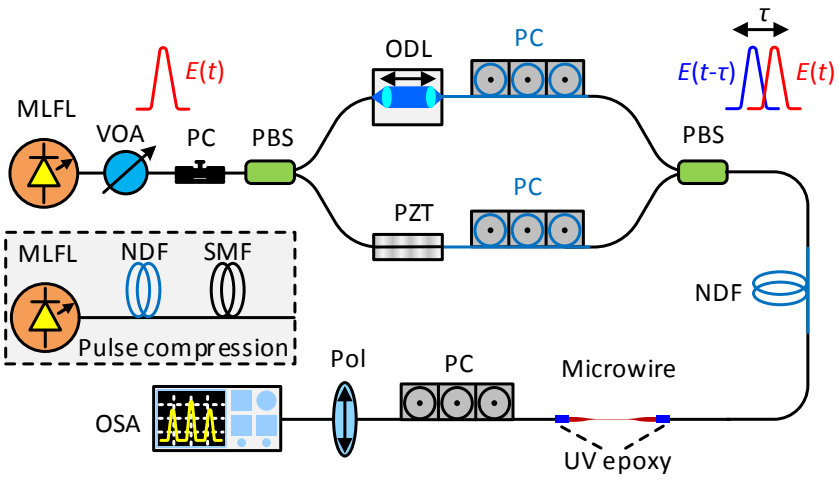

Fig. 6.2 Experimental setup of the XPM-based FROG. VOA, variable optical attenuator; PBS, polarization beam splitter; ODL, optical delay line; PZT, piezoelectric transducer; PC, polarization controller; NDF, normal dispersion fiber; Pol, polarizer; OSA, optical spectrum analyzer; Inset: pulse compression stage

The average and peak pump powers coupled into the microwire are 11 μW and 410 mW on each polarization axis, corresponding to a pulse energy of 367 fJ. The pump power in the microwire induces a XPM phase shift $\phi_{XPM} = \frac{2}{3}\gamma P L_{eff} = 0.45$ rad. In theory, a nonlinear phase shift as low as 0.1 rad is sufficient to ensure XPM-based pulse characterization [98]. Since $\beta_2 \cong 0$ in the present device, third-order dispersive effects at the wavelength of 1.937 μm limit the minimum measurable pulse duration to $T_0 \geq (20|\beta_3 L|)^{1/3} \cong 200$ fs [98]. Residual birefringence in the microwire also generates a differential group delay of 80 fs due to PMD, a negligible amount with respect to the one from third-order dispersion.

Figure 6.3(a) shows a typical measurement spectrogram after noise removal on a 64×64 grid. The spectrogram is reconstructed with a FROG retrieval error $G = 0.0009$, defined in equation 5.3. In this situation, the sensitivity of the FROG is 18 mW^2. Figure 6.3(b) shows the retrieved amplitude and phase in time and frequency domains, respectively. Temporal and spectral phase exhibit a slight residual chirp, possibly resulting from the mode-locked fiber laser itself or imperfect dispersion compensation in the FROG device. Retrieved pulse width FWHM is 830 fs, and spectral width is 6.9 nm. Corresponding time-bandwidth product is 0.45, close to the transform-limit of Gaussian pulses. Pulse autocorrelation and optical spectrum are independently measured using an autocorrelator and OSA. An excellent agreement is found with the retrieved autocorrelation and optical spectrum, as shown in Figure 6.3(b).

To further investigate the measurement capability of the FROG device with ultrafast pulses, additional experiments are carried out with compressed pulses. As shown in the inset of Figure 6.2, the pulses from the mode-locked fiber laser are compressed using 5 m long UHNA7 (Nufern) fiber with high nonlinearity and normal dispersion for spectral broadening, followed by 2.8 m long SMF-28 for dispersion compensation. In this case, the average pump power coupled into the microwire is reduced to 7 μW on each polarization axis. Figure 6.4 shows the measurement and FROG reconstruction results of the pulses with a FROG error $G = 0.0011$. Retrieved pulse width FWHM is 390 fs, and spectral width is 19.2 nm. Corresponding time-bandwidth product is 0.59. Residual chirp is observable in the retrieved pulse, which contributes to the increase in the pulse width longer than the transform-limit. Retrieved autocorrelation and spectrum have good agreement with the measured autocorrelation and optical spectrum.

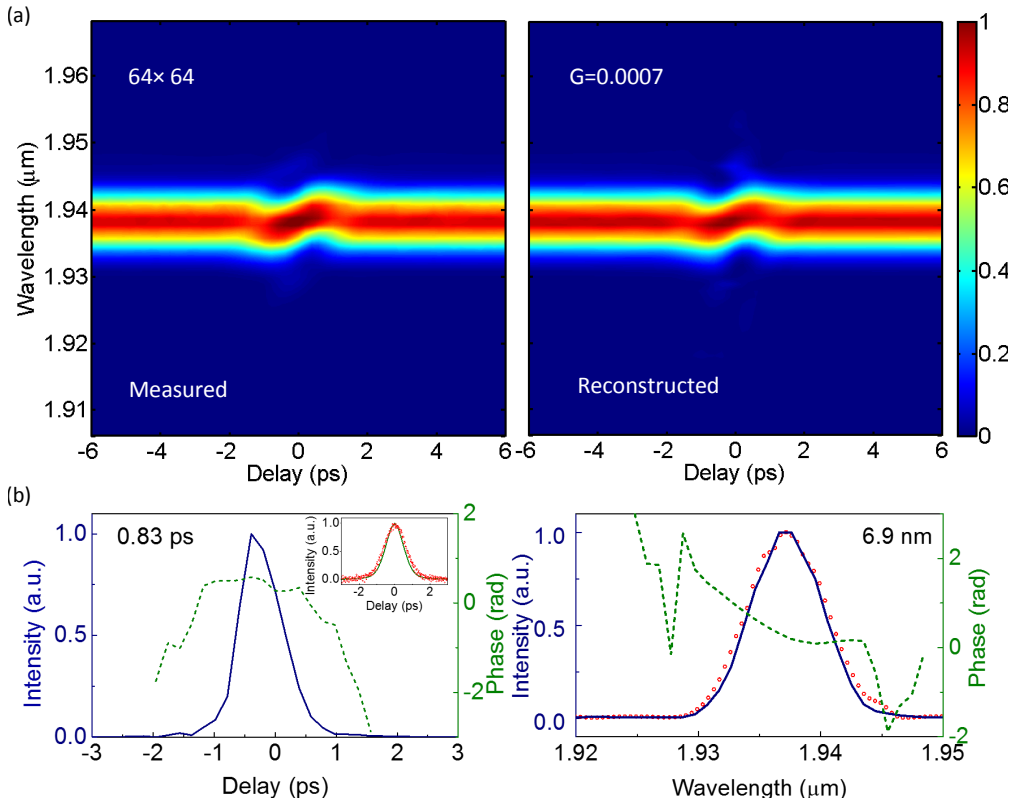

Fig. 6.3 (a) Measured and reconstructed FROG spectrograms. (b) Retrieved pulse shape (solid) and temporal phase (dashed), inset: retrieved autocorrelation (solid) and measured autocorrelation (circles); Retrieved spectrum (solid), spectral phase (dashed), and measured spectrum (circles).

6.5 Summary

In conclusion, we have demonstrated an all-fiber FROG device based on XPM in chalcogenide glass. The COP-cladded chalcogenide microwire possesses good transparency and high nonlinearity in the 2 μm wavelength band. A 10 cm long microwire with zero dispersion enables high-sensitivity FROG characterization. With the freedom of dispersion engineering, FROG pulse characterization using chalcogenide microwires is accessible over a wide range of mid-IR wavelengths. The characterization wavelength of such a FROG device could be further extended towards longer wavelengths by replacing silica-based fibers with mid-IR compatible chalcogenide or ZBLAN fibers.

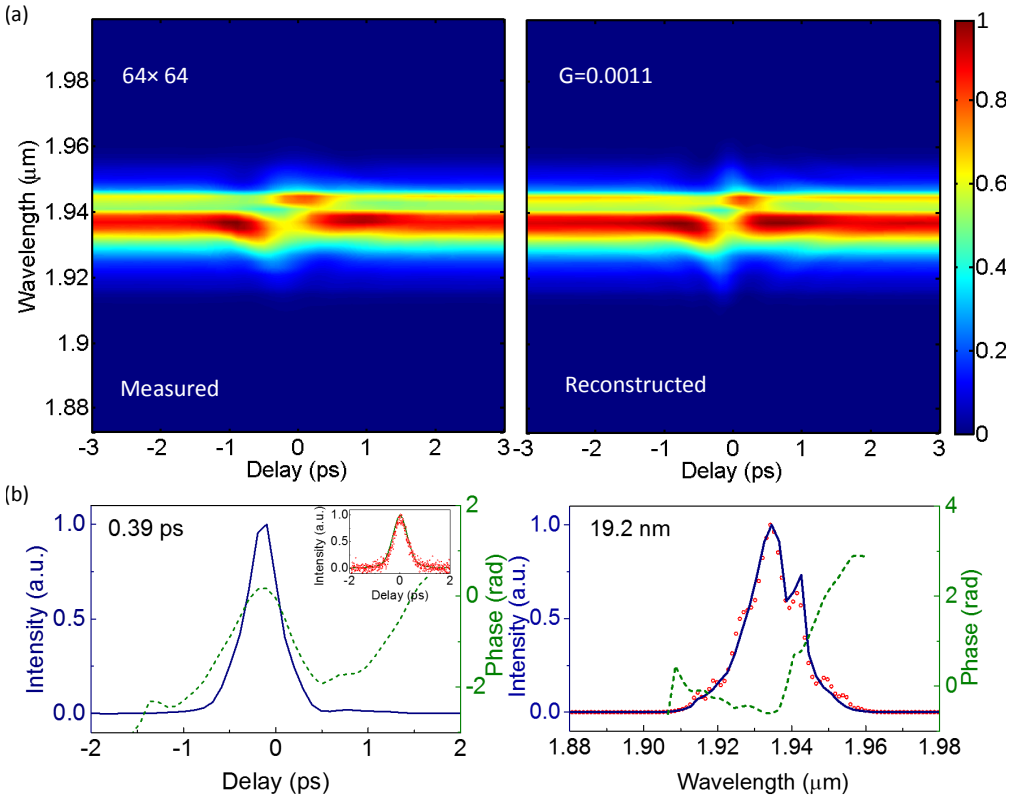

Fig. 6.4 (a) Measured and reconstructed FROG spectrograms of compressed pulses. (b) Retrieved pulse shape (solid) and temporal phase (dashed), inset: retrieved autocorrelation (solid) and measured autocorrelation (circles); Retrieved spectrum (solid), spectral phase (dashed), and measured spectrum (circles).

Chapter 7

Conclusion and outlook

This thesis summarizes my research efforts over the past five years, towards the development of mid-IR nonlinear fiber sources and ultrafast pulse characterization devices using highly nonlinear chalcogenide microwires. The high nonlinearity in chalcogenide microwires, combined with the flexibility in dispersion engineering, is utilized to develop compact, low threshold, power efficient and widely wavelength tunable pulsed sources in 2 μm wavelength band. To address the challenges in characterization of the output pulses from these optical sources, alignment-free and highly sensitive FROG devices are developed based on efficient nonlinear effects in polymer-cladded chalcogenide microwires. In this thesis, first, the operation of a pulsed Raman fiber laser using a multimaterial chalcogenide microwire is presented. The Raman fiber laser emits at 2.025 μm from pump pulses centered at a wavelength of 1.938 μm, with a wavelength tunable range of 8 nm, limited by the Raman gain bandwidth. However, the output wavelength range of the Raman fiber laser could be significantly extended towards longer wavelengths by utilizing second or higher order Raman shift. With dual-chalcogenide core/cladding composition, the microwire is a promising medium for power efficient nonlinear applications in the mid-IR wavelength range up to 11 μm, only limited by the transmission window of the cladding chalcogenide material. Important insights into the output characteristics of the Raman fiber laser are obtained through numerical simulations. Secondly, the first FOPO using a COP-cladded chalcogenide microwire is demonstrated. The FOPO oscillates solely from the strong parametric gain in a 10 cm microwire, without the support of Raman gain. The output Stokes signal wavelength is tunable over 55 nm, while the entire output wavelength from the FOPO covers a total tunable range of 290 nm, with the help of cascaded parametric generation. The output wavelength range can be further extended by optimizing the cavity design and microwire structure. The COP cladding preserves transparency in 2 μm wavelength band, and also helps engineering of the microwire

chromatic dispersion profile, which is crucial for phase-matching for efficient parametric processes. This microwire structure is the foundation for the realization of following all-fiber FROG pulse characterization devices. The first FROG device is based on efficient FWM in a dispersion-engineered chalcogenide microwire, with a sensitivity level of orders of magnitude higher than conventional FROG architectures based on $\chi^{(2)}$ nonlinearity in crystals. However, limitations of FWM-based FROGs are unresolved temporal ambiguity and the the requirement of a continuous wave probe laser, which limits the characterization wavelength. To overcome these limitations, a second FROG device is developed based on XPM in chalcogenide microwire fabricated with zero dispersion. Complete electric fields of ultrafast pulses with femtojoule pulse energy are accurately characterized by both FROG devices. With the freedom of dispersion engineering, FROG pulse characterization using chalcogenide microwires is accessible over a wide range of mid-IR wavelengths. These FROG devices are important demonstrations towards the development of compact and highly sensitive pulse characterization techniques in the midIR. The characterization wavelength of such a FROG devices could be further extended towards long er wavelength by replacing silica-based fibers with mid-IR compatible chalcogenide or ZBLAN fibers.

The ultrafast pulse generation and characterization techniques described in this thesis are developed in 2 μm wavelength band, where the COP-cladded microwire provides good transparency and silica fiber components are commercially available. Meanwhile, the remaining mid-IR spectral range up to 12 μm is yet to be explored, which is entirely covered by transmission windows of chalcogenide glass. Normal dispersion parametric generation is the most promising approach to enable nonlinear gain at wavelengths that are far-detuned from the pump wavelength by tens of THz. Parametric wavelength conversion up to a frequency detuning of 49.3 THz has been demonstrated in chalcogenide microwires cladded with cyclized transparent optical polymer [18], pumped by a mode-locked thulium-doped fiber laser centered at 1.94 μm. A FOPO based on such far-detuned parametric gain in chalcogenide microwires can be pumped by thulium-doped fiber lasers in 2 μm wavelength band, and emission can be enabled in 3 μm wavelength band or even further into mid-IR. However, building all-fiber oscillator cavities beyond 2 μm wavelength band requires not only mid-IR fibers, but also mid-IR fiber components, such as fiber couplers (both directional and wavelength division multiplexing couplers), filters, polarization controllers, etc. There are ongoing efforts to develop such mid-IR compatible chalcogenide fiber components. The development of these fiber components will also enable pulse characterization using chalcogenide microwires beyond 2 μm wavelength band. Another interesting approach for mid-IR pulse characterization would be utilizing the parametric signal on shorter wavelength side in the FWM-based

FROG architecture. Through far-detuned FWM in chalcogenide microwires with normal dispersion, mid-IR pulses in 3 μm wavelength band or beyond can be up-converted to 1.55 μm wavelength band, where highly sensitive photodetectors and OSAs are widely available, by using a continuous-wave laser pump source in 2 μm wavelength band.

Appendix A

Appendix

A.1 Numerical simulations

This sections provides the MATLAB code to simulate the impact of dispersion fluctuation on the actual parametric gain profile caused by longitudinal variation of optical fiber or microwire core diameter. As shown in the code below, dispersion and nonlinear parameters are curve fitted to more accurately evaluate continuous diameter fluctuation. A random walk of the microwire core radius is produced with a given coherence length.

```
c0 = 299792458;       %Speed of light, unit in [m/s]
a = 0.8125e-6;        %Average radius, unit in [m]
LambdaRef = 1.94e-6; %Pump wavelength, unit in [m]
Alpha_dB = 30;        %Average propagation loss, unit in [dB/m]
dOmega = 2*pi*(-60e12:5e10:60e12);      %Angular Frequency axis
Pp = 2.4;             %Peak pump power, unit in [W];
L = 0.1;              %Fiber or microwire length, unit in [m]
x = linspace(0, L, 10);     %Coherence length is 0.01 m
Ns = 100;             %Number of fiber or microwire segments

for i = 1:Ns          %The fiber or micowire is divided into 100 segments
    err = ones(11,1);
    errl = 1;
    errr = 1;

    while max(errl, errr)>0.5
        RandWalk = rand(10, 1);
```

```
        RandWalk = RandWalk - mean(RandWalk);
        errl = max(abs(RandWalk - [RandWalk(2:end); RandWalk(1)]));
        errr = max(abs(RandWalk - [RandWalk(end); RandWalk(1:end-1)]));
    end

    r0 = a + 25e-9*RandWalk;    %Radius added a random walk
    length = linspace(0, L, 100);
    randR = spline(x, r0, lengthl);
    figure(1); plot(l*100, 2e6*randR,':', 'LineWidth', 0.5)
    hold on
    DiaF = 2*randR;             %Diameter with random fluctuation

    Beta2  = polyval(B2Coeff, DiaF*1e6)*1e-24;
    Beta4  = polyval(B4Coeff, DiaF*1e6)*1e-48;
    GammaR = polyval(GammaCoeff, DiaF*1e6);

    Gain = FWM_Matrix(Pp, GammaR, Beta2, Beta4, Alpha_dB, dOmega, L, ...
       Ns);   %%% Matrix solution
    figure(2); plot(1e6*c0./(c0/LambdaRef + dOmega/2/pi), ...
       10*log10(Gain), ':','LineWidth', 0.5)
    hold on
end
```

A.2 Characteristic equation of three-layer fiber/microwire

$$
\begin{vmatrix}
\frac{\beta m}{u^2 r_1^2} J_m(ur_1) & \frac{k_0\eta_0}{ur_1} J'_m(ur_1) & \frac{\beta m}{\nu^2 r_1^2} K_m(\nu r_1) & \frac{\beta m}{\nu^2 r_1^2} I_m(\nu r_1) & \frac{k_0\eta_0}{\nu r_1} K'_m(\nu r_1) & \frac{k_0\eta_0}{\nu r_1} I'_m(\nu r_1) & 0 & 0 \\
0 & 0 & \frac{\beta m}{\nu^2 r_2^2} K_m(\nu r_2) & \frac{\beta m}{\nu^2 r_2^2} I_m(\nu r_2) & \frac{k_0\eta_0}{\nu r_2} K'_m(\nu r_2) & \frac{k_0\eta_0}{\nu r_2} I'_m(\nu r_2) & -\frac{\beta m}{\omega^2 r_2^2} K_m(\omega r_2) & -\frac{k_0\eta_0}{\omega r_2} K'_m(\omega r_2) \\
\frac{n_1^2 k_0}{ur_1} J'_m(ur_1) & \frac{\beta\eta_0 m}{u^2 r_1^2} J_m(ur_1) & \frac{n_2^2 k_0}{\nu r_1} K'_m(\nu r_1) & \frac{n_2^2 k_0}{\nu r_1} I'_m(\nu r_1) & \frac{\beta\eta_0 m}{\nu^2 r_1^2} K_m(\nu r_1) & \frac{\beta\eta_0 m}{\nu^2 r_1^2} I_m(\nu r_1) & 0 & 0 \\
0 & 0 & \frac{n_2^2 k_0}{\nu r_2} K'_m(\nu r_2) & \frac{n_2^2 k_0}{\nu r_2} I'_m(\nu r_2) & \frac{\beta\eta_0 m}{\nu^2 r_2^2} K_m(\nu r_2) & \frac{\beta\eta_0 m}{\nu^2 r_2^2} I_m(\nu r_2) & -\frac{n_3^2 k_0}{\omega r_2} K'_m(\omega r_2) & -\frac{\beta\eta_0 m}{\omega^2 r_2^2} K_m(\omega r_2) \\
J_m(ur_1) & 0 & -K_m(\nu r_1) & -I_m(\nu r_1) & 0 & 0 & 0 & 0 \\
0 & J_m(ur_1) & 0 & 0 & -K_m(\nu r_1) & -I_m(\nu r_1) & 0 & 0 \\
0 & 0 & K_m(\nu r_2) & I_m(\nu r_2) & 0 & 0 & -K_m(\omega r_2) & 0 \\
0 & 0 & 0 & 0 & K_m(\nu r_2) & I_m(\nu r_2) & 0 & -K_m(\omega r_2)
\end{vmatrix} = 0
$$

References

[1] S. D. Personick, *Fiber optics: technology and applications*. Springer Science & Business Media, 2013.

[2] G. P. Agrawal, *Nonlinear fiber optics (4^{th} ed.)*. Academic press, 2007.

[3] M. J. F. Digonnet, *Rare-earth-doped fiber lasers and amplifiers, revised and expanded*. CRC press, 2001.

[4] G. Agrawal, *Applications of nonlinear fiber optics (2^{nd} ed.)*. Academic press, 2008.

[5] D. J. Richardson, J. Nilsson, and W. A. Clarkson, "High power fiber lasers: current status and future perspectives," *JOSA B*, vol. 27, no. 11, pp. B63–B92, 2010.

[6] T. M. Monro and H. Ebendorff-Heidepriem, "Progress in microstructured optical fibers," *Annual Review of Materials Research*, vol. 36, pp. 467–495, 2006.

[7] P. Russell, "Photonic crystal fibers," *Science*, vol. 299, no. 5605, pp. 358–362, 2003.

[8] G. Brambilla, "Optical fibre nanowires and microwires: a review," *Journal of Optics*, vol. 12, no. 4, p. 043001, 2010.

[9] J. S. Sanghera, L. B. Shaw, and I. D. Aggarwal, "Chalcogenide glass-fiber-based mid-IR sources and applications," *IEEE Journal of selected topics in quantum electronics*, vol. 15, no. 1, pp. 114–119, 2009.

[10] D. Heard, *Analytical techniques for atmospheric measurement*. John Wiley & Sons, 2008.

[11] H. Hahn, J. Pallua, C. Pezzei, V. Huck-Pezzei, G. Bonn, and C. Huck, "Infrared-spectroscopy: a non-invasive tool for medical diagnostics and drug analysis," *Current medicinal chemistry*, vol. 17, no. 26, pp. 2956–2966, 2010.

[12] A. Schliesser, N. Picqué, and T. W. Hänsch, "Mid-infrared frequency combs," *Nature Photonics*, vol. 6, no. 7, p. 440, 2012.

[13] Y. Yao, A. J. Hoffman, and C. F. Gmachl, "Mid-infrared quantum cascade lasers," *Nature Photonics*, vol. 6, no. 7, p. 432, 2012.

[14] M. Ebrahim-Zadeh, "Mid-infrared optical parametric oscillators and applications," in *Mid-Infrared Coherent Sources and Applications*, pp. 347–375, Springer, 2008.

[15] S. D. Jackson, "Towards high-power mid-infrared emission from a fibre laser," *Nature Photonics*, 2012.

[16] J. H. V. Price, T. M. Monro, H. Ebendorff-Heidepriem, F. Poletti, P. Horak, V. Finazzi, J. Y. Y. Leong, P. Petropoulos, J. C. Flanagan, G. Brambilla, X. Feng, and D. J. Richardson, "Mid-IR supercontinuum generation from nonsilica microstructured optical fibers," *IEEE Journal of Selected Topics in Quantum Electronics*, vol. 13, no. 3, pp. 738–749, 2007.

[17] M. Bernier, V. Fortin, N. Caron, M. El-Amraoui, Y. Messaddeq, and R. Vallée, "Mid-infrared chalcogenide glass Raman fiber laser," *Optics letters*, vol. 38, no. 2, pp. 127–129, 2013.

[18] L. Li, N. Abdukerim, and M. Rochette, "Mid-infrared wavelength conversion from As_2Se_3 microwires," *Optics letters*, vol. 42, no. 3, pp. 639–642, 2017.

[19] C. Baker and M. Rochette, "Highly nonlinear hybrid AsSe-PMMA microtapers," *Optics express*, vol. 18, no. 12, pp. 12391–12398, 2010.

[20] R. Ahmad and M. Rochette, "Chalcogenide microwire based Raman laser," *Applied Physics Letters*, vol. 101, no. 10, p. 101110, 2012.

[21] R. Ahmad and M. Rochette, "Chalcogenide optical parametric oscillator," *Optics express*, vol. 20, no. 9, pp. 10095–10099, 2012.

[22] R. Ahmad and M. Rochette, "All-chalcogenide Raman-Parametric laser, wavelength converter, and amplifier in a single microwire," *IEEE Journal of Selected Topics in Quantum Electronics*, vol. 20, pp. 299–304, Sept. 2014.

[23] A. Al-Kadry, L. Li, M. El Amraoui, T. North, Y. Messaddeq, and M. Rochette, "Broadband supercontinuum generation in all-normal dispersion chalcogenide microwires," *Optics letters*, vol. 40, no. 20, pp. 4687–4690, 2015.

[24] L. Li, A. Al-Kadry, N. Abdukerim, and M. Rochette, "Design, fabrication and characterization of PC, COP and PMMA-cladded As_2Se_3 microwires," *Optical Materials Express*, vol. 6, no. 3, pp. 912–921, 2016.

[25] B. J. Eggleton, B. Luther-Davies, and K. Richardson, "Chalcogenide photonics," *Nature Photonics*, vol. 5, pp. 141–148, feb 2011.

[26] R. E. Slusher, G. Lenz, J. Hodelin, J. Sanghera, L. B. Shaw, and I. D. Aggarwal, "Large Raman gain and nonlinear phase shifts in high-purity As_2Se_3 chalcogenide fibers," *JOSA B*, vol. 21, no. 6, pp. 1146–1155, 2004.

[27] M. Asobe, T. Ohara, I. Yokohama, and T. Kaino, "Fabrication of Bragg grating in chalcogenide glass fibre using the transverse holographic method," *Electronics Letters*, vol. 32, pp. 1611–1613, Aug. 1996.

[28] M. Bernier, V. Fortin, M. El-Amraoui, Y. Messaddeq, and R. Vallée, "3.77 μm fiber laser based on cascaded Raman gain in a chalcogenide glass fiber," *Optics letters*, vol. 39, no. 7, pp. 2052–2055, 2014.

[29] S. D. Jackson and G. Anzueto-Sánchez, "Chalcogenide glass Raman fiber laser," *Applied physics letters*, vol. 88, no. 22, p. 221106, 2006.

[30] V. Fortin, M. Bernier, M. El-Amraoui, Y. Messaddeq, and R. Vallee, "Modeling of As_2S_3 Raman fiber lasers operating in the mid-infrared," *IEEE Photonics Journal*, vol. 5, no. 6, pp. 1502309–1502309, 2013.

[31] C. R. Petersen, U. M, I. Kubat, B. Zhou, S. Dupont, J. Ramsay, T. Benson, S. Sujecki, N. Abdel-Moneim, Z. Tang, D. Furniss, A. Seddon, and O. Band, "Mid-infrared supercontinuum covering the 1.4–13.3 μm molecular fingerprint region using ultra-high NA chalcogenide step-index fibre," *Nature Photonics*, vol. 8, no. 11, pp. 830–835, 2014.

[32] T. Cheng, K. Nagasaka, T. H. Tuan, X. Xue, M. Matsumoto, H. Tezuka, T. Suzuki, and Y. Ohishi, "Mid-infrared supercontinuum generation spanning 2.0 to 15.1 μm in a chalcogenide step-index fiber," *Optics Letters*, vol. 41, no. 9, pp. 2117–2120, 2016.

[33] J. A. Savage, "Optical properties of chalcogenide glasses," *Journal of Non-Crystalline Solids*, vol. 47, pp. 101–115, jan 1982.

[34] L. Calvez, "Chalcogenide glasses and glass-ceramics: transparent materials in the infrared for dual applications," *Comptes Rendus Physique*, vol. 18, pp. 314–322, may 2017.

[35] D. Y. Smith, E. Shiles, M. Inokuti, and E. D. Palik, "Handbook of optical constants of solids," *Handbook of Optical Constants of Solids*, vol. 1, pp. 369–406, 1985.

[36] A. materials Inc., "http://www.amorphousmaterials.com/products/."

[37] A. Al-kadry, C. Baker, M. El Amraoui, Y. Messaddeq, and M. Rochette, "Broadband supercontinuum generation in As_2Se_3 chalcogenide wires by avoiding the two-photon absorption effects," *Optics letters*, vol. 38, no. 7, pp. 1185–1187, 2013.

[38] M. E. Lines, "Oxide glasses for fast photonic switching: a comparative study," *Journal of applied physics*, vol. 69, no. 10, pp. 6876–6884, 1991.

[39] G. Lenz, J. Zimmermann, T. Katsufuji, M. E. Lines, H. Y. Hwang, S. Spälter, R. E. Slusher, S. W. Cheong, J. S. Sanghera, and I. D. Aggarwal, "Large Kerr effect in bulk Se-based chalcogenide glasses," *Optics Letters*, vol. 25, no. 4, pp. 254–256, 2000.

[40] M. Sheik-Bahae, D. J. Hagan, and E. W. Van Stryland, "Dispersion and band-gap scaling of the electronic Kerr effect in solids associated with two-photon absorption," *Physical review letters*, vol. 65, no. 1, p. 96, 1990.

[41] K. Richardson, T. Cardinal, M. Richardson, A. Schulte, and S. Seal, "Engineering glassy chalcogenide materials for integrated optics applications," in *Photo-Induced Metastability in Amorphous Semiconductors*, pp. 383–405, Wiley-VCH Verlag GmbH & Co. KGaA.

[42] R. W. Boyd, *Nonlinear optics*. Academic press, 2003.

[43] R. H. Stolen, J. P. Gordon, W. J. Tomlinson, and H. A. Haus, "Raman response function of silica-core fibers," *JOSA B*, vol. 6, no. 6, pp. 1159–1166, 1989.

[44] P. Pureza, V. Q. Nguyen, F. Kung, and I. D. Aggarwal, "Nonlinear properties of chalcogenide glass fibers," *Journal of Optoelectronics and Advanced Materials*, vol. 8, no. 6, pp. 2148–2155, 2006.

[45] K. J. Blow and D. Wood, "Theoretical description of transient stimulated Raman scattering in optical fibers," *IEEE Journal of Quantum Electronics*, vol. 25, no. 12, pp. 2665–2673, 1989.

[46] C. Xiong, E. Magi, F. Luan, A. Tuniz, S. Dekker, J. Sanghera, L. Shaw, I. Aggarwal, and B. Eggleton, "Characterization of picosecond pulse nonlinear propagation in chalcogenide As_2S_3 fiber," *Applied optics*, vol. 48, no. 29, pp. 5467–5474, 2009.

[47] J. Hu, C. R. Menyuk, L. B. Shaw, J. S. Sanghera, and I. D. Aggarwal, "Maximizing the bandwidth of supercontinuum generation in As_2Se_3 chalcogenide fibers," *Optics express*, vol. 18, no. 7, pp. 6722–6739, 2010.

[48] K. Ogusu, H. Li, and M. Kitao, "Brillouin-gain coefficients of chalcogenide glasses," *Journal of the Optical Society of America B*, vol. 21, p. 1302, jul 2004.

[49] P. Dumais, A. Villeneuve, P. G. J. Wigley, F. Gonthier, S. Lacroix, G. I. Stegeman, and J. Bures, "Enhanced self-phase modulation in tapered fibers," *Optics letters*, vol. 18, no. 23, pp. 1996–1998, 1993.

[50] E. C. Mägi, L. B. Fu, H. C. Nguyen, M. R. E. Lamont, D. I. Yeom, and B. J. Eggleton, "Enhanced Kerr nonlinearity in sub-wavelength diameter As_2Se_3 chalcogenide fiber tapers," *Optics Express*, vol. 15, no. 16, pp. 10324–10329, 2007.

[51] C. Baker and M. Rochette, "High nonlinearity and single-mode transmission in tapered multimode-PMMA fibers," *IEEE Photonics Journal*, vol. 4, no. 3, pp. 960–969, 2012.

[52] P.-A. Belanger, *Optical fiber Theory: A supplement to applied Electromagnetism*. World Scientific Press, 1993.

[53] A. V. Shahraam and T. M. Monro, "A full vectorial model for pulse propagation in emerging waveguides with subwavelength structures part I: Kerr nonlinearity," *Optics Express*, vol. 17, p. 2298, feb 2009.

[54] M. D. Turner, T. M. Monro, and A. V. Shahraam, "A full vectorial model for pulse propagation in emerging waveguides with subwavelength structures part II: stimulated Raman scattering," *Optics Express*, vol. 17, p. 11565, jul 2009.

[55] C. Baker and M. Rochette, "A generalized heat-brush approach for precise control of the waist profile in fiber tapers," *Optical Materials Express*, vol. 1, no. 6, pp. 1065–1076, 2011.

[56] I. Alamgir, N. Abdukerim, and M. Rochette, "In situ fabrication of far-detuned optical fiber wavelength converters," in *IEEE Photonics Conference (IPC)*, pp. 1–2, 2018.

[57] E. M. Dianov and A. M. Prokhorov, "Medium-power CW Raman fiber lasers," *IEEE Journal of Selected Topics in Quantum Electronics*, vol. 6, no. 6, pp. 1022–1028, 2000.

[58] Y. Feng, L. R. Taylor, and D. B. Calia, "150 W highly-efficient Raman fiber laser," *Optics express*, vol. 17, no. 26, pp. 23678–23683, 2009.

[59] F. Anguez, E. Courtade, A. Silvery, P. Suret, and S. Randoux, "High-power tunable Raman fiber ring for the investigation of singlet oxygen production from direct laser excitation around 1270 nm," *Optics Express*, vol. 18, no. 22, pp. 22928–22936, 2010.

[60] D. S. Kharenko, A. E. Bednyakova, E. V. Podivilov, M. P. Fedoruk, A. Apolonski, and S. A. Babin, "Cascaded generation of coherent Raman dissipative solitons," *Optics letters*, vol. 41, no. 1, pp. 175–178, 2016.

[61] D. Churin, J. Olson, R. A. Norwood, N. Peyghambarian, and K. Kieu, "High-power synchronously pumped femtosecond Raman fiber laser," *Optics letters*, vol. 40, no. 11, pp. 2529–2532, 2015.

[62] C. E. S. Castellani, E. J. Kelleher, J. C. Travers, D. Popa, T. Hasan, Z. Sun, E. Flahaut, A. C. Ferrari, S. V. Popov, and J. R. Taylor, "Ultrafast Raman laser mode-locked by nanotubes," *Optics letters*, vol. 36, no. 20, pp. 3996–3998, 2011.

[63] E. M. Dianov, I. Bufetov, V. M. Mashinsky, A. V. Shubin, O. I. Medvedkov, A. E. Rakitin, M. A. Mel'kumov, V. F. Khopin, and A. N. Gur'yanov, "Raman fibre lasers based on heavily GeO_2-doped fibres," *Quantum Electronics*, vol. 35, no. 5, pp. 435–441, 2005.

[64] O. P. Kulkarni, C. Xia, D. J. Lee, M. Kumar, A. Kuditcher, M. N. Islam, F. L. Terry, M. J. Freeman, B. G. Aitken, S. C. Currie, J. E. McCarthy, M. L. Powley, and D. A. Nolan, "Third order cascaded Raman wavelength shifting in chalcogenide fibers and determination of Raman gain coefficient," *Optics express*, vol. 14, no. 17, pp. 7924–7930, 2006.

[65] V. S. Shiryaev and M. F. Churbanov, "Trends and prospects for development of chalcogenide fibers for mid-infrared transmission," *Journal of Non-Crystalline Solids*, vol. 377, pp. 225–230, 2013.

[66] S. D. Jackson and G. Anzueto-Sánchez, "Chalcogenide glass Raman fiber laser," *Applied physics letters*, vol. 88, no. 22, p. 221106, 2006.

[67] S. Shabahang, G. Tao, J. J. Kaufman, and A. F. Abouraddy, "Dispersion characterization of chalcogenide bulk glass, composite fibers, and robust nanotapers," *JOSA B*, vol. 30, no. 9, pp. 2498–2506, 2013.

[68] L. Zhang, H. Jiang, X. Yang, W. Pan, and Y. Feng, "Ultra-wide wavelength tuning of a cascaded Raman random fiber laser," *Optics letters*, vol. 41, no. 2, pp. 215–218, 2016.

[69] V. R. Supradeepa and J. W. Nicholson, "Power scaling of high-efficiency 1.5 μm cascaded Raman fiber lasers," *Optics letters*, vol. 38, no. 14, pp. 2538–2541, 2013.

[70] S. D. Jackson and P. H. Muir, "Theory and numerical simulation of n^{th}-order cascaded Raman fiber lasers," *JOSA B*, vol. 18, no. 9, pp. 1297–1306, 2001.

[71] R. T. White and T. M. Monro, "Cascaded Raman shifting of high-peak-power nanosecond pulses in As_2S_3 and As_2Se_3 optical fibers," *Optics letters*, vol. 36, no. 12, pp. 2351–2353, 2011.

[72] L. Vácha, M. Granberg, P. Marcollà, and U. Lindborg, "Manufacture of optical fibres by the double-crucible method," *Journal of Non-Crystalline Solids*, vol. 38, pp. 797–802, 1980.

[73] G. Xue, B. Zhang, K. Yin, W. Yang, and J. Hou, "Ultra-wideband all-fiber tunable Tm/Ho-co-doped laser at 2 μm," *Optics express*, vol. 22, no. 21, pp. 25976–25983, 2014.

[74] J. Troles, Q. Coulombier, G. Canat, M. Duhant, W. Renard, P. Toupin, L. Calvez, G. Renversez, F. Smektala, M. El Amraoui, J. L. Adam, T. Chartier, D. Mechin, and L. Brilland, "Low loss microstructured chalcogenide fibers for large nonlinear effects at 1995 nm," *Optics Express*, vol. 18, no. 25, pp. 26647–26654, 2010.

[75] T. Cheng, S. Li, X. Yan, T. H. Tuan, M. Matsumoto, S. Cho, T. Suzuki, and Y. Ohishi, "Mid-infrared cascaded stimulated Raman scattering up to eight orders in As-S optical fiber," *Optics express*, vol. 26, no. 9, pp. 12007–12015, 2018.

[76] J. Yao, B. Zhang, K. Yin, L. Yang, J. Hou, and Q. Lu, "Mid-infrared supercontinuum generation based on cascaded Raman scattering in a few-mode As_2S_3 fiber pumped by a thulium-doped fiber laser," *Optics Express*, vol. 24, no. 13, pp. 14717–14724, 2016.

[77] R. Stolen, C. Lin, and R. Jain, "A time-dispersion-tuned fiber Raman oscillator," *Applied Physics Letters*, vol. 30, no. 7, pp. 340–342, 1977.

[78] F. Vanier, Y.-A. Peter, and M. Rochette, "Cascaded Raman lasing in packaged high quality As_2S_3 microspheres," *Optics Express*, vol. 22, no. 23, pp. 28731–28739, 2014.

[79] M. H. Dunn and M. Ebrahimzadeh, "Parametric generation of tunable light from continuous-wave to femtosecond pulses," *Science*, vol. 286, pp. 1513–1517, nov 1999.

[80] M. E. Marhic, *Fiber optical parametric amplifiers, oscillators and related devices*. Cambridge university press, 2008.

[81] A. Gershikov, E. Shumakher, A. Willinger, and G. Eisenstein, "Fiber parametric oscillator for the 2 μm wavelength range based on narrowband optical parametric amplification," *Optics Letters*, vol. 35, p. 3198, sep 2010.

[82] R. Ahmad and M. Rochette, "High efficiency and ultra broadband optical parametric four-wave mixing in chalcogenide-PMMA hybrid microwires," *Optics express*, vol. 20, no. 9, pp. 9572–9580, 2012.

[83] M. Farahmand and M. de Sterke, "Parametric amplification in presence of dispersion fluctuations," *Optics express*, vol. 12, no. 1, pp. 136–142, 2004.

[84] J. A. Buck, *Fundamentals of optical fibers*. John Wiley & Sons, 2004.

[85] M.-C. Ho, K. Uesaka, M. Marhic, Y. Akasaka, and L. G. Kazovsky, "200-nm-bandwidth fiber optical amplifier combining parametric and Raman gain," *Journal of Lightwave Technology*, vol. 19, no. 7, pp. 977–981, 2001.

[86] T. Godin, Y. Combes, R. Ahmad, M. Rochette, T. Sylvestre, and J. M. Dudley, "Far-detuned mid-infrared frequency conversion via normal dispersion modulation instability in chalcogenide microwires," *Optics letters*, vol. 39, no. 7, pp. 1885–1888, 2014.

[87] F. Yaman, Q. Lin, S. Radic, and G. P. Agrawal, "Impact of dispersion fluctuations on dual-pump fiber-optic parametric amplifiers," *IEEE Photonics Technology Letters*, vol. 16, no. 5, pp. 1292–1294, 2004.

[88] J. S. Y. Chen, S. G. Murdoch, R. Leonhardt, and J. D. Harvey, "Effect of dispersion fluctuations on widely tunable optical parametric amplification in photonic crystal fibers," *Optics Express*, vol. 14, no. 20, pp. 9491–9501, 2006.

[89] D. Chow, J. C. T. Nougnihi, A. Denisov, J.-C. Beugnot, T. Sylvestre, L. Li, R. Ahmad, M. Rochette, K. H. Tow, M. A. Soto, and L. Thévenaz, "Mapping the uniformity of optical microwires using phase-correlation brillouin distributed measurements," in *Frontiers in Optics*, pp. FW4F–4, Optical Society of America, 2015.

[90] X. Liu, R. M. Osgood, Y. A. Vlasov, and W. M. J. Green, "Mid-infrared optical parametric amplifier using silicon nanophotonic waveguides," *Nature Photonics*, vol. 4, no. 8, pp. 557–560, 2010.

[91] M. Karlsson, "Four-wave mixing in fibers with randomly varying zero-dispersion wavelength," *JOSA B*, vol. 15, no. 8, pp. 2269–2275, 1998.

[92] B. Kuyken, X. Liu, R. M. Osgood, R. Baets, G. Roelkens, and W. M. J. Green, "A silicon-based widely tunable short-wave infrared optical parametric oscillator," *Optics express*, vol. 21, no. 5, pp. 5931–5940, 2013.

[93] R. Trebino, K. W. DeLong, D. N. Fittinghoff, J. N. Sweetser, M. A. Krumbügel, B. A. Richman, and D. J. Kane, "Measuring ultrashort laser pulses in the time-frequency domain using frequency-resolved optical gating," *Review of Scientific Instruments*, vol. 68, no. 9, pp. 3277–3295, 1997.

[94] R. Trebino, *Frequency-resolved optical gating: the measurement of ultrashort laser pulses*. Springer Science & Business Media, 2012.

[95] H. Miao, S.-D. Yang, C. Langrock, R. V. Roussev, M. M. Fejer, and A. M. Weiner, "Ultralow-power second-harmonic generation frequency-resolved optical gating using aperiodically poled lithium niobate waveguides," *JOSA B*, vol. 25, no. 6, pp. A41–A53, 2008.

[96] H. Miao, A. M. Weiner, C. Langrock, R. V. Roussev, and M. M. Fejer, "Polarization-insensitive ultralow-power second-harmonic generation frequency-resolved optical gating," *Optics letters*, vol. 32, no. 7, pp. 874–876, 2007.

[97] P.-A. Lacourt, J. M. Dudley, J.-M. Merolla, H. Porte, J.-P. Goedgebuer, and W. T. Rhodes, "Milliwatt-peak-power pulse characterization at 1.55 μm by wavelength-conversion frequency-resolved optical gating," *Optics letters*, vol. 27, no. 10, pp. 863–865, 2002.

[98] M. D. Thomson, J. M. Dudley, L. P. Barry, and J. D. Harvey, "Complete pulse characterization at 1.5 μm by cross-phase modulation in optical fibers," *Optics letters*, vol. 23, no. 20, pp. 1582–1584, 1998.

[99] P. A. Lacourt, M. Hanna, and J. M. Dudley, "Broad-band and ultrasensitive pulse characterization using frequency-resolved optical gating via four-wave mixing in a semiconductor optical amplifier," *IEEE photonics technology letters*, vol. 17, no. 1, pp. 157–159, 2005.

[100] J. J. Ferreiro, R. de La Fuente, and E. López-Lago, "Characterization of arbitrarily polarized ultrashort laser pulses by cross-phase modulation," *Optics letters*, vol. 26, no. 13, pp. 1025–1027, 2001.

[101] K. G. Petrillo, K.-Y. Wang, A. C. Foster, and M. A. Foster, "Highly sensitive ultrafast pulse characterization using hydrogenated amorphous silicon waveguides," *Optics express*, vol. 21, no. 25, pp. 31229–31238, 2013.

[102] E.-K. Tien, X.-Z. Sang, F. Qing, Q. Song, and O. Boyraz, "Ultrafast pulse characterization using cross phase modulation in silicon," *Applied Physics Letters*, vol. 95, no. 5, p. 051101, 2009.

[103] E. A. Anashkina, A. V. Andrianov, M. Y. Koptev, and A. V. Kim, "Complete field characterization of ultrashort pulses in fiber photonics," *IEEE Journal of Selected Topics in Quantum Electronics*, vol. 24, no. 3, pp. 1–7, 2018.

[104] N. Abdukerim, L. Li, and M. Rochette, "Chalcogenide-based optical parametric oscillator at 2 μm," *Optics letters*, vol. 41, no. 18, pp. 4364–4367, 2016.

[105] K. W. DeLong and R. Trebino, "Improved ultrashort pulse-retrieval algorithm for frequency-resolved optical gating," *JOSA A*, vol. 11, no. 9, pp. 2429–2437, 1994.

[106] A. Wienke, F. Haxsen, D. Wandt, U. Morgner, J. Neumann, and D. Kracht, "Ultrafast, stretched-pulse thulium-doped fiber laser with a fiber-based dispersion management," *Optics letters*, vol. 37, no. 13, pp. 2466–2468, 2012.

[107] P. Ciąćka, A. Rampur, A. Heidt, T. Feurer, and M. Klimczak, "Dispersion measurement of ultra-high numerical aperture fibers covering thulium, holmium, and erbium emission wavelengths," *JOSA B*, vol. 35, no. 6, pp. 1301–1307, 2018.

[108] J. M. Dudley, L. P. Barry, J. D. Harvey, M. D. Thomson, B. C. Thomsen, P. G. Bollond, and R. Leonhardt, "Complete characterization of ultrashort pulse sources at 1550 nm," *IEEE Journal of Quantum Electronics*, vol. 35, no. 4, pp. 441–450, 1999.

[109] P. Honzatko, J. Kanka, and B. Vrany, "Retrieval of the pulse amplitude and phase from cross-phase modulation spectrograms using the simulated annealing method," *Optics express*, vol. 12, no. 24, pp. 6046–6052, 2004.

[110] P. Honzatko, J. Kanka, and B. Vrany, "Measurement of pulse amplitude and phase using cross-phase modulation in microstructured fiber," *Optics Letters*, 2005.

[111] D. D. Hudson, S. Antipov, L. Li, I. Alamgir, T. Hu, M. El Amraoui, Y. Messaddeq, M. Rochette, S. D. Jackson, and A. Fuerbach, "Toward all-fiber supercontinuum spanning the mid-infrared," *Optica*, vol. 4, no. 10, pp. 1163–1166, 2017.

[112] D. J. Kane, "Real-time measurement of ultrashort laser pulses using principal component generalized projections," *IEEE Journal of Selected Topics in Quantum Electronics*, vol. 4, no. 2, pp. 278–284, 1998.

[113] A. Al-Kadry, M. El Amraoui, Y. Messaddeq, and M. Rochette, "Mode-locked fiber laser based on chalcogenide microwires," *Optics letters*, 2015.

[114] D. Derickson, *Fiber Optic Test and Measurement*. Prentice Hall, 1998.